Characteristic Morphology, Backscatter, and Sub-seafloor Structures of Cold-Vents on the Northern Cascadia Margin from High-Resolution Autonomous Underwater Vehicle Data

by

Jonathan Furlong
BSc, Memorial University Of Newfoundland, 2010

A Thesis Submitted in Partial Fulfillment
of the Requirements for the Degree of

Masters of Science

in the School of Earth and Ocean Sciences

Supervisory Committee

Characteristic Morphology, Backscatter, and Sub-seafloor Structures of Cold-Vents on the Northern Cascadia Margin from High-Resolution Autonomous Underwater Vehicle Data

by

Jonathan Furlong
BSc, Memorial University Of Newfoundland, 2010

Supervisory Committee

Michael Riedel, School of Earth and Ocean Sciences, Geological Survey of Canada, Natural Resources Canada
Co-Supervisor

George Spence, School of Earth and Ocean Sciences
Co-Supervisor

Phil Hill, School of Earth and Ocean Sciences, Geological Survey of Canada, Natural Resources Canada
Member

Abstract

Supervisory Committee

Michael Riedel, School of Earth and Ocean Sciences, Geological Survey of Canada, Natural Resources Canada
Co-Supervisor

George Spence, School of Earth and Ocean Sciences
Co-Supervisor

Phil Hill, School of Earth and Ocean Sciences, Geological Survey of Canada, Natural Resources Canada
Member

In this thesis seafloor cold vents are examined using autonomous underwater vehicle (AUV) and remotely operated vehicle (ROV) data on the Northern Cascadia margin. These data were collected in a 2009 joint cruise between the Monterey Bay Aquarium Research Institute (MBARI) and Natural Resources Canada (NRCan). High-resolution bathymetry data, acoustic reflectivity (backscatter) data, and 3.5 kHz sub bottom profiler data were examined for cold-vent-related features that include pockmarks, chemosynthetic biological communities (CBC), and authigenic carbonate. Additionally subsequent ROV observations, sediments from push cores and seafloor video/photos were used to ground truth AUV data. Numerous prolific venting sites were examined in detail and a model for the evolution of venting was generated. Vents are categorized as juvenile, intermediate, or mature depending on the presence and or absence of cold-vent-features. High near-surface reflection amplitudes are coincident with an anomalous area of seafloor backscatter. In June of 2012, NEPTUNE (North East Pacific Time-series Underwater Networked Experiment) collected a near-surface push

core with their ROV ROPOS (Remotely Operated Platform for Ocean Sciences) in the high reflective area. The retrieved core showed stacked turbidites in the top 0.5 meters of the sediment column. Closely spaced high-velocity turbidite sands are highly reflective and inhibit acoustic penetration to depth. The presence of high-density, high-velocity sands in the near surface is linked to steady ocean bottom currents. These bottom currents progress northeast to southwest over the study area and differentially erode the surface sediments by removing muds and leaving heavy sands over the exposed area.

Table of Contents

Supervisory Committee ii
Abstract iii
Table of Contents v
List of Tables vii
List of Figures viii
Acknowledgments x
1 Introduction 1
1.1 Motivation for Study 1
1.2 Historical study of Methane Cycle on Continental Margins 2
1.3 Thesis Objectives 6
1.4 Study Area 7
1.5 Previous Work 11
1.6 Project Data 13
2 Regional Geology and Cold Vents 17
2.1 The Cascadia Margin 17
2.1.1 Tectonics 18
2.1.2 Sediment Supply 21
2.2 Accretionary Prism 22
2.2.1 Accretionary Prism Mechanics 25
2.2.2 Deformation 26
2.2.3 Fluid Advection Variations Across The Prism 28
2.3 Cold Vent Dynamics 32
2.3.1 Methane Generation 33
2.3.2 Hydrate Stability 34
2.3.3 Bottom Simulating Reflector (BSR) 39
2.3.4 Hydrate Formation Mechanisms 42
2.3.5 Hydrate Pull-up Structures 43
2.3.6 Carbonate Structures 45
2.3.7 Chemosynthetic Biological Communities 46
3 AUV Data – Methods 49
3.1 AUV Module 49
3.2 Data Acquisition and Processing 50
3.2.1 Bathymetry 52
3.2.2 Non Side-scan Chirp Sonar Reflectivity 54
3.2.3 Side-scan Sonar Reflectivity 56
3.2.4 Sub-Bottom Profiler 59
4 ROV and AUV Observations 64
4.1 Robotic Underwater Vehicle (ROV) Visual Observations 64
4.1.1 ROV Seafloor Waypoints and Images 64
4.1.2 Chemosynthetic Communities 75
4.1.3 Authigenic Carbonates 75

4.1.4 ROV Sonar 76
4.2 Sediment Core 77
4.2.1 Core Description 77
4.2.2 Physical Properties 78
4.2.3 Carbon Dating 82
4.3 AUV Observations 84
4.3.1 Cucumber Ridge 90
4.3.2 Spinnaker Vent 94
4.3.3 Snake Vent 98
4.3.4 Ridge Crest Crater 103
4.3.5 Bullseye Vent 108
4.3.6 Bubbly Gulch 114
5 Discussion and Interpretation 118
5.1 Regional Blanking 119
5.1.1 Cause of widespread blanking: Occurrence of free gas? 122
5.1.2 Cause of widespread blanking: Transmission losses from "hard" layers? . 124
5.2 Localized Blanking 130
5.2.1 Spatial Trends In Blanking 133
5.2.2 Structure of individual Cold Vent Sites 134
5.3 Patterns In Seafloor Backscatter at Cold Vents 137
5.3.1 Carbonates 137
5.3.2 Chemosynthetic Biological Communities (CBC) 140
5.4 Pull-up structures and associated gas hydrate at discrete (vertical) vent sites ... 141
5.5 Evidence for evolutionary history of venting and related surface and sub-surface geophysical expressions 145
5.6 Evolution of Venting 149
5.6.1 Juvenile 151
5.6.2 Intermediate 152
5.6.3 Mature 154
5.7 Can Ocean-Bottom Currents cause anomalous seafloor backscatter highs? A proposed new mechanism 155
6 Summary and Conclusions 158
Bibliography 160

List of Tables

Table 4.1 83
Table 5.1 125
Table 5.2 150

List of Figures

Figure 1.1 Location of the Study Area 8
Figure 1.2 Regional Bathymetry Through Study Area 9
Figure 1.3 Seismic Line 89-08 10
Figure 1.4 MBARI AUV Schematic 14
Figure 1.5 MBARI's ROV Doc Rickets 14
Figure 1.6 Illustration of AUV Penetration Depth 16
Figure 2.1 Subduction Tectonics of the North West Pacific 19
Figure 2.2 Tectonic cross section through the northern Cascadia Margin 23
Figure 2.3 Regional bathymetry across accretionary wedge 24
Figure 2.4 Accretionary ridges of the study area 27
Figure 2.5 Accretionary wedge interval velocities and porosities 30
Figure 2.6 Fluid expulsion rate and total fluid expulsion across the prism. 31
Figure 2.7 Complexity of fluid flow across the margin illustration 32
Figure 2.8 Marine gas hydrate stability 36
Figure 2.9 IODP site U1327 and U1328 sulfate-methane transition zone 37
Figure 2.10 Sulfate-methane transition zone (SMTZ) illustration 38
Figure 2.11 Methane concentrations for IODP sites and inferred BSR depths 41
Figure 2.12 Methane degassing affects on seafloor biota concentration 48
Figure 3.1 AUV track lines and high-resolution bathymetry 51
Figure 3.2 High-resolution bathymetry 53
Figure 3.3 Vertical incidence sonar corrected for topography 55
Figure 3.4 Sidescan backscatter "shingling" method 57
Figure 3.5 Combined side-scan sonar backscatter (grids 1-3) 58
Figure 3.6 Sub-bottom profiler time adjustment 60
Figure 3.7 Spectral Analysis Of Profiler Data 63
Figure 4.1 High-resolution bathymetry outlining ROV dive and core locations 66
Figure 4.2 Spinnaker Vent ROV dive waypoints 67
Figure 4.3 Ridge Crest Crater ROV dive waypoints 68
Figure 4.4 Bullseye Vent ROV dive waypoints 69
Figure 4.5 Bubbly Gulch ROV dive waypoints 70
Figure 4.6 ROV dive images Spinnaker Vent 71
Figure 4.7 ROV dive images Ridge Crest Crater 72
Figure 4.8 ROV dive images Bullseye Vent 73
Figure 4.9 ROV dive images Bubbly Gulch 74
Figure 4.10 ROV Sonar Bubble Plumes 76
Figure 4.11 Core R1554 With Munsell Colors 79
Figure 4.12 Sediment Core R1554 Description 80
Figure 4.13 Core R1554 Physical Properties 81
Figure 4.14 Regional Bathymetry With 3D Image Locations. 85
Figure 4.15 Regional backscatter with bathymetry contours 87
Figure 4.16 Regional backscatter with sites of interest outlined. 88
Figure 4.17 High-resolution bathymetry with AUV track lines 89

Figure 4.18 3D perspective of Cucumber Ridge 91
Figure 4.19 Backscatter image of cucumber ridge 92
Figure 4.20 Sub-bottom profiler across Cucumber Ridge 93
Figure 4.21 3D perspective view of Spinnaker Vent 95
Figure 4.22 Backscatter image of Spinnaker Vent 96
Figure 4.24 3D perspective of Snake Vent 100
Figure 4.25 Backscatter image of Snake Vent 101
Figure 4.26 Sub-bottom profiler through Snake Vent 102
Figure 4.27 3D perspective of Ridge Crest Creater 105
Figure 4.28 Backscatter image of Ridge Crest Crater 106
Figure 4.29 Sub-bottom profiler across Ridge Crest Crater 107
Figure 4.30 3D perspective of Bullseye Vent 110
Figure 4.31 Backscatter Image Of Bullseye Vent 111
Figure 4.32 Sub-bottom profiler through Bullseye Vent, perpendicular to vent axis..... 112
Figure 4.33 Sub-bottom profiles across Bullseye Vent to Bubbly Gulch, parallel to vent axis 113
Figure 4.34 3D perspective of Bubbly Gulch 116
Figure 4.35 Backscatter image of Bubbly Gulch 117
Figure 5.1 Extent of regional and localized blanking on the grid of AUV lines 120
Figure 5.2 Profiler line A-A' showing regional blanking northeast of Cucumber Ridge121
Figure 5.3 Reflectivity values as calculated by Fink and Spence (1993) 127
Figure 5.4 Core R1554 seafloor screen capture 129
Figure 5.5 Single channel seismic (SCS) Line 27 132
Figure 5.6 AUV backscatter with sites of interest 138
Figure 5.7 AUV Line 20090625_0042, shallow vent chimneys 143
Figure 5.8 AUV Line 20090623_0035, shallow vent chimneys 144
Figure 5.9 AUV with SCS Line 27 148
Figure 5.10 Illustration of Juvenile Venting 152
Figure 5.11 Illustration of Intermediate Venting 153
Figure 5.12 Illustration of Mature Cold Vent Site 155
Figure 5.13 Bottom current affects on backscatter intensity 157

Acknowledgments

First and foremost I would like to thank my supervisor Dr. Michael Riedel for all his support and mentorship during this thesis. I commend Michael for his ability to quickly turn over drafts of this thesis that allowed me to maintain a consistent workflow towards the end. I would like to thank Dr. George Spence for his continued support and input on my thesis work, I always left Dr. Spence's presence with more knowledge than what I had previously. I would also like to thank Dr. Michael Whiticar for his thoughts and input while he was on the committee, and Dr. Phil Hill for filling in for Dr. Whiticar at the end of my thesis on short notice.

I would like to thank the Monterey Bay Aquarium Research Institute in California for the use of their facilities, data, and for Dr. Charlie Paull's continued enthusiasm and support for this work. Additionally I would like to thank MBARI's Dr. Peter Brewer for my time at sea, and the rest of the MBARI staff including the crew and operators of the Western Flyer.

A big thanks goes out to everyone at the Pacific Geoscience Center in Sidney for the use of their facilities and for providing me with a powerful computer to handle the resolution of my data. A final thanks goes out to the many students, staff, and facility at the University of Victoria and especially the Department of Earth and Ocean Sciences. I very much enjoyed the time I spent studying at the university and I look forward to spending more time on the Island in the future.

1 Introduction

This chapter outlines the motivation for this marine geology research and the objectives of this thesis. A brief introduction describes the cycle of methane in marine sediments and how its importance to society warrants continued research. Finally a brief description of the study area and AUV data location is provided, and the background geological and geophysical research previously done in the area is briefly summarized.

1.1 Motivation for Study

The ocean floor remains for most parts one of the least explored regions of our planet, and while this fact is rapidly changing due to advancements in seafloor mapping technology and increased interest within the scientific community, the processes that define seafloor geology and morphology are still poorly understood. Seafloor cold vent sites are recognized globally on continental shelves as sites of vigorous methane expulsion and carbonate formation, and as habitat for unique chemo-synthetic and biological communities. However, more research is necessary to understand better the evolution and significance of cold vents, especially with respect to their spatial distribution and evolution in methane degassing, in the associated build-ups of carbonate platforms, and in the formation of massive gas hydrate mounds. Historically (prior to about the year 2000), research was hampered due to limitations in sufficient high-resolution survey equipment. Using more contemporary survey equipment developed

over the past 5-6 years, such as autonomous underwater vehicles (AUVs), this thesis aims to add to the limited data library for fine scale examination (<20m) of cold vent populations, and attempts to describe how these vents behave and develop over time.

1.2 Historical study of Methane Cycle on Continental Margins

Continental margins (both passive and active) host vast amounts of organically derived carbon co-deposited during sedimentation. Over time organic carbon is altered to methane by both biological and physical processes, and eventually migrates towards the surface. Seafloor venting characteristics were first identified by the discovery of pockmarks. Pockmarks were initially distinguished on the seafloor by small concave features at the sediment-water interface, as imaged by echograms. The lateral extent of these features was first mapped off the Nova Scotia shelf (King and Maclean, 1970) following the development of side-scan sonar techniques (about 1965). Later cold-vent communities were unintentionally observed during a dive by the submersible Alvin in the Gulf of Mexico (Paull et al., 1984). Moreover, natural gas seeps were observed on the seafloor of the North Sea during surveys for potential pipeline routes (Hovland et al., 1987). The 25 years that followed encompassed abundant research to understand methane budgets in marine sediments and the flux of methane into the ocean and atmosphere. Research was mainly directed at developing more robust climate models to understand potential feedbacks in climate change (global warming) associated with the store-house of methane in marine sediments.

Seafloor sites prone to methane venting are named “cold vents”; these sites are associated with shallow gas accumulations, pockmarks, gas hydrate deposits, authigenic carbonate, and biological communities. Their naming convention stems from the earlier discovery of “hot vents” at mid-ocean ridges, where fluids well in excess of 80°C are expelled at the seafloor. The “cold vents” in contrast lack often (but not necessarily always) a strong thermal anomaly as measured in the sediments and fluids that are expelled (water and/or gas) and do not exhibit signs of increased temperatures relative to the surrounding areas.

Marine sediments hosting high concentrations of methane are appropriate environments for the formation of gas hydrate. Gas hydrate is an ice-like clathrate structure with methane as the host molecule. The existence of naturally occurring gas hydrate on continental margins was not documented until the 1970’s (Shipley et al., 1979) through evidence of a widespread Bottom Simulating Reflector (BSR). Recent estimates of global mass of gas hydrate in marine sediments covers a broad range from 0.5-2.5 x 10^3 Gt (Milkov, 2004), 3.0 x 10^3 Gt (Buffett and Archer, 2004), and 85 x 10^3 Gt (Kluada and Sandler, 2005). These estimates are still received contentiously due to the lack of constrainable hydrate data globally. Naturally occurring hydrate structures that develop on the seafloor contain dense concentrations of methane gas. Methane is known to occur in concentrations up to 7.6 mol/L, or more simply, dissociated hydrate would have a methane-to-water ratio of 164:1 at standard temperature and pressure (STP) (e.g. Sloan, 1990).

Marine and permafrost accumulations of gas hydrate have been suggested as a potential energy resource. Dispersed gas hydrate in fine grained sediment (e.g. at the

Blake Ridge or in the Gulf of Mexico) lack sufficiently high concentrations of methane to make extraction economical with current technology and at global gas market prices. However, areas of coarser-grained sediments with higher porosities and permeabilities are more suitable for hydrate accumulation and flow (e.g. found in the Nankai Trough or at Mallik). The 2008 Malik well test in permafrost had initial production values of 3500-4000 m^3d^{-1} (Dallimore et al., 2012). Gas hydrate may not be a practical energy source, since uncertainty still exists on whether production can maintain a dependable flow rate beyond the initial production period, which was 6 days at Malik. At the time of this thesis (May 2013) initial production tests are being carried out by the Japanese government in the marine sediments of the Nankai Trough. The results of these production tests, improvements in engineering technologies, and the growing demand for fossil fuels could lead to gas hydrate becoming an economical fuel source.

The co-deposition of organic carbon with inorganic seafloor sediments is considered to remove carbon from the rapid-cycling biogeosphere. Studies show that 16-40 MT (megatons) of methane may be released annually from continental shelves (Judd et al., 2002). On margins, cold vent sites are considered zones of macro-seepage and account for the largest geological release of methane at 1,000 t of carbon annually (Etiope and Klusman, 2002). The leakage of methane from sediment to the atmosphere and ocean can occur as slow microseepage from sedimentary basins (Etiope and Klusman, 2002), or in localized areas of increased flow (i.e. seafloor cold vents). The release of methane from the seabed can be considered a variable process that may be heightened daily by tidal affects (Boles and Clark, 2001) or yearly to decadal by seismic activity (Tsunogai et al., 2012). Additionally, the nature of methane release varies from

margin to margin. On active margins such as the Cascadia margin, venting processes are more complex than on passive margins, since they also involve sediment compression due to tectonic forces. The relationship between active tectonics and fluid venting across the Cascadia subduction zone was initially described by Hyndman and Davis (1992), later updated by Riedel et al. (2010) from IODP Expedition 311, and most recently modelled by Archer and Buffett (2012).

Understanding the behaviour of methane in marine sediments is foremost when attempting to interpret slope failures and assess geo-hazards on continental margins. Earthquakes and the dissociation of gas hydrate have both been linked to the potential destabilization of continental slopes leading to slope failure. For example, the Storegga Slide offshore Norway (Bryn et al., 2005) is probably the most prominent slope failure recorded during the Holocene. The slide is suspected to have been triggered by the dissociation of gas hydrate following changes in ocean temperatures. The failure is dated at 8200 BP and mobilized 2500-3500 km^3 of sediment as calculated from the slide scar dimensions (e.g. Haflidason et al., 2005). The slide triggered a tsunami that hit Norway (10-12 m), Scotland (4-6 m), Shetland (20-30 m), and the Faroe Islands (>10 m) (Bondevik et al., 2005).

Methane can also act as a potential modifier of the world`s climate. The influence of methane as a greenhouse gas is 21-23 times that of carbon dioxide (e.g. Lelieveld et al., 1998) but only over a relatively short period of time as methane is rapidly oxidized to CO_2 in the atmosphere. The end of the Palaeocene (~57 Ma) was denoted by a massive oxygen and carbon isotope excursion coinciding with intense global warming and deep-sea benthic extinction (Alegret and Ortiz, 2007). These prolific changes resonated in the

environment and had effects on biological evolution thereafter (Kennett and Scott, 1991). Momentous events like these gave rise to the Clathrate Gun Hypothesis (Kennett et al., 2003); this hypothesis links large methane release to near- instantaneous climate tipping events. A debate exists over whether the source of methane is derived from marine sediments (O'Hara, 2008) or sourced from the continent (Etiope et al., 2008).

1.3 Thesis Objectives

In this thesis I examine geophysical data acquired in 2009 by an autonomous underwater vehicle (AUV) and remotely operated vehicle (ROV) over known cold vents on the Northern Cascadia margin off Vancouver Island. The objective is to improve our understanding of fluid venting processes on the margin, from apparently "fresh" or recently initiated methane venting on the seafloor with no indication of chemosynthetic communities to mature carbonate platforms void of any active venting and biological communities. Motivation for this research is to aid future IODP drilling and borehole-observatory installations and additionally, in collaboration with Florida State University and NEPTUNE-Canada, to assess base data for time series analysis (North East Pacific Time-series Underwater Networked Experiment) that may link earthquake shaking to fluid expulsion and changes in seabed morphology.

1.4 Study Area

This thesis study area covers approximately 32 km^2 surveyed by the AUV on the mid-continental slope off Vancouver Island (Figure 1.1). The study area is ~20 km from the deformation front and ~30 km from the continental shelf edge. On the northern Cascadia Margin, seafloor ridges provide bathymetric relief of over 800 m (Figure 1.2). Multichannel seismic line 89-08 (Figure 1.2, 1.3), collected in 1989 by the Geological Survey of Canada, acts as a central line for the interpretation of the deep tectonic setting of the study area (e.g. Hyndman, 1995; Yuan et al., 1996; Riedel et al., 2006). Seismic line 89-08 (Figure 1.3) through the area shows the location of the AUV grid is ~17.5 km northeast of the deformation front, between shot points 2000-2400 on seismic line 89-08 (Figure 1.3). The high-resolution bathymetric grid and AUV lines lie between two topographic highs that rise more than 200 m above the surrounding seafloor (Figure 1.1 C). The seafloor in this region shows abundant surface expressions of fluid venting creating chemosynthetic biological communities (CBC), methane bubble plumes, and authigenic carbonate, which have been previously described by Riedel et al., (2002); Riedel et al., 2010; Riedel et al., 2006-IODP volume; Zykov, 2003; and Vidalie (2006).

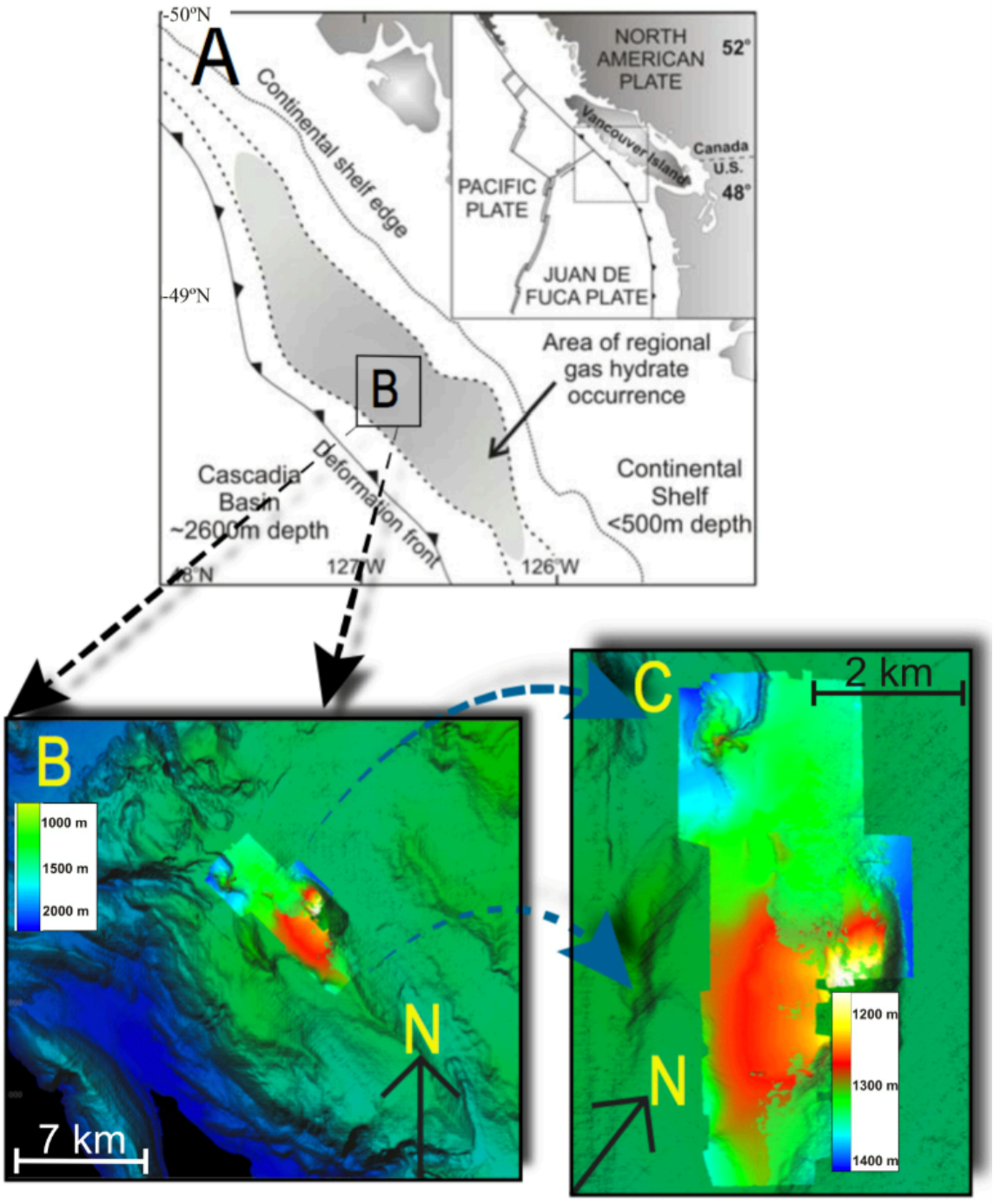

Figure 1.1 Location of the Study Area

(A) Illustration of the Northern Cascadia margin showing the location of the deformation front, extent of the continental shelf, and the approximate zone of gas hydrate stability (modified from Hyndman 2001). (B) Location of study area along the continental slope with regional bathymetry. The Cascadia basin lies to the west and the continental shelf to the east. (C) Location of high-resolution bathymetry grid atop a structural high.

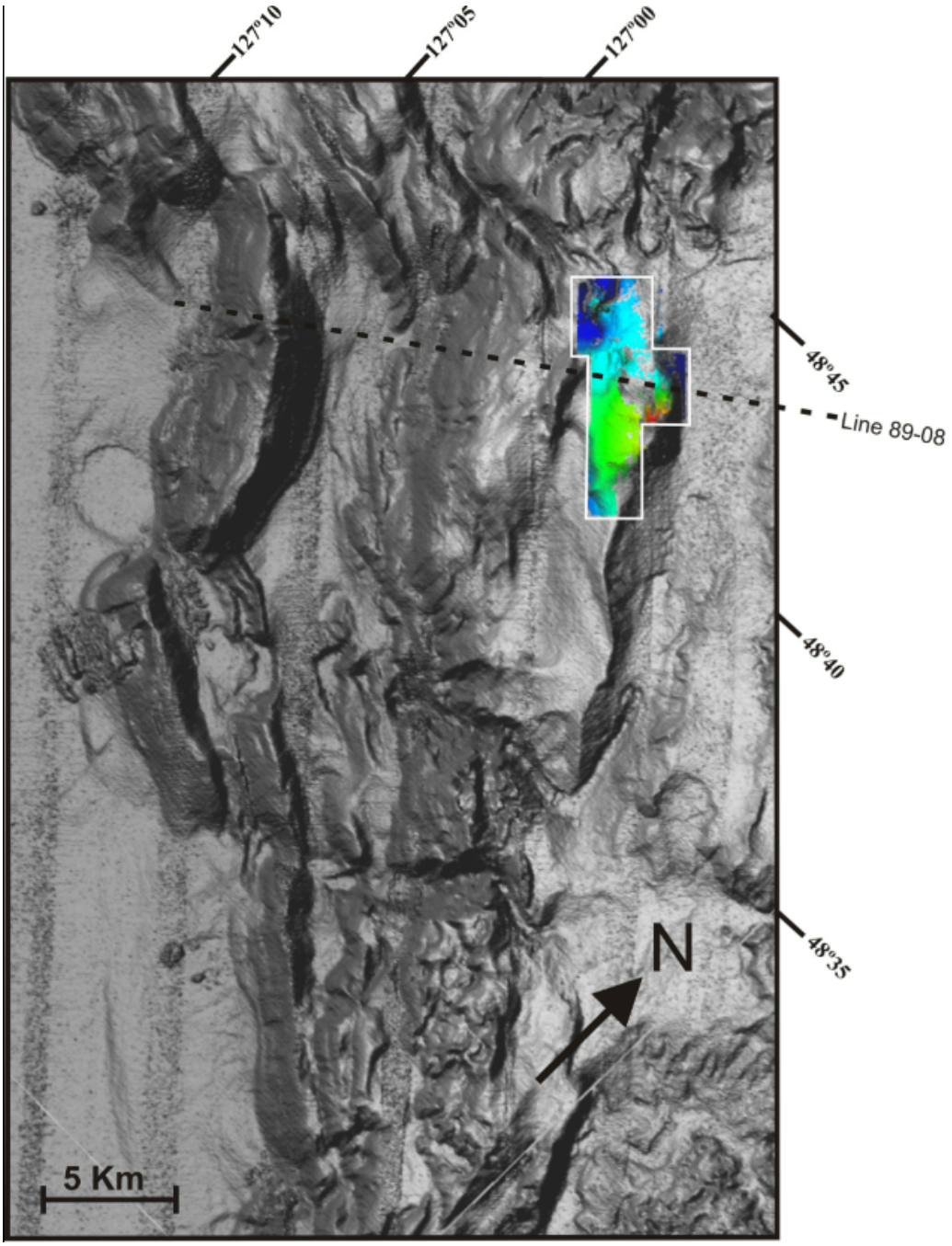

Figure 1.2 Regional Bathymetry Through Study Area

Regional Bathymetry through the area with high-resolution bathymetry shown inside white box. Line 89-08 (Figure 1.3) passes through the study area. The gray scale does not accurately show depth as the image is "shadowed" to enhance the depict seafloor morphology. Depth through the area varies from 2500 m in the low planes of the continental rise (east portion of line 89-08) to 1200 m at the summit of eastern ridge in the white box (west portion of line 89-08).

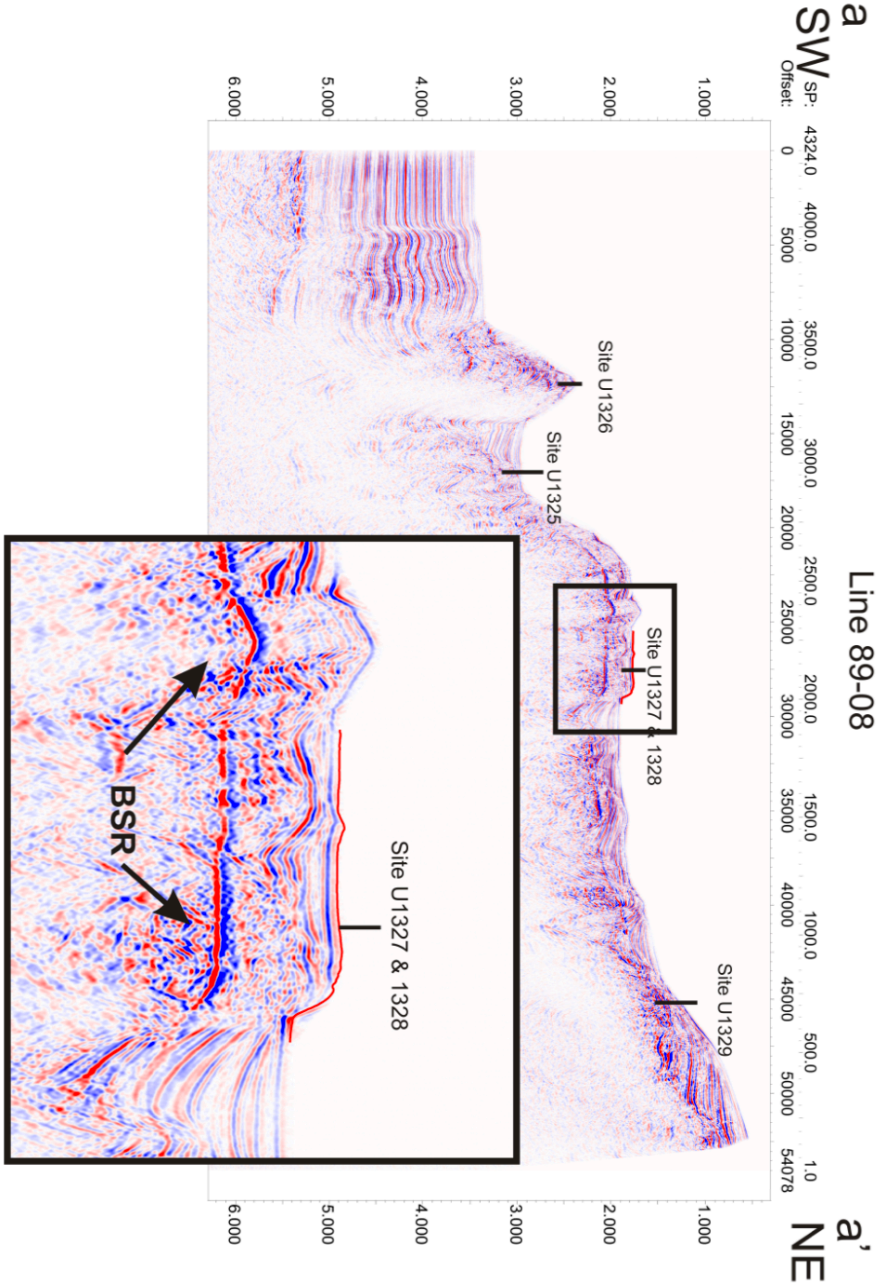

Figure 1.3 Seismic Line 89-08

A southwest to northeast transect across the accretionary margin. The AUV grid lies between shot points 2000-2400 on top of an accretionary ridge high. IODP drill sites U1325-U1328 are shown across the prism. Location of the high-resolution grid survey by the AUV is shown by thin red line. BSR is marked by polarity inversion 0.30 seconds (TWT) below the surface.

1.5 Previous Work

Offshore Vancouver Island on the northern Cascadia margin has been a focal point for geophysical studies since the discovery of a widespread bottom-simulating reflector (BSR) in 1985 (Davis and Hyndman, 1989, Hyndman and Spence, 1992). In seismic data, the BSR marks the base of the gas hydrate stability field and thus widespread occurrence of gas hydrate was hypothesized (Davis and Hyndman, 1989). Additional multichannel seismic data were acquired in 1989 (Hyndman, 1995). In 1992, Ocean Drilling Program (ODP) Leg 148 drilled several wells through the gas hydrate zone (Westbrook et al, 1994). Since that time, additional more detailed geophysical studies include: surface-towed single- and multi-channel seismic surveys (Yuan et al., 1996; Yuan et al., 1999; Fink and Spence, 1999; Riedel et al., 2002); deep-towed high-resolution seismic (DTAGS) studies (Chapman et al., 2002; He, 2007); Ocean Bottom Seismometer (OBS) studies (Hobro, 2005; Zykov, 2006; Lopez, 2008; Dash, 2011), ship-mounted high-resolution (12 kHz) acoustic echo-sounder surveys (Riedel et al., 2002), 3.5 kHz sub-bottom profiling (Riedel et al., 2002; Zykov and Chapman, 2000); electrical surveys (Yuan and Edwards, 2000; Schwalenberg et al., 2005); swath bathymetry mapping (Zuehlsdorff and Spiess, 2004); heat flow studies and seafloor piston core programs (Riedel., 2002; Riedel et al., 2006; Novosel et al., 2005). Additional comprehensive summaries of the literature for the Cascadia margin are found in many of the papers previously listed (e.g. Hyndman et al., 2001; Spence, 2010; Hyndman, 2011; Riedel et al., 2010).

The ODP Site 889/890 at the Northern Cascadia provided a first baseline of chlorinity profiles, electrical resistivity measurements, and down-hole acoustic velocities to estimate gas hydrate concentration in the subsurface (e.g. Hyndman et al., 1999; Kastner et al., 1995; Yuan et al., 1996).

In 2005, the Integrated Ocean Drilling Program (IODP) Expedition 311 returned to the margin and recovered 1217.76 m of core through a total of five drill sites (U3125-U3128) across the entire margin along a main drilling transect (Riedel et al., 2010). Figure 1.3 shows the location of IODP Expedition 311 drill sites along line 89-08; specifically, Sites U1327 and U1328 lie within the study area of this MSc thesis project. The presence of shallow hydrate is confirmed at drill site U1328, and by piston coring around this feature (e.g. Novosel, 2005; Solem et al., 2002; Riedel et al., 2006). Drilling revealed discrete gas hydrate layers in sandy lithology containing hydrate concentrations up to 80% of pore space with the largest concentrations of hydrate in the shallow sub-surface below 100 m depths. Site U1328 revealed a gas hydrate cap that extended from the surface to ~40 meters below sea floor (mbsf) (Riedel et al., 2010). These results were in contrast to predictions from Hyndman and Davis (1992) who hypothesised maximum hydrate concentration directly above the bottom simulating reflector (BSR).

Most recently, Dash and Spence (2011) produced a hydrate-saturation model utilizing ocean bottom seismometer (OBS) data in the same study area as this thesis. The prediction from their study was a linear increase in gas hydrate concentrations from 0 to 26% of the pore space at Site U1327 between 60 and 230 mbsf. Regionally they predicted an average hydrate concentration of 13% of pore space for 120 to 230 mbsf.

1.6 Project Data

In this thesis I investigate geophysical data acquired in 2009 during a collaborative cruise between Natural Resources Canada (NRCan) and the Monterey Bay Aquarium Research Institute (MBARI). The geophysical data were collected by MBARI's D. Allan B (Figure 1.4) AUV as the first component of a two-part cruise. The AUV mapped the seafloor near previously identified areas of interest, providing high-resolution bathymetric and backscatter maps. In a subsequent cruise in 2009, MBARI's Remotely Operated Vehicle (ROV) Doc Rickets (Figure 1.5) was used to complete seafloor observations and geologic sampling in the newly mapped regions. In addition to data collected from these two cruises with MBARI, other sources of data in this thesis include: seismic reflection data shot throughout the region (e.g. Line 89-08), seafloor video observations and a shallow sediment core taken from the seafloor acquired during a NEPTUNE-Canada cruise using the ROV ROPOS (Remotely Operated Platform for Ocean Sciences).

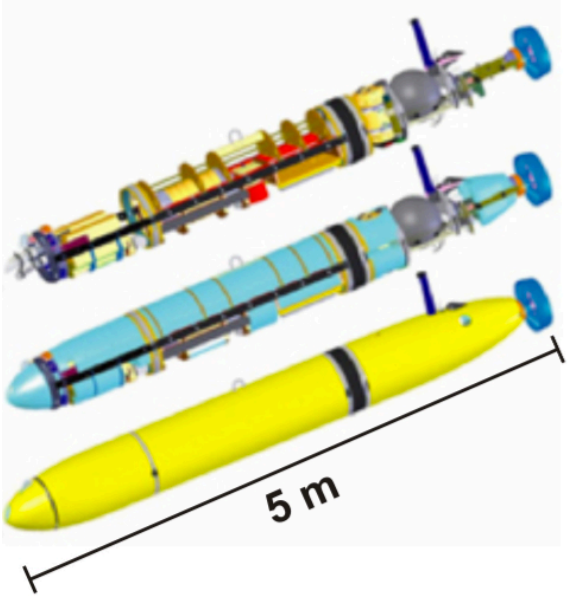

Figure 1.4 MBARI AUV Schematic

Schematic drawing of the AUV Dr. D Allan B (taken from MBARI website: http://www.mbari.org/auv/MappingAUV/vehicle_specs) showing instrumental internals and shell exterior.

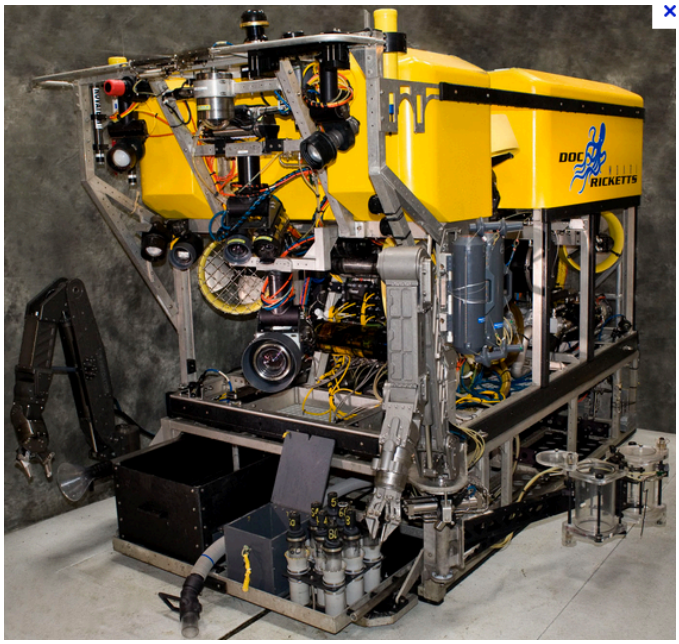

Figure 1.5 MBARI's ROV Doc Rickets

Image of MBARI's ROV Doc Rickets (taken from MBARI website: http://www.mbari.org/dmo/vessels_vehicles/Doc_Ricketts/Doc_Ricketts.html)

MBARI's D. Allan B. AUV is a 5 m long torpedo equipped with an electrical propulsion engine and an electric navigation system. The AUV carries a collection of mapping sonars that operate simultaneously. The multi-beam sonar collects bathymetry information for seafloor relief maps. There are two side-scan sonars (one on each side of the tool) that image the seafloor and are capable of resolving small-scale structures (cm scale) while also characterizing seafloor hardness. The 2-16 kHz sub-bottom profiler sonar images the structure beneath the seafloor allowing for inspection of sedimentary layers and other small-scale structures. The AUV operates in a "lawnmower" fashion by making side-by-side passes of the area with additional perpendicular tie-lines to confirm bathymetric values between adjacent lines. Bathymetry resolution strongly depends on how close the sonar source and receivers are to the seafloor; MBARI's D. Allan B can flies routinely 50 m above the seafloor. For more information on the mechanics, operation, and collected data from the AUV module, see Chapter 3.

Due to the high frequency of the sub bottom profiler, much of the energy is lost due to attenuation in the sediments. This loss of energy restricts the AUV image to only the top of the sediment column. In this study area, AUV seismic penetrates to only a fraction of the depth (10-15%) of lower frequency streamer-towed multichannel seismic in the region (Figure 1.6).

In this study I also examine photo images of the seafloor acquired from both MBARI's 2009 and 2011 cruises to the Cascadia margin where the ROV Doc Rickets operated in our seafloor study area, as well as from the 2011 cruise by NEPTUNE-Canada using ROPOS.

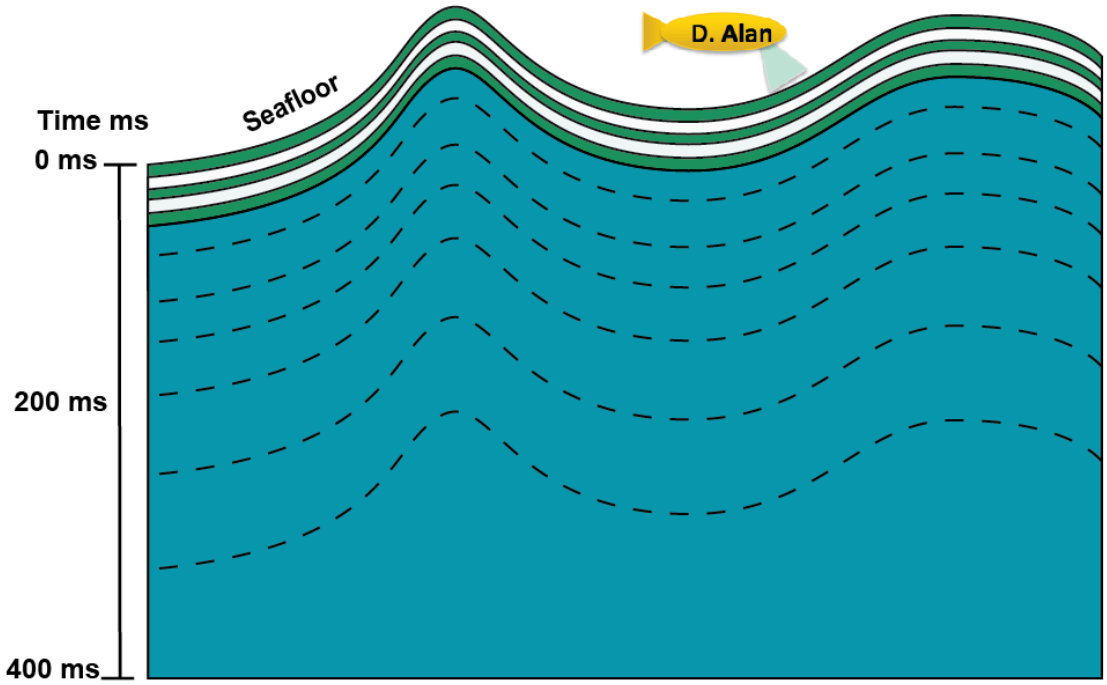

Figure 1.6 Illustration of AUV Penetration Depth

The AUV has a shallow penetration depth, 10-15% (top white and green, 0-50 ms) compared to streamer-towed multi-channel seismic (times > 50 ms). However the AUV images the near-surface sediments at a much higher resolution due to its high frequency.

2 Regional Geology and Cold Vents

This chapter discusses the regional geology in the study area. The tectonic controls on geological processes are presented, as well as the sources of sediment involved in the formation of the Cascadia Accretionary Complex and the overlying slope sediment layers. Accretionary prism mechanics are introduced to give an appreciation for how active sediment deformation and fluid venting matures across the prism (i.e., from the continental rise, through the slope, and onto the continental shelf). Finally, cold vents are discussed, including the history and discovery of cold vent communities, the components that make up cold vents, (i.e. authigenic carbonate, chemosynthetic biological communities), and the pressure-temperature conditions that control hydrate stability.

2.1 The Cascadia Margin

The Cascadia Margin is a tectonically active margin where subduction of the oceanic Juan de Fuca plate results in a large accretionary prism. In this section I discuss the history and geographic extent of subduction on the margin and outline subduction characteristics necessary for accretionary prism formation. The foremost characteristics are: tight plate configuration that does not allow significant trench development, and ample sediment supply to the margin.

2.1.1 Tectonics

The contact between the Pacific plate and the North American Plate along the west coast of North America is predominately a right-lateral transform boundary. The transform boundary extends from southern California to Cape Mendocino, and again from Queen Charlotte Sound to the Aleutian Trench of Alaska (Hyndman, 1995). Between these boundaries the continental margin is a subduction zone (Figure 2.1). The subducting Juan de Fuca plate is what remains of the previously large Farallon plate that was mostly consumed through the continuous convergence of the East Pacific Rise with North America (Atwater, 1970). The resultant active margin is formed through the nearly orthogonal subduction of the Juan de Fuca plate beneath the North American plate. In the study area, subduction rates of the Juan de Fuca plate beneath the North American plate are estimated at 45 mm/year (Riddihough, 1984; Engebretson et al., 1985). A review of the plate regime off Vancouver Island was provided by Davis and Hyndman (1989) and Riddihough and Hyndman (1991). The most recent estimates of plate velocities in the region, based on a decade of GPS measurements, were provided by Mazzotti et al. (2003).

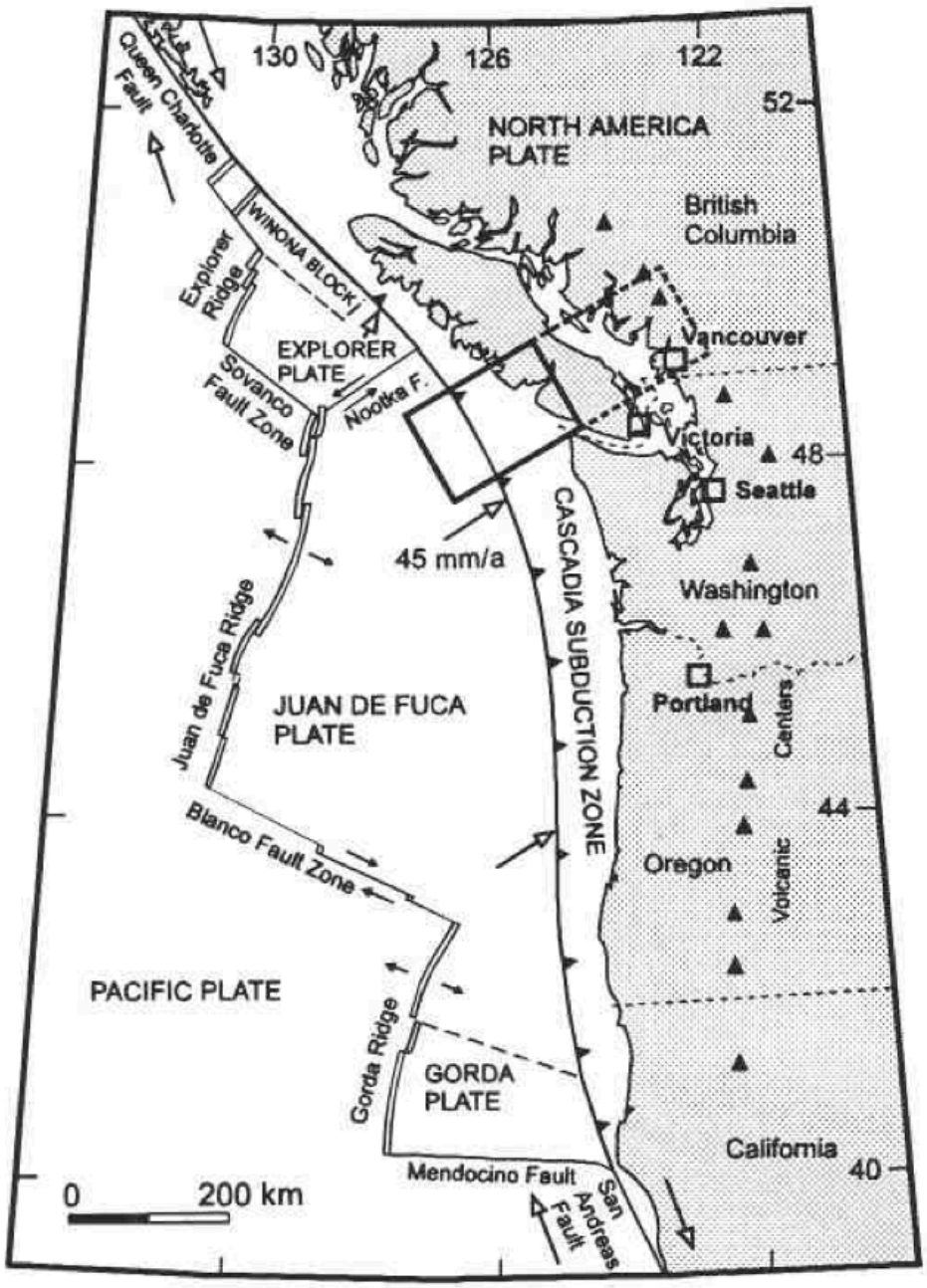

Figure 2.1 Subduction Tectonics of the North West Pacific

This illustration depicts subduction zone tectonics of the Cascadia margin with its subducting Juan de Fuca plate. The solid box shows the location of offshore Lithoprobe survey (taken from Hyndman et al., 1995).

The Cascadia subduction zone provides the characteristic elements of subduction zone tectonics as defined by Hyndman (1995). These elements include (1) inland active volcanoes from southern British Columbia to northern California; (2) continental and subducting plate seismicity; (3) low heat flow within the foreland, and sharp heat flow increases closely seaward of the volcanic arc; (4) low-high gravity trends, with low gravity values above trench and high values over the edge of the continent; (5) broad accretionary prism from a steady influx and accumulation of marine sediments.

Central Cascadia margin convergence has been continuous since the Eocene (56 Ma) (Riddihouh 1982, Engebretson et al., 1985, Wilson 1988). Roughly 43 Ma years ago two narrow terranes were emplaced on the Cascadia margin, the Eocene marine volcanic Crescent Terrane, and the Mesozoic marine sedimentary Pacific Rim Terrane. The Crescent Terrane acts as the landward barrier for the accreted sedimentary prism accumulated since the Eocene (Hyndman et al., 1995). In the Tofino Basin up to 4-km-deep of Eocene and Holocene sediments were deposited over the accretionary wedge and above the two accreted terranes. The Tofino Basin extends over the continental shelf of Vancouver Island containing former slope basins, deep sea turbidites, and hemipelagic sediments (Hyndman, 1995). The Cascadia subduction zone lacks a bathymetric subduction trench due to the high rate of sediment fill in the basin. Additionally plate roll-back velocity is less than overriding plate velocity allowing for a tight plate configuration, (i.e., compressional plate contact), and also limiting oceanic trench development (Humphreys and Coblentz, 2007). These mechanical characteristics of plate contact in addition to high amounts of marine and terrigenous sediment input are the basic components for accretionary prism development. Hyndman (1995) provides an

interpreted illustration of the different subduction zone elements from seismic line 89-08 (Figure 2.2). These subduction zone elements including but not limited to Cascadia Basin sediment fill, dipping oceanic crust, accreted terranes, foreland basins, and structural elements including thrust faulting and folds. Line 89-08 bisects the study area and the northern Cascadia accretionary complex (Figure 2.3).

2.1.2 Sediment Supply

To create an accretionary margin, sediments must accumulate onto the overriding plate by off-scraping from the subducted oceanic plate. The eastern flank of the Juan de Fuca Ridge has a smooth topography and thus a smooth subduction surface. Rougher terrain (associated with seamounts) is characteristic of the western flank of the ridge (Davis and Karsten, 1986). Seaward of the deformation front, the subduction trench is almost completely filled by sediments forming the Cascadia Basin. The highest sedimentation rates are off southern Vancouver Island resulting in the thickest sediment package of the Cascadia subduction zone (4.5 km), which decreases southwards off Northern Washington (3.75 km), Mid Oregon (3.5 km), and Northern California (2.7 km) (Hyndman and Wang, 1995). Basin fill is predominantly pre-Pleistocene fine-grained hemipelagic sediment. These sediments are overlain by a rapidly deposited and layered Pleistocene turbidite section of significantly coarser material. The thickness of the turbidite section is controlled for the most part by the thickness of the underlying pre-Pleistocene sediments. The high rates of sediment deposition during the Pleistocene was sufficient to maintain Cascadia basin fill and maintain a topographic height comparable to that of the Juan de Fuca Ridge system. The majority of incoming sediments from the

Juan de Fuca plate are scraped off and form long accretionary ridges that strike parallel to the subducting plate. More recent bathymetry data show that while average strikes are orthogonal to plate subduction at regional scales (>10-15 km), at finer scales ridge strikes will deviate 30-40 degrees, and ridges <2 km in length have no visible directional preference (Figure 2.3). The study area of this thesis lies between two closely spaced accretionary highs within a shallow depositional basin. The basin is 350 m deep and lies atop deformed Cascadia basin sediments. The top 128 m of sediments consist of clay-silt packages that are intermittently deposited with fine sand turbidites (Westbook et al., 1994).

2.2 Accretionary Prism

The Cascadia convergent margin allows studies of the impact of rapid sedimentation on the mechanics of subduction zone accretion. Intensified sedimentation from glacial periods resulted in a high Quaternary growth rate with landward thrust faulting rarely observed in other accretionary wedge settings. Sediments of the 2-3 km thick Cascadia Basin are carried eastward and scraped off the underlying oceanic crust to form the accretionary prism. The accretionary prism is 5-8 km thick at the continental slope, and becomes thicker to the east. The prism can be viewed as a proto-fold and thrust-belt, and can be studied as an evolving accretionary system to be compared to geological analogs on land. Processes studied include folding, thrust faulting, compaction, fluid expulsion, and thermal metamorphism (Hyndman et al., 1995).

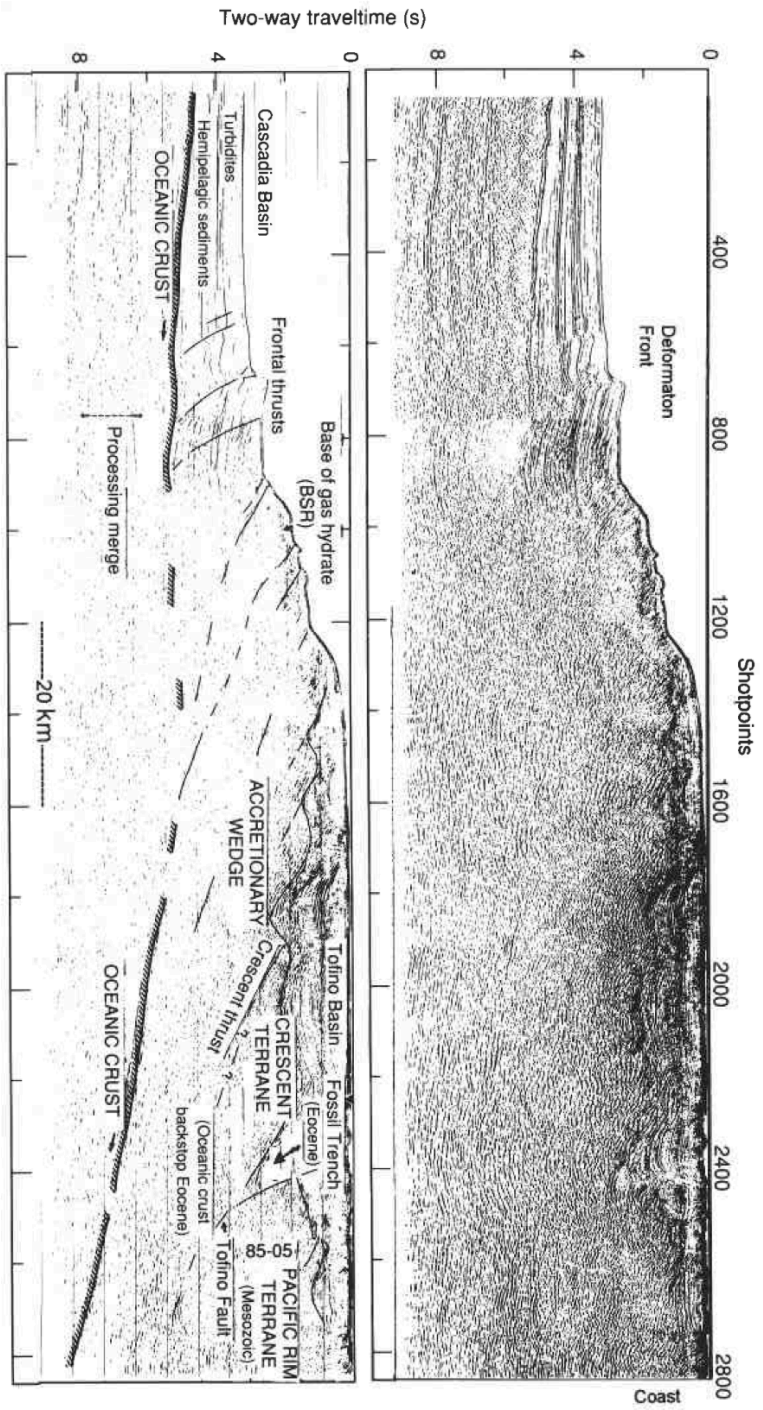

Figure 2.2 Tectonic cross section through the northern Cascadia Margin

Tectonic interpretation of line 89-08 from Hyndman (1995) showing accreted terranes (Pacific Rim, Crescent), Cascadia Basin sediments, wedge development, inferred faults, folds, and dipping oceanic plate.

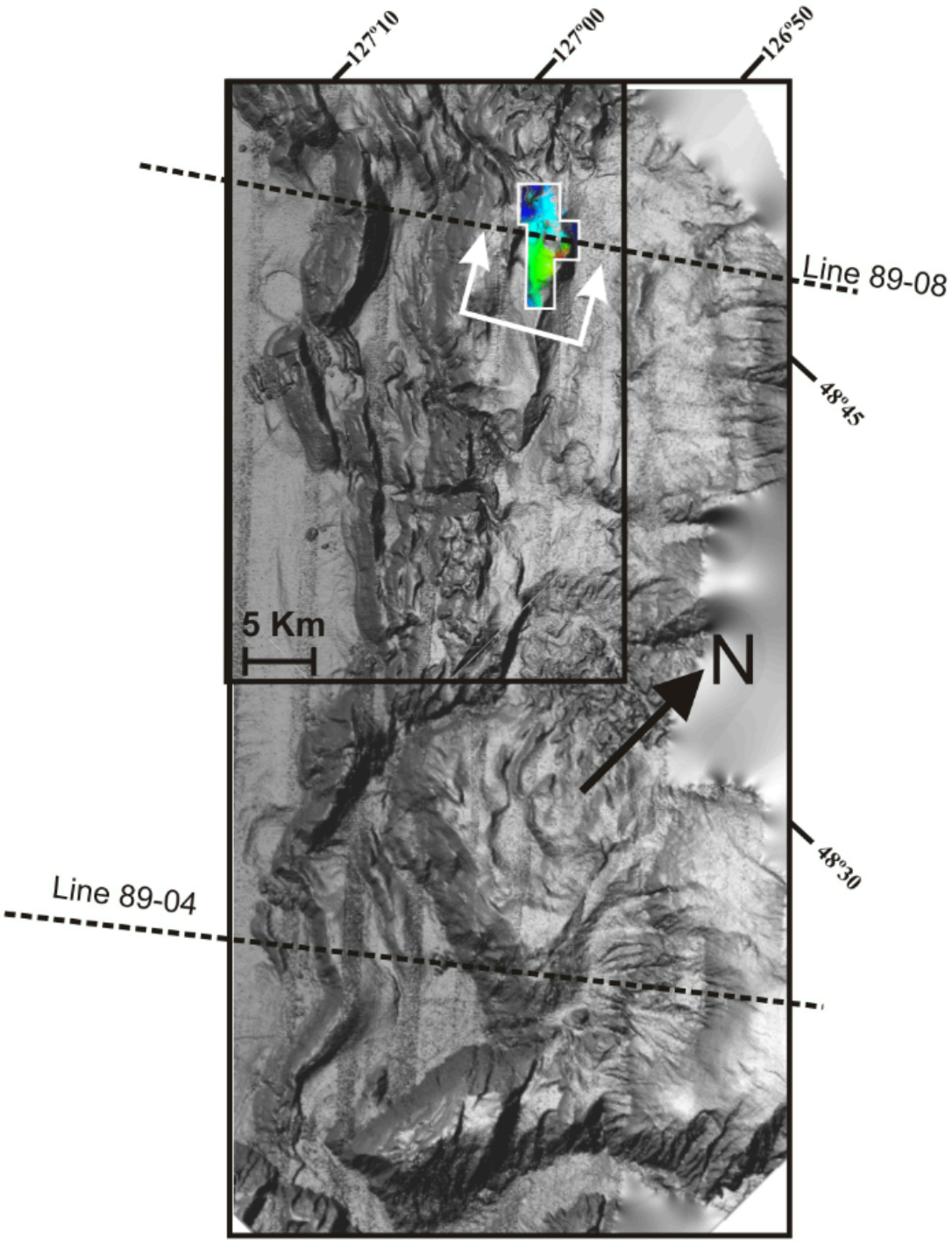

Figure 2.3 Regional bathymetry across accretionary wedge

High-resolution survey lies between two structural highs (white box). Line 89-08 runs roughly perpendicular to anticlinal ridges across the margin. Elongated anticlinal ridges show pervasive strike throughout the region with variations becoming more apparent as ridge size decreases. White arrows show the viewing direction and location of Figure 2.4.

2.2.1 Accretionary Prism Mechanics

The crust of the Juan de Fuca Plate that is now being subducted is young (5-7 ma), buoyant, and maintains a shallow landward-dipping angle of ~3° at the deformation front. This shallow-dipping angle inhibits the development of a trench and further contributes to the formation of a large accretionary prism. Water depths at the base of the continental slope do not exceed 2.5 km (Hyndman et al., 1995).

Through the critical taper theory for accretionary prisms, two elements of prism mechanics can be inferred. (1) The first element is that the shape of the prism is controlled by sediment and pore fluid properties within the prism (Hyndman et al., 1995). Using classical critical taper theory, Davis et al. (1983) showed that the shape of the accretionary prism is dictated by contact friction between sediment grains where there is insignificant sediment cohesion (Coulomb behaviour). The bathymetric slope of the accreted sediments is a function of the dip of the décollement layer and the pore fluid pressures within the prism. Therefore, a change in taper angle of the prism (décollement dip plus surface slope) from west to east over the prism may be indicative of a change in fluid pore pressure (Davis and Hyndman 1989, Hyndman et al., 1993). Recently, in an update of the classical critical taper theory, Hu and Wang (2008) and Wang and Hu (2006) proposed a dynamic Coulomb wedge model, which addresses the effects of strength changes along the megathrust fault during great earthquakes.

(2) The second important aspect to critical taper theory is that the décollement dip angle may control whether the surface slope grows upwards (a positive surface slope) or whether it subsides to form a forearc basin. The maximum taper angle for a positive landward slope of an accrectionary margin appears to be 11 degrees (Davis and Hyndman

1989). For slope >11°, prism slopes become negative and a forearc basin will form. For southern Vancouver Island the Tofino Basin forms as the 11° taper threshold is achieved 50 km seaward of the deformation zone. For the Olympic Peninsula, the threshold of 11° is not reached until 200 km east of the deformation front. This has allowed the prism to grow upwards creating the Olympic Peninsula (Hyndman , 1995).

2.2.2 Deformation

Maximum sediment deformation occurs at the base of the continental slope; sediments are folded and faulted creating elongate anticlinal ridges. Seaward vergent thrust faults are typical for the narrow slopes off Vancouver Island's accretionary wedge; however, thrust faults become more landward vergent to the south (northern Oregon and Washington) where glacial sediment accumulation was higher (Adams et al., 2004). Ridges protrude as high as 700 m above surrounding sea floor, extend 20-30 km in length, and are between 2-3 km wide. Figure 2.4 shows the accretionary ridges in the region of my study area. The more eastern ridge has an azimuth of 317°, and the more western ridge just outside this study area has an azimuth of 326°. Anticlinal axes have structure roughly continuous along axis with the amount of shortening decreasing from their centers towards their plunging ends.

The décollement of the accretionary prism is near the base of the sediment section and is imaged on multichannel seismic data (Figure 2.2) as a strong reflector at the top of the oceanic plate, landward of the deformation front (Hyndman, 1995). Further south, Oregon's décollement is above the top of ocean crust and a component of the sediment section is subducted to unknown depths. Shortening accommodated through faulting is

rarely visible on the seafloor, since surface expressions of faults are most likely covered by their hanging wall anticlines, or covered by local erosional debris (Davis and Hyndman, 1989).

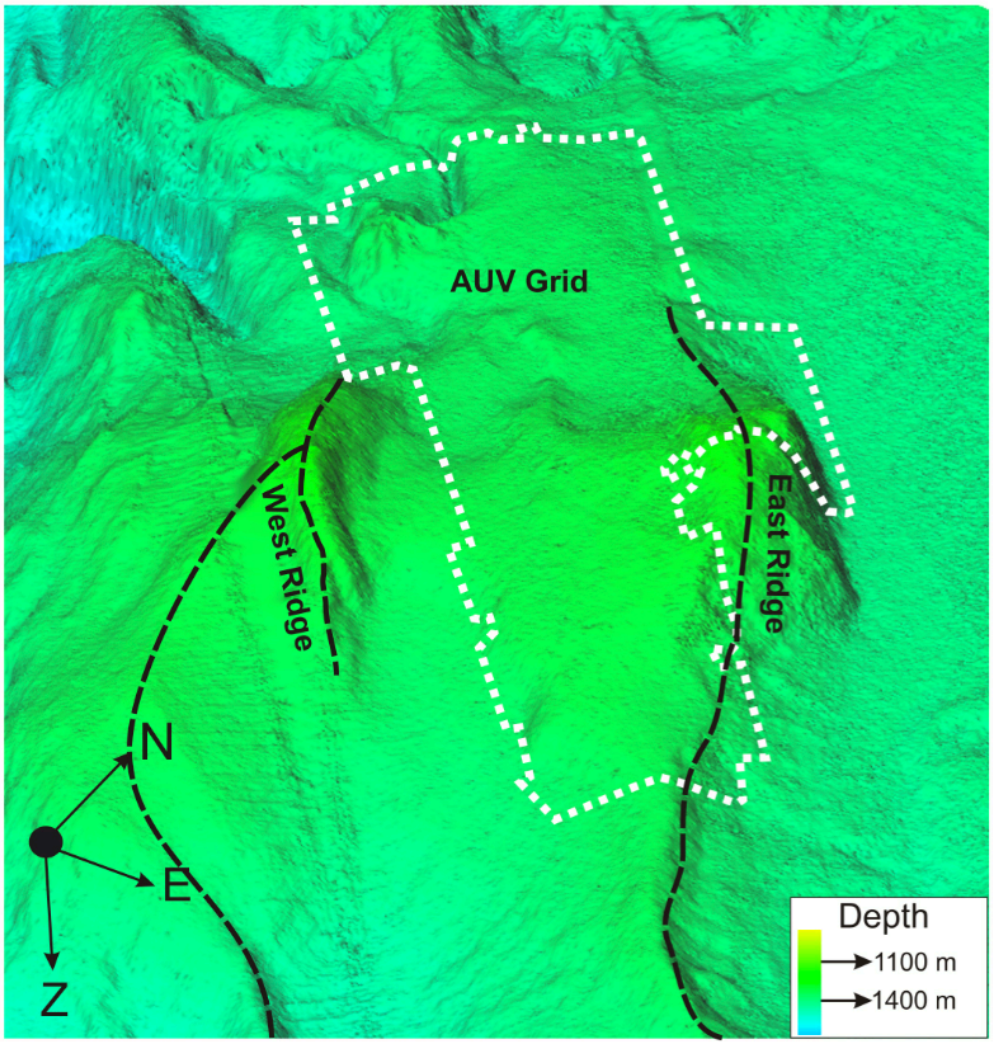

Figure 2.4 Accretionary ridges of the study area

The survey area is bounded by two accretionary ridges; the western ridge is orientated 326°, and the eastern ridge is orientated 317°. The azimuths are averaged from the regional strike of the ridge through the region. The high-resolution AUV grid is shown outlined by the white polygon. The dashed black lines outline the summits and potential axis of the accretionary ridges in the area.

2.2.3 Fluid Advection Variations Across The Prism

Fluid venting is variable across the accretionary prism. Internal properties of the prism have been inferred through the development of thermal models (Hyndman and Wang, 1993) and velocity models (Yuan et al., 1994). IODP Expedition 311 further enhanced the understanding of fluid advection rates across the Cascadia margin (Riedel et al., 2010-X311Synthesis).

Hyndman and Wang (1993) explored tectonic sediment thickening and fluid expulsion along the Cascadia accretionary prism by modelling the regional heat flux, which included variations in bottom simulating reflector (BSR) depths and porosity. The BSR marks the limit of the gas hydrate stability (the nature of BSRs is discussed in more detail in Section 2.3.3). Pronounced depressions in the predicted BSR depth account for reductions in heat flow (e.g. Ganguly et al., 2000; Riedel, 2001). Regional tectonic forces cause lateral compression of the sediment forcing the sediments to accommodate by stretching vertically. This shortening of sediment results in a vertical stretching of the sediment isotherms. This phenomenon is characteristic of the seaward section of the prism. Further inland, heat flow is re-established from the re-genesis of fluid expulsion and the upward advection of heat. While sediment thickening from shortening reduces heat flow, fluid expulsion from compaction increases heat flow. Model predictions give maximum fluid expulsion rates of 1.3 mm a^{-1}, from 25-30 km landward of the deformation front (Hyndman and Wang, 1993).

Yuan et al. (1994) utilized multi-channel seismic for an in-depth velocity analysis to estimate pore fluid expulsion. Under normal consolidation environments, sediment porosity changes are approximately exponential with depth (Athy's Law). Cascadia Basin

sediments fit this approximation; porosity-depth profiles become irregular as you move from basin to shelf. Approximately 30% of total fluid volume is lost as the sediments are accreted onto the wedge (just seaward of the deformation front). As the sediments are accreted and stretched vertically, the rate of tectonic thickening is faster than the rate of fluid expulsion. The lag in fluid expulsion results in pore fluid pressures that are higher in slope sediments than for sediments at similar depths in the basin. Due to the high fluid pressures and rate of deformation the sediments of the accretionary wedge can be described as under-consolidated. Time lags for fluid expulsion within the prism are on the order of 0.2-0.4 m.y. (Yuan et al., 1994). High sediment pore pressures associated with the lower slope contribute to the low sediment velocities associated with the area. Figure 2.5 shows interval velocities across the prism from seismic line 89-04 (location shown in Figure 2.3). IODP Expedition 311 (56 km north of line 89-04) showed a fluid advection rate increase landward of the deformation front (Riedel et al., 2010), but regional advection rates are not uniform and pervasive as previously thought. Figure 2.6 shows updated knowledge of changes is fluid expulsion rate (dashed line) and cumulative fluid expelled (solid line) across the prism. Exploration drill sites are shown on line 89-09 in Figure 1.3.

He (2007) modeled heat flow variations 20-25 km from the deformation front using single-channel seismic and deep-towed multichannel seismic data, in a region that included the study area of this thesis. With regional heat flow calculated from variations in the depth of the BSR, He (2007) determined heat flow variations through the region with a two-dimensional analytical correction for the effect of topography. His findings show that fluid flow across the prism is influenced by sediment heterogeneity and

structural factors. With updated venting measurements from IODP Expedition 311, Riedel et al., (2010) illustrated some of the complex nature of fluid expulsion across the accretionary prism (Figure 2.7). The illustration depicts how sedimentation rates, diagenesis, metamorphism, and structural features contribute to the advection rates encountered throughout the prism.

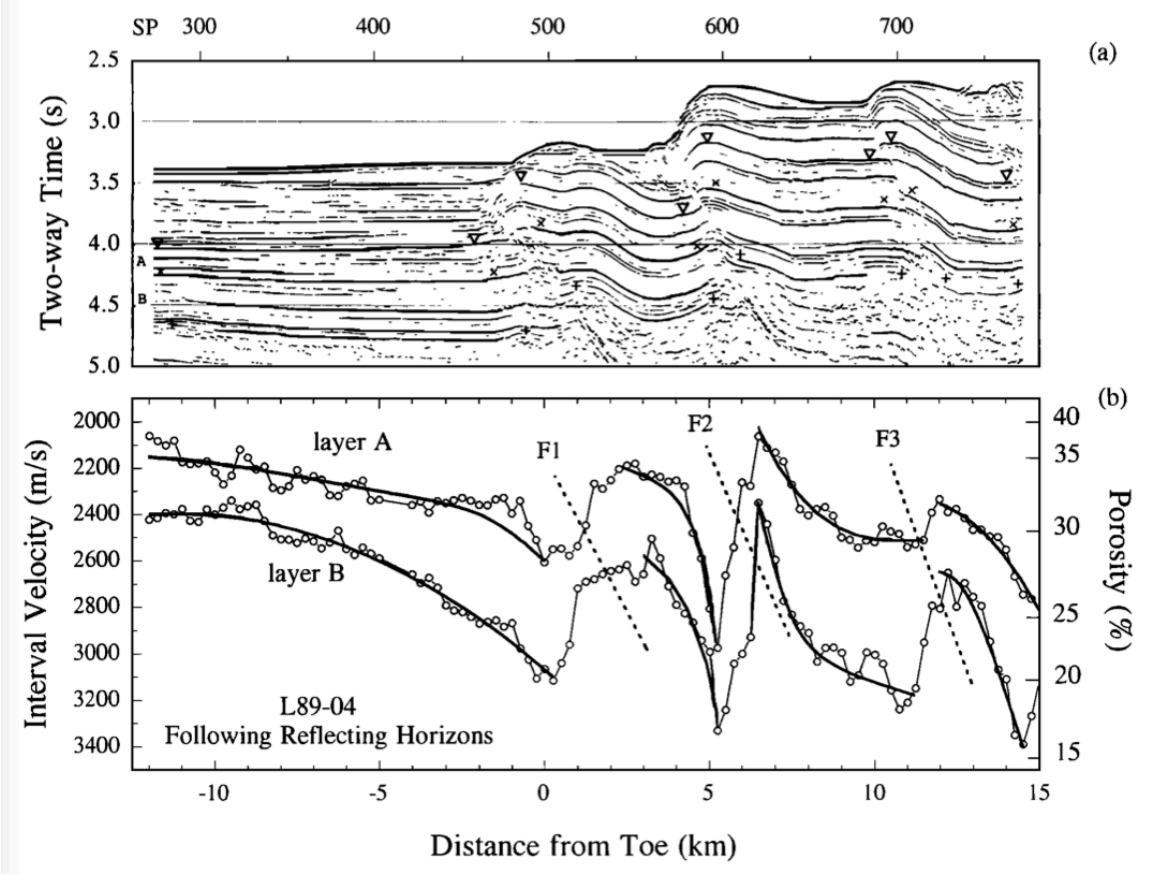

Figure 2.5 Accretionary wedge interval velocities and porosities

Wedge velocities and porosities are shown with variations from basin to slope. (a) Migrated seismic line (L89-04) showing a layered stratigraphic section becoming faulted and vertically stretched as it passes the "toe" of the accretionary margin. Faults dip landwards and turbidite layers A and B are evaluated for their interval velocities. (b) Interval velocities and interpreted porosities for turbide layers A and B. Location of faults F1, F2, and F3 carried from above (Yuan et al., 1994).

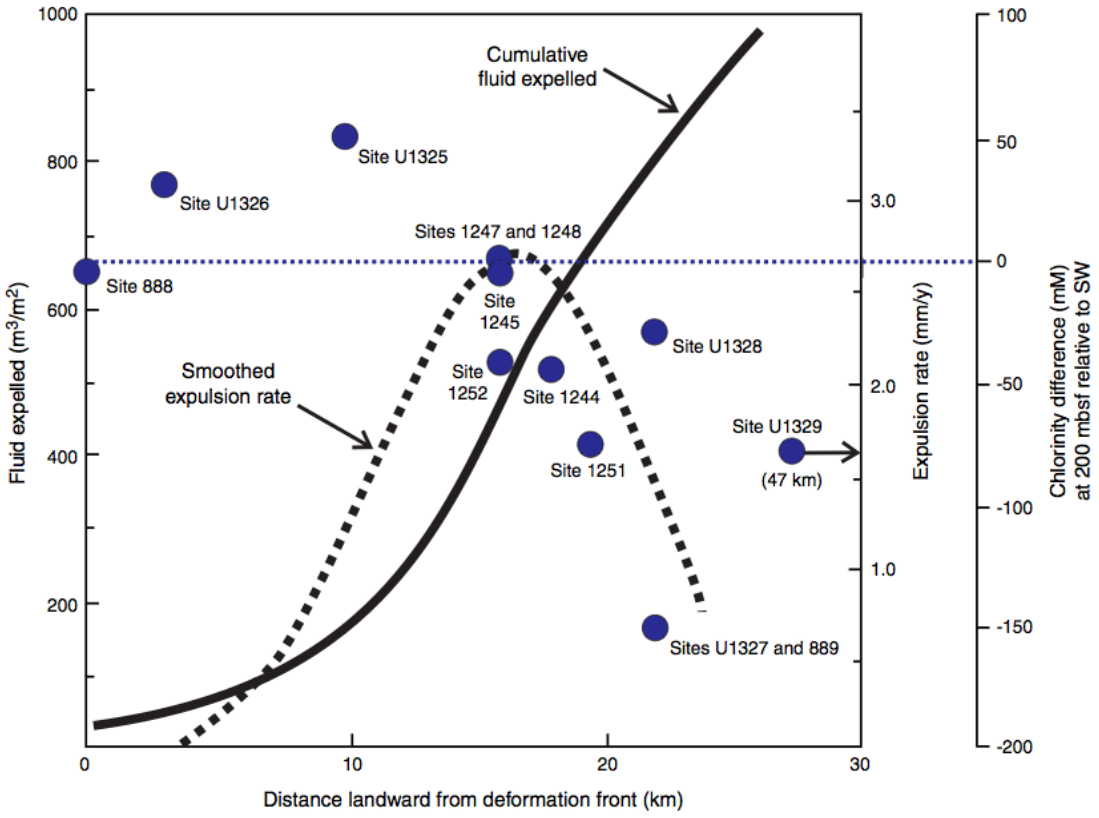

Figure 2.6 Fluid expulsion rate and total fluid expulsion across the prism.

This illustration shows variations in fluid expulsion rate and total fluid expelled across the prism. The dashed line shows smooth expulsion rate and the solid lines shows accumulative fluid expelled. Sites U1328 and U1327 are landward of the maximum fluid expulsion rate with low pore water chlorinity compared to the seafloor (Riedel et al., 2010).

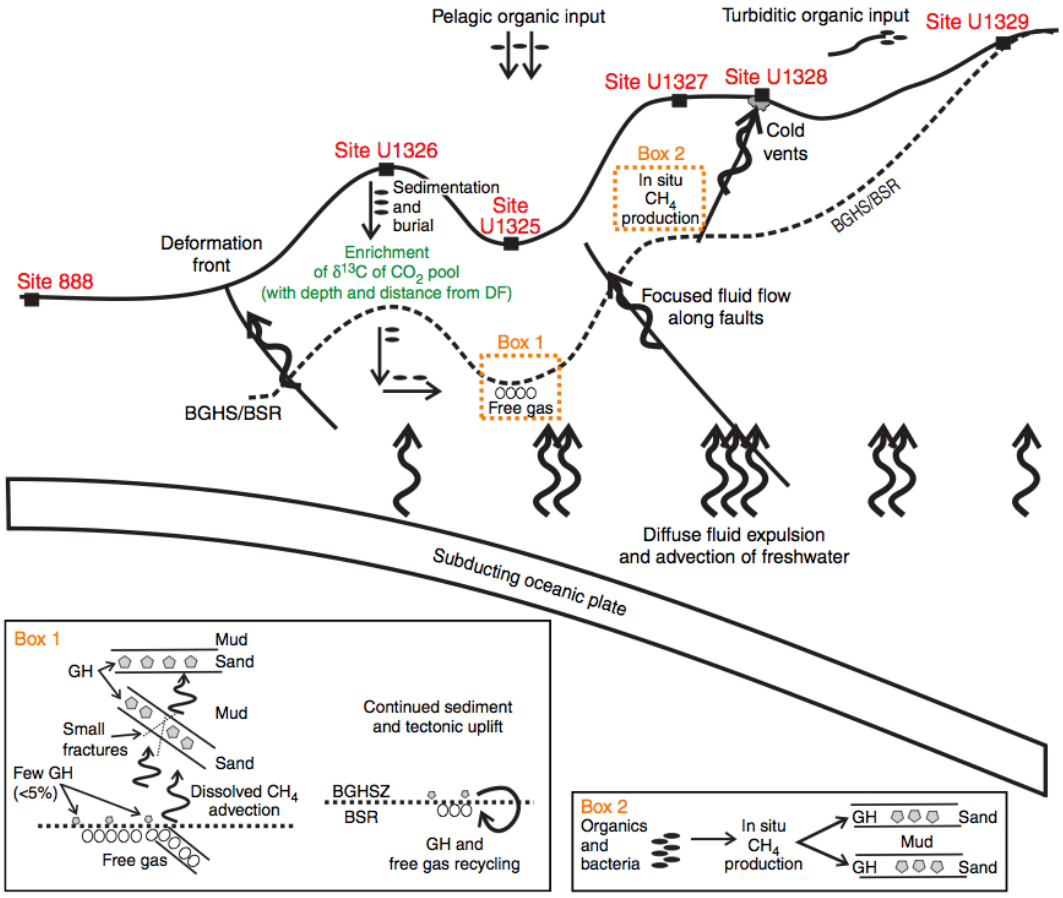

Figure 2.7 Complexity of fluid flow across the margin illustration

Illustration showing the complexity associated with fluid flow across the accretionary margin. Tectonic uplift, sedimentation rates, diagenesis, metamorphism, and structural features all contribute to variations in fluid advection and analogously the prism's thermal character (Riedel et al., 2010).

2.3 Cold Vent Dynamics

Cold vents are the surface expression of fluid or gas escape from the subsurface into the ocean. These venting sites are comparatively "cold" compared to high-temperature hydrothermal vent systems (>100°C) present at mid-ocean ridges. Cold vent temperatures are usually near the same temperature as the seawater they inject into:

Torres et al. (2002) measured in situ temperature variations of <0.2°C over ~1 m of push core. The presence of a cold vent is an indicator of increased fluid or methane flux regionally, locally, or both; vent presence can be used as a visual indicator of increased pore pressures (in excess of hydrostatic) at depth. Visually, vent presence is marked by chemosynthetic biological communities (CBC), seafloor authigenic carbonate, bubbling of hydrocarbons and/or hydrocarbon slicks (e.g. Boles et al., 2001; Orange et al., 2002; De Beukelaer et al., 2003). Depending on the stage of venting and location, some or all of the listed may be present. Migration can occur both horizontally and vertically depending on the in situ pressure conditions. Lithostatic loading (see Section 2.2) and methane generation often lead to overpressured reservoirs.

2.3.1 Methane Generation

The methane is derived through either thermogenic or biogenic processes, and sometimes both methane sources are encountered. Biogenically produced methane is a diagenetic process that occurs from the breakdown of deposited organic matter through methanogenesis (Claypool and Kenvenvolden, 1983). Equation 1 shows a simplified net reaction for methanogenesis producing the two redox end members of methane and carbon dioxide.

Equation 1: $2CH_2O$ (solid organic matter) $\rightarrow$ $CH_4 + CO_2$

Whiticar (1999) provides a detailed description of the chemistry and complexity of shallow methane generation. Organic material buried deep within the sediment section will be exposed to high temperatures and pressures. At these depths the sediment enters

the hydrocarbon window and thermogenic gas is produced. This catagenetic process (essentially baking of the rock) creates methane at temperatures above 100 °C and at depths 1000-2000 meters below seafloor (mbsf). These fluids may migrate to the surface where they can add to existing biogenic methane reservoirs. These gases often contain longer hydrocarbons chains (C_{2+}) in addition to methane and their presence indicates an over-pressured hydrocarbon reservoir at depth. The Gulf of Mexico, the Caspian Sea, the Black Sea and the Japan Sea all have significant thermogenic methane sources. The study area in this thesis is almost exclusively sourced by biogenic methane as concluded by IODP Expedition 311 (Riedel et al., 2006; Pohlman et al., 2009). Thermogenic sources of methane also exist along the margin: seafloor sediments in Barkley Canyon ~60 km southeast of this thesis' study area host gas hydrate structures II and H, and oil-stained gas hydrate (e.g. Pohlman et al., 2005).

2.3.2 Hydrate Stability

Gas hydrate is a form of clathrate structure where the guest molecule of gas is hosted inside an ice lattice. When gas hydrate forms naturally, the host molecule is almost exclusively methane; however, other gases (ethane, propane, carbon dioxide) can also be hosted. Three hydrate structures are observed to occur naturally: Structure I, II, and H. Structure I is the most dense, while II and H host larger molecules and are thus more typically encountered in thermogenic settings (Lu et al., 2007). For this study, and most studies involving gas hydrate, gas hydrate is synonymous with methane hydrate. The formation of hydrate requires cold temperatures and high pressures; marine

sediments satisfy these conditions due to cold bottom waters (~2.5-3.0 °C in this thesis' study area) and the pressure resulting from the overlying water column. Lithostatic pressures associated with the weight of the sediment column are neglected as determined through empirical measurements at ODP site 889 (Westbrook et al., 1994). The base of gas hydrate stability zone (GHSZ) is marked by the intersection of the geothermal gradient with the gas hydrate phase boundary. At greater depths, temperatures are too high for the stability of the gas hydrate structure. Figure 2.8 shows a typical phase boundary for gas hydrate in marine sediments. IODP Expedition 311 places the base of the GHSZ at a depth of 223 mbsf at site U1327, and 219 mbsf at site U1328 (Riedel et al., 2006).

The theoretical gas hydrate occurrence zone (GHOZ) extends from the base of the GHSZ to the sulfate methane transition zone (SMTZ). The sulphate methane transition zone marks the vertical limit of the reaction zone between the downward diffusing seawater-derived sulphate and upward migrating methane. The SMTZ is the zone of maximum anerorbic oxidation of methane (AOM). Figure 2.9 shows measured methane and sulfate concentration for IODP site U1327 and U1328. Site U1327 puts the SMTZ at ~8 mbsf in this study area and site U1328 places the SMTZ at ~2 mbsf. The depth of the SMTZ depends on environmental conditions (faults, sediment permeability, advection of methane), and where fluid advection rates are high enough, the SMTZ may extend to the seafloor where methane escapes sediments and bubbles away. Figure 2.10 is an illustration showing the relationship between the methane advection rates and the position of the SMTZ.

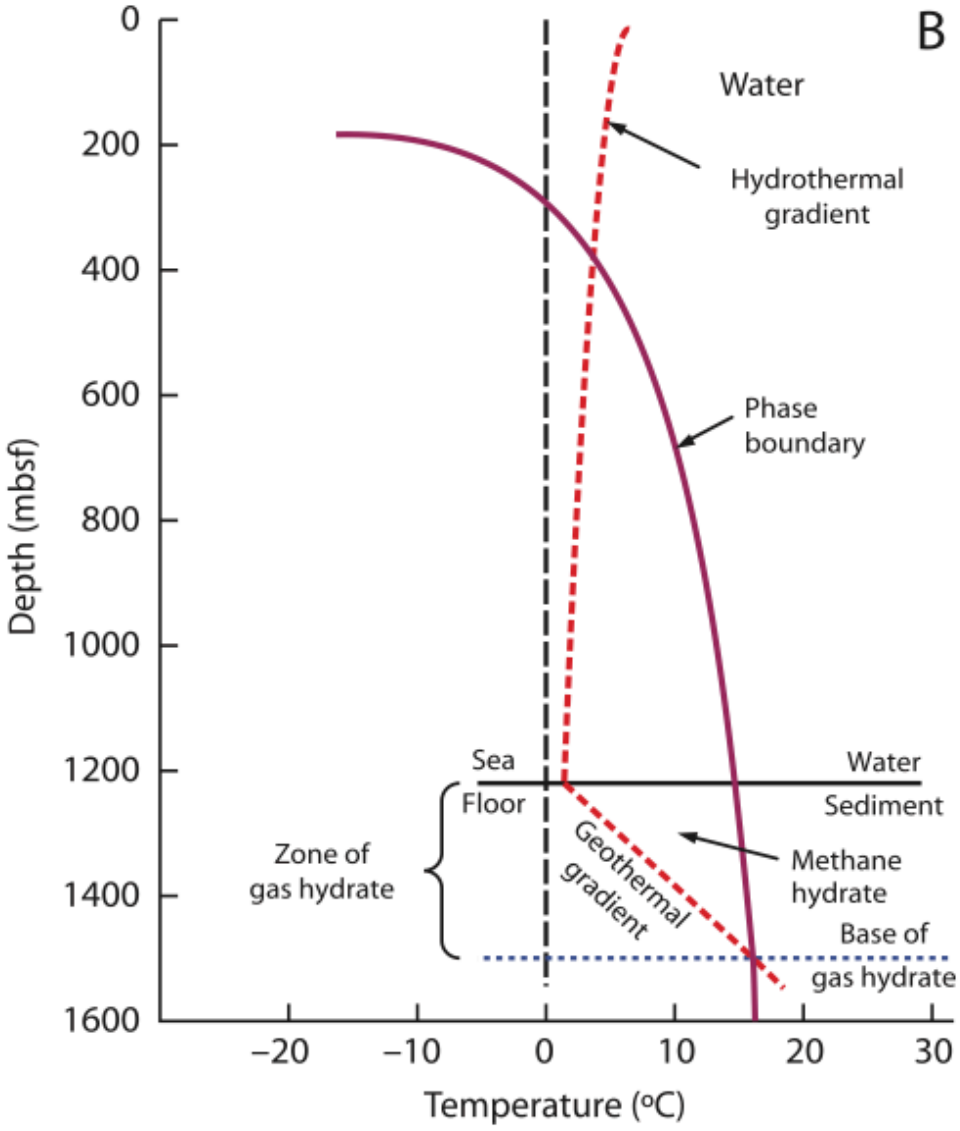

Figure 2.8 Marine gas hydrate stability

This figure provides a generic example of depth-temperature conditions for which gas hydrate is stable for marine sediments (Collett et al., 2009). The base of the gas hydrate occurrence zone is marked by the intersection of the geothermal gradient with the gas hydrate phase boundary.

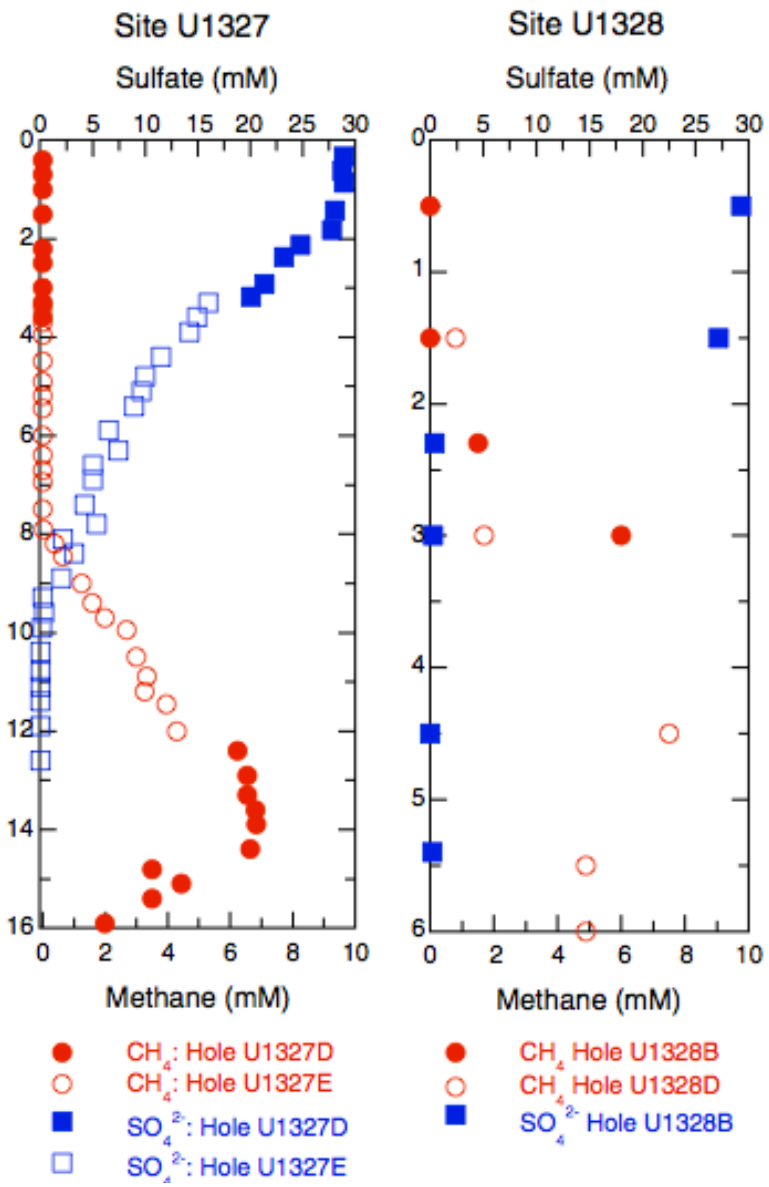

Figure 2.9 IODP site U1327 and U1328 sulfate-methane transition zone

These graphs show measured sulphate and methane concentrations in sediment for two drill holes from IODP Expedition 311. The sulfate methane transition zones for site U1327 is ~8 mbsf, and ~2 mbsf for site U1328 (Riedel et al., 2006).

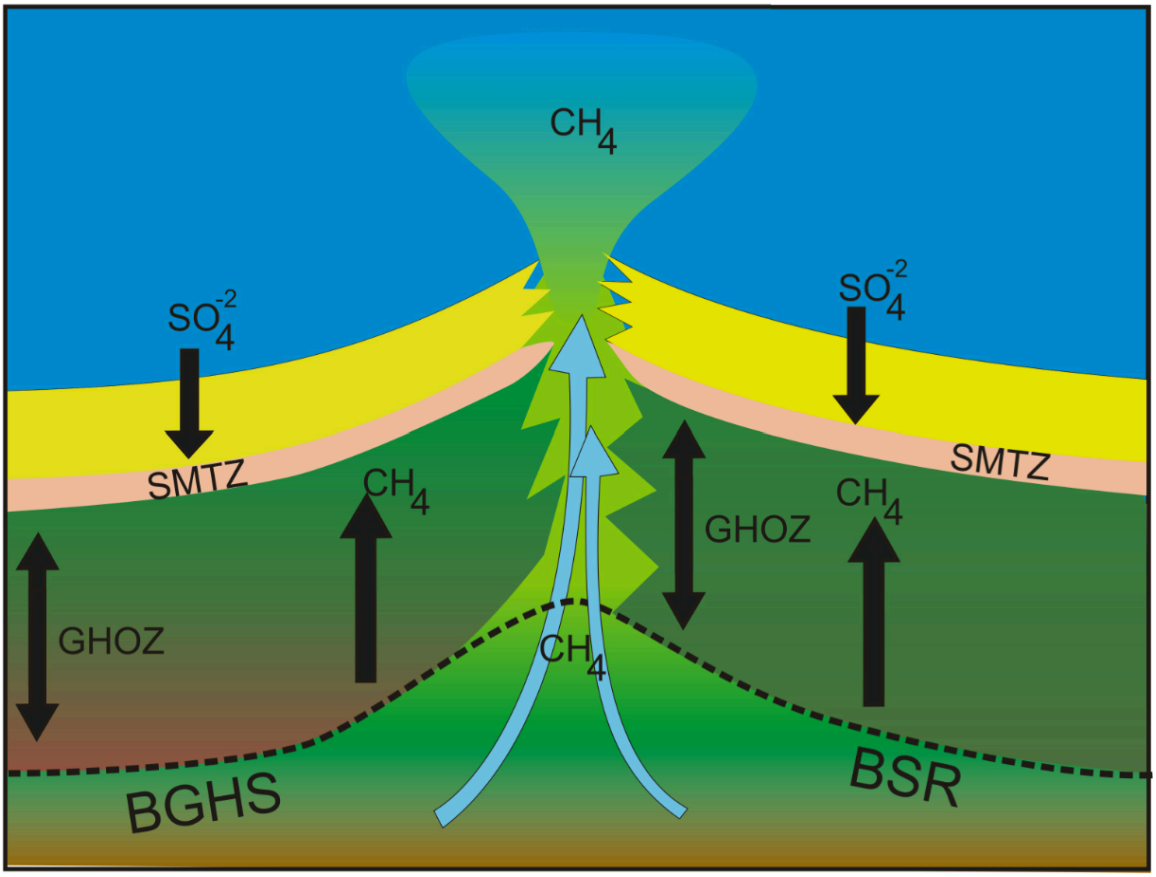

Figure 2.10 Sulfate-methane transition zone (SMTZ) illustration.

This illustration depicts the interaction between sulfate and methane with relative changes in fluid advection. Methane breaches the seafloor when advection rates are high and is anaerobically oxidized by sulfate when advection rates are low.

The concentration of methane in marine sediments varies due to a number of different factors (pore space, pore water salinity, available methane, etc.). Considering these parameters, analytical models have been created to describe and predict the formation of marine gas hydrate (e.g. Xu and Ruppel, 1999). The concentration of gas hydrate in marine sediments within the northern Cascadia can be 80-100% of pore space in local discrete environments (e.g. veins, lenses). These are zones of anomalously high fluid advection rates; the regional distribution among sediment is arguably much lower and averages <10% (Riedel et al., 2010).

The study area of this thesis is known to host some of the highest accumulations of gas hydrate associated with cold vents (Riedel et al., 2010). West of this study area at sites U1325-U1326 (15 and 7 km west of this study area respectively, and 10 km east of the deformation front) pore fluids have high chlorinity values due to ash-zeolite diagenesis and are less conducive to the formation of hydrate. Further from the deformation front (20-25 km) at site U1327-U1328 (this study area) fluid advection rates increase as discussed in Section 2.2. Deeper metamorphism (smectite-illite alteration) causes pore water freshening in advecting fluids further adding to hydrate stability. Landward at site U1329 fluid advection rates and pore water freshening decrease (Riedel et al., 2010). Previous Figure 2.6 shows alterations in advection rates and pore water salinity.

2.3.3 Bottom Simulating Reflector (BSR)

At the base of the GHSZ, temperatures are too high for the formation of hydrate. A thin layer of free gas typically denotes the base of the stability zone giving rise to the seismic expression of a BSR. Free gas is acoustically slow and generates a profound acoustic signature when imaged by seismic data. The presence of free gas at the base of the GHSZ (either through hydrate dissociation releasing methane, or methane sourced from below) marks a sharp change in compressional-wave (P-wave) velocity. This velocity inversion is amplified if the sediments above the base of the GHSZ are cemented with high-velocity hydrate. The sharp impedance contrast and subsequent polarity

inversion of the reflection are easily distinguishable on seismic recordings (Spence et al., 2010).

The occurrence of gas hydrate on the Cascadia was first hypothesized from the occurrence of a widespread BSR on seismic reflection data (Davis and Hyndman, 1989). BSRs are the foremost indicator of potential gas hydrate on continental margins. In seismic data, the BSR is visible as a single reflection within the sediment and often running parallel to the seafloor but with opposite polarity relative to the seafloor. The reflection marks a sharp impedance decrease of 20-30% (Hyndman and Spence, 1992, Spence et al., 1995). Concentrations of free gas just below at the BSR are low at ~1-2% (e.g. Hyndman, 1995; Yuan et al., 1996) Seismic reflectors above the BSR potentially marking the top of, or any part of, the GHOZ are rare. Reflectors below the BSR marking the cessation of free gas are also not observed and thus suggest that the transitions away from the base of the GHSZ are gradational.

Seismic line 89-08 (Figure 1.2) through the accretionary prism shows the widespread BSR throughout this study area. Figure 2.11 shows BSR depths for IODP Expedition 311 drill sites across the margin (Riedel et al., 2010). BSR depths are inferred from the concentration of dissolved methane and hydrate versus the concentration of dissolved methane and methane gas. The depth to the BSR varies though the study area as described by He et al. (2007) due to surface topography and variations in upward fluid flow.

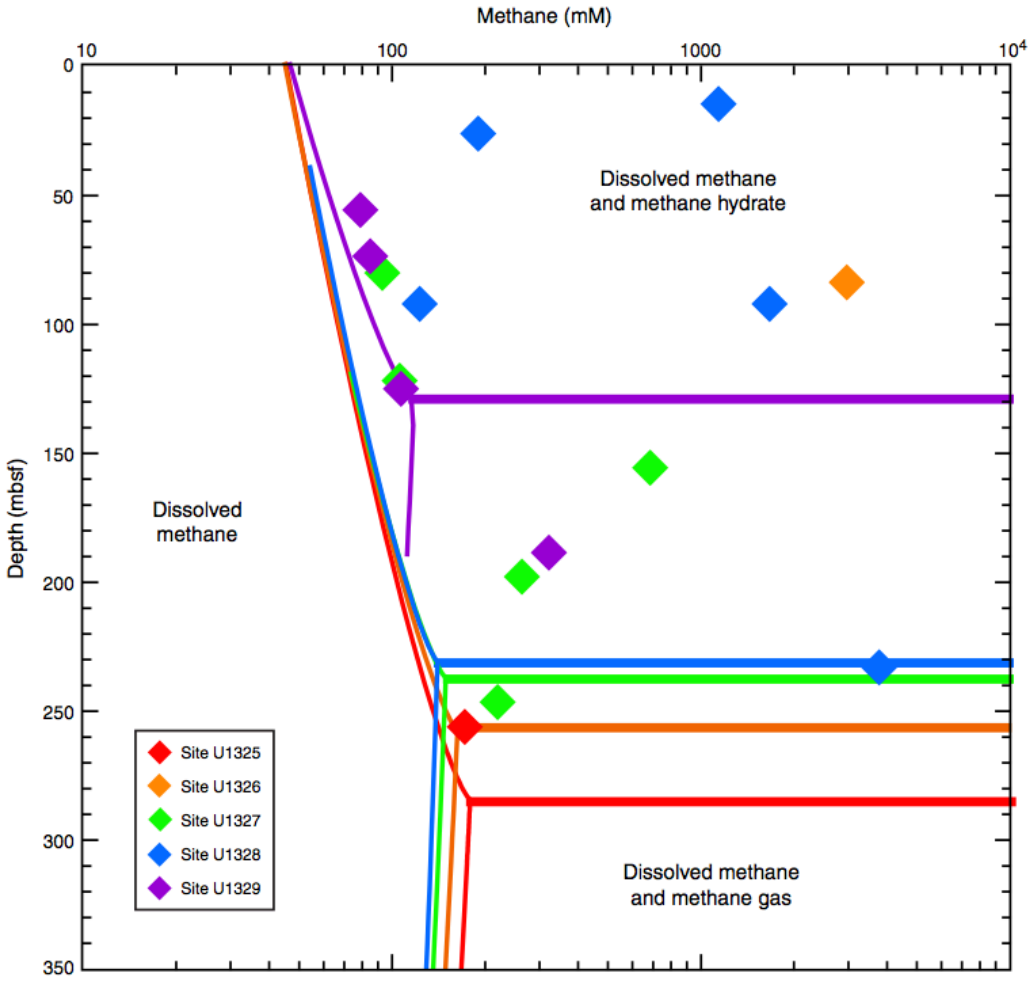

Figure 2.11 Methane concentrations for IODP sites and inferred BSR depths

This figure shows measured methane concentrations for IODP Expedition 311 drill sites and inferred BSR depth. Concentrations are measured through pressure core degassing (Riedel et al., 2010).

2.3.4 Hydrate Formation Mechanisms

The migration of methane from depth (below the BSR) into the GHOZ allows for the formation of hydrate. In this thesis, gas hydrate is considered to form in one of two ways: (1) through a natural decrease in pressure from the vertical migration of fluids, and (2) in localized areas that temporarily experience overpressure.

(1) As methane infused geo-fluids migrate towards the surface through fracture networks they experience a reduction in hydrostatic pressure. This reduction in pressure decreases the solubility of methane in pore fluids; if pressure is reduced enough methane will bubble out of solution. Free gas within the theoretical hydrate stability field is not stable and will incorporate itself into gas hydrate structure. The natural progression of fluids from BSR depths towards the surface potentially allows for the formation of hydrate to occur anywhere along the fluid's path. However, the formation of hydrate usually occurs in discrete hydrate layers. These discrete formations are caused in some capacity, if not entirely, due to the heterogeneity present within the sediment column (think stacked turbidite layers). Sand units offer higher permeability (more conducive for the formation of gas hydrate) while mud units are much less permeable. In shallow marine sediment (100 - 200 mbsf), porosity of mud and sand layers can vary significantly depending on sediment composition, grain sizes, sorting, and compaction history. Under these conditions it is not necessarily guaranteed that sand has higher porosity than mud (as e.g. detected during the Korean drilling in the Ulleung Basin, Ryu, 2012). These low permeable layers act as a barrier to vertical migration of fluids; if vertically migrating

fluids are unable to continue their progress towards the seafloor these areas may become over-pressured. Zones of over-pressure lead to the second setting for hydrate growth.

(2) In shallow marine environments where pressure generally does not exceed hydrostatic, pore pressure in excess of hydrostatic pressure are considered to be over-pressured. Over-pressuring pore fluids have the opposite affect on methane solubility and acts to increase the local solubility of methane. If the source of fluid over-pressure (e.g. fluid backing) to these zones is removed, and the pore pressure returns to hydrostatic, the solubility of methane will decrease locally causing methane to bubble out of solution. In this situation, the fluids have remained stationary yet have experienced pressure changes analogous to vertical migration.

In the first scenario for hydrate formation above, where migrating fluids progress uninterrupted towards the surface, this is considered a hydrocarbon "seep". The formation of hydrate along vertical fractures is commonly encountered at cold vent sites (e.g. Hydrate Ridge). In the second scenario where the migration of fluids is interrupted by an impermeable barrier, this situation is called a hydrocarbon "trap". These areas may thus host concentrations of hydrate significantly above the average for the region. Subsurface methane traps and sites of methane seepage are discussed in Chapter 5 for this study area.

2.3.5 Hydrate Pull-up Structures

Typically, P-wave velocity analysis is employed to infer the presence of hydrate from seismic data. The presence of hydrate disseminated through pore spaces or cementing sediments can create measureable increases in P-wave velocity (e.g. Chand et

al., 2004). There have been numerous studies estimating the concentration of gas hydrate using P-wave velocity models on the northern Cascadia margin (e.g. Yuan et al., 1996; 1999; Hobro et al., 2005; Chen, 2006; Dash and Spence, 2011).

If a gas hydrate trap is present in the subsurface, hydrate-bound sediment will have a higher P-wave velocity than the surrounding sediment. An increase in sediment velocity relative to the surrounding sediment will result in higher acoustic impedance for the hydrate-bearing layer, and a higher reflection coefficient between the hydrate unit and the surrounding layers. This high impedance reflector can create two measureable affects in the seismic data: First, a high reflection coefficient will result in a brightening of the sub-surface reflector at the top of the hydrate occurrence. Second, where hydrate is present in high concentrations there may be a local increase in sediment P-wave velocity. As the travel time for a P-wave in hydrate is faster than the surrounding sediment, a "pull up" structure may form underneath. A pull up structure forms when the travel time for a seismic wave between the source and receiver, and a given sedimentary horizon is faster in one region relative to the adjacent. In this environment the higher velocity medium is the discrete hydrate package, and the localized increase in travel time acts to bow reflections vertically. Similar occurrences have been documented in the Ulleung Basin where the differences in velocity were used to determine hydrate concentration at vent chimneys (e.g. Stoian et al., 2008). Pull up structures in this data set will be discussed in Section 5.5.

2.3.6 Carbonate Structures

Authigenic carbonates are commonly present at cold vent sites and are an indicator of prolonged fluid expulsion (Carson et al., 1991; Paull et al., 1992). Authigenic carbonate is often the first method of detection for seafloor cold vents systems as carbonates exposed on the seafloor are easily detected with ship-mounted sonar due to their hardness relative to the surrounding softer sediments. These carbonates precipitate from the fluids due to the anaerobic oxidation of methane (AOM) and other heavier hydrocarbons (Orange et al., 2002). The AOM occurs at the SMTZ where downward-diffusing seawater sulfate is reduced upon encountering upward-migrating methane. Equation 2 (below) shows the anaerobic oxidation of methane (sulfate reduction) generating bicarbonate, bisulfide, and water.

Equation 2: $SO_4^{2-} + CH_4 \leftrightarrow HCO_3^- + HS^- + H_2O$

Bicarbonate (HCO_3^-) is also produced through organoclastic sulfate reduction (Malinverno and Pohlman, 2011) in the area above the SMTZ known as the sulfate reduction zone (Figure 2.10). The prevailing theory of formation is that the upward migration of methane shortens diagenetic profiles (i.e. the SMTZ moves upwards in the sediment column) such that carbonate is able to precipitate at or near the seafloor (Martin et al., 1997). Equation 2 shows the reaction of bicarbonate with calcium to form carbon dioxide, carbonate, and water. Both high and low magnesium carbonates, as well as aragonite, are the most common precipitants from the AOM (Luff & Wallmann, 2003).

Equation 3: $Ca^{2+} + 2HCO_3^- \leftrightarrow CO_2 + CaCO_3(s) + H_2O$

Unlike other indicators of cold vents (e.g. biological communities, gas hydrate), authigenic carbonate's presence remains after cessation of fluid venting (assuming sedimentation rates are low and the carbonates are not buried) and can therefore be used as an indicator of paleo-venting sites. Authigenic carbonate and hydrate often co-exist due to their dependence on sources of methane. Fluid advection is simultaneously a mechanism of heat advection, and thus may act to destabilize hydrate existing within the stability zone (Suess et al., 1999). Seafloor authigenic carbonates can become quite massive compared to the regionally smooth seafloor (heights greater than 5 m). Determining the rates of authigenic carbonate nucleation and examining the relationship between carbonate deposition and chemosynthetic communities are areas of active research (e.g. Luff et al., 2004; Ussler and Paull, 2008).

2.3.7 Chemosynthetic Biological Communities

The seepage of methane-rich fluids to the surface often supports unique ecosystems of marine biota (Kulm et al., 1986; Torres et al., 2009). Bacterial mats, chemosynthetic clams, and tubeworms often cover sites of venting. These communities can be extensive and cover square kilometers of the seafloor. Venting sites with abundant CBC's are often coincident with the presence of authigenic carbonate (Lewis and Cochrane, 1990). These communities are known as "cold seep communities" and exist

through the microbial utilization of the chemicals present in venting fluids. Increased advection of methane plus other hydrocarbon-bearing fluids and sequential hydrogen sulfide (product of anaerobic oxidation of methane) feed chemosynthetic communities. The distribution of benthic communities near and at cold vent sites is primarily related to the sulfide flux from the seafloor (Sashling et al., 2002). The deliverance of sulfide to the seafloor is inherently linked to the regional methane advection profile. The highest rates of AOM occur in the very near- surface sediments (10-15 cm) oxidizing methane that would otherwise escape into the water column.

Organisms encountered at cold vent sites are primary producers, and survive through either the consumption of methane, or the oxidation of sulphide. At study by Boetius and Suess (2004) examined biodiversity in CBCs encountered at Hydrate Ridge on the Southern Cascadia margin. Methane-consuming microbial communities are the predominant sink for methane emission through methanogensis. Methanotropic archea ANME-2 are identified as the main contributor to AOM. AOM products bicarbonate and bisulfide increase seawater alkalinity and promote the formation of authigenic carbonate. Authigenic carbonate is the final product and permanent carbon sink for organic carbon. Bisulfide then acts as sustenance for sulfide-reducing benthic organisms. Sulfide-reducing bacterial mats (*Beggiatoa*) are common in areas receiving high methane advection rates with shallow sulfate profiles. In zones of intermediate advection rates, the seafloor is commonly occupied by clam fields (*Calyptogena*) and tubeworms. Where fluid flow rates are low, the zone of maximum AOM is deeper, and *Acharax* clams have specifically adapted to tunnel for deeper-residing sulfide (Sahling et al., 2002). Figure 2.12 shows an illustration of various seafloor biota encountered during ODP Leg 204 at

Southern Hydrate Ridge. Methane degassing from seafloor sediments decreases from left to right through the figure. Progressing left to right through the figure, Bacterial mats (*Beggiatoa*) are first seen at sites of active venting, followed by claim communities (*Calyptogena*), and eventually subsurface burrowing clams (*Acharax*). In general, where multiple organisms maintain the same location, a symbiotic relationship is developed with morphological and physiological adaptations providing their symbionts with nutrients (e.g. sulfide, oxygen).

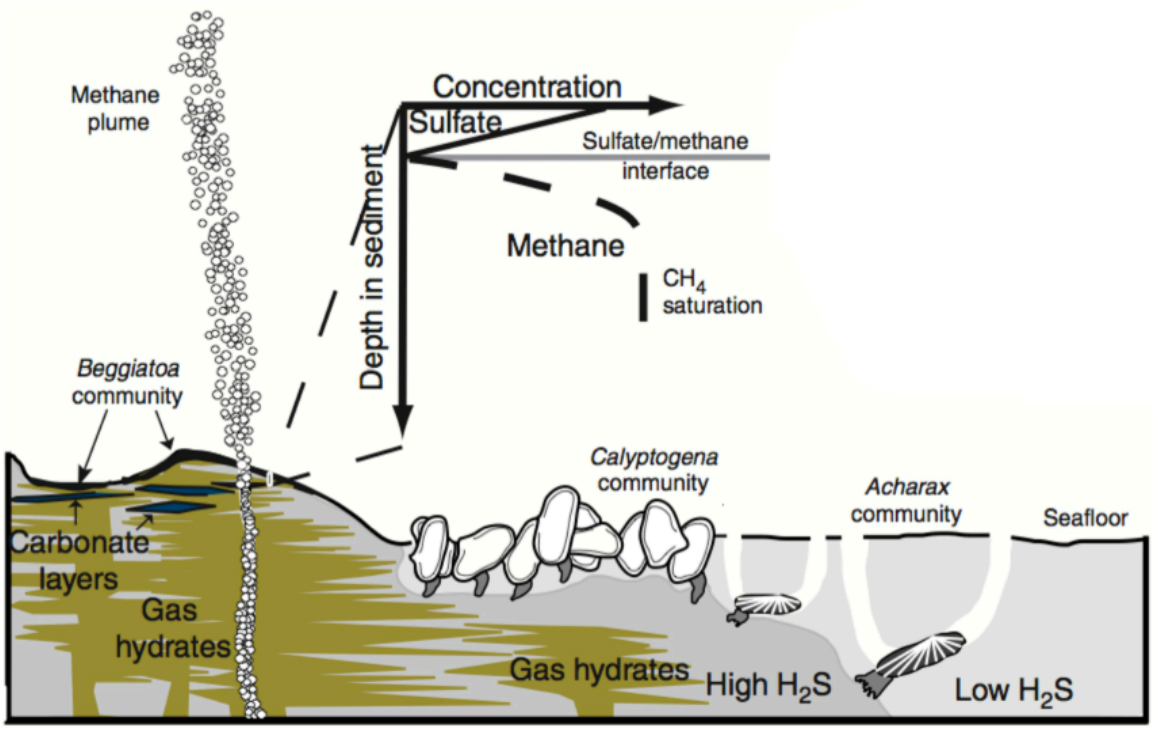

Figure 2.12 Methane degassing affects on seafloor biota concentration

This illustration shows the distribution of bacterial mats (*Beggiatoa*) at sites of active venting, clam communities (*Calyptogena*) at intermediate sites of venting, and eventually subsurface burrowing clams (*Acharax*) at more distal venting locations. Figure adapted from IODP Expedition 204 Preliminary Report.

3 AUV Data – Methods

In this chapter I examine AUV and ROV data collected during the 2009 cruises carried out jointly by between MBARI and the Canadian government. The construction, functionality, and method of deployment for MBARI's AUV module are introduced. The functions of the AUV's sonars are analyzed, brief processing methodologies are outlined, and the strengths and weaknesses of the different data types are summarized.

3.1 AUV Module

The AUV "D Allan B" by MBARI is 0.53m in diameter and 5.3m long. Its shell is made of plastic so it is acoustically transparent to the frequencies it records. It weighs 680 kg (in air) and can travel at 5.4 km/h (usually maintaining a speed of 3 knots) through its electric propulsion engine (Figure 1.4). The AUV can dive to a maximum depth of 6 km and travel on missions of up to 18 hours in duration. The submersible is fitted with onboard navigation and mapping sonars that operate simultaneously. These sonars include: (1) a Reson 200 kHz multi-beam sonar for collecting bathymetry information to generate seafloor relief maps (50 cm resolution), (2) Edgetech 110 and 410 kHz side-scan sonars (one on each side) that measure small changes in seafloor structure and more importantly characterize seafloor hardness (~10 cm resolution), (3) a 3.5 kHz sub bottom profiler for imaging structures beneath the seafloor allowing for resolution of thin sedimentary layers and other small-scale structures (~40-50 m

penetration and up to 10 cm vertical resolution). Traditionally, the side-scan sonar is not recorded as the AUV operates 50 m above the seafloor, which is too high for optimal recording. More detail on MBARI's AUV mapping sonars can be found on their website (http://www.mbari.org/auv/MappingAUV/sonars.htm).

3.2 Data Acquisition and Processing

The AUV was deployed over the Cascadia margin seafloor for three days. Each day the AUV surveyed a different geographic area (Figure 3.1). The AUV swath pattern tracks with a "lawn mower" pattern with 150 m spacing between each track. Data processing is carried out by MBARI's science team using the open source software called "MB-System". After a successful dive, processing involves correcting for pitch and roll errors during the dive, noise filtering, and navigational reconstruction for path deviation. Bathymetry resolution is depends on how close the sonar source and receivers are to the seafloor; MBARI's D. Allan B usually flies at 50 meters above seafloor, allowing ~1 m grid resolution.

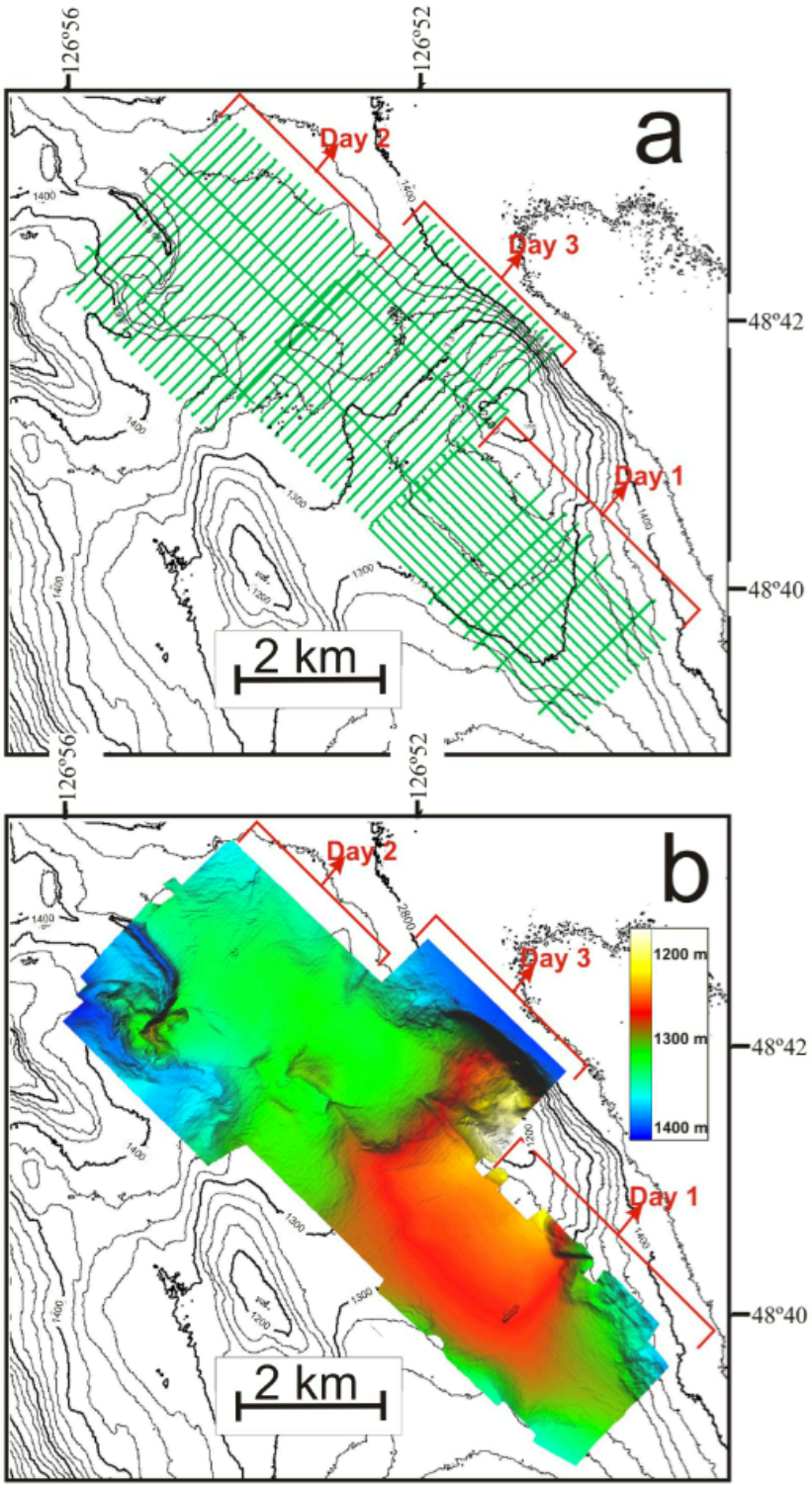

Figure 3.1 AUV track lines and high-resolution bathymetry

(a) AUV track lines, a total of 68 lines (inlines plus crosslines) were surveyed over 3 days. (b) AUV high-resolution bathymetry

3.2.1 Bathymetry

Bathymetry was recorded by a Reson 200 kHz Multibeam sonar with a 150-degree swath. Of the 68 lines surveyed, 12 were cross-lines (90° to main track lines). These cross-lines allow the depth data to be normalized to account for height discrepancies throughout the survey. These cross-lines also calibrate relative backscatter to account for influences related to surveying direction on the backscatter values which arise from large topographic variations (as explained later). The sonar has a lateral resolution of 1 m, and is capable of producing 11 cm vertical resolution. Bathymetry grids shown in this thesis are gridded at 2 m resolution. Gridding at 1 m resolutions or higher produces significant noise that needs to be smoothed out for a coherent image, a time intensive process not necessary for the scale of many features represented and discussed in this thesis (e.g. carbonate mounds and regional changes in seabed morphology). Pockmarks in this study area often have a vertical relief of less than 2 m; these features can still be resolved yet higher resolution gridding may bring more clarity. The AUV high-resolution bathymetry is shown in Figure 3.2. Specific sites of interest discussed in this thesis are identified in Figure 3.2; these sites will be described in detail within Chapters 4 and 5.

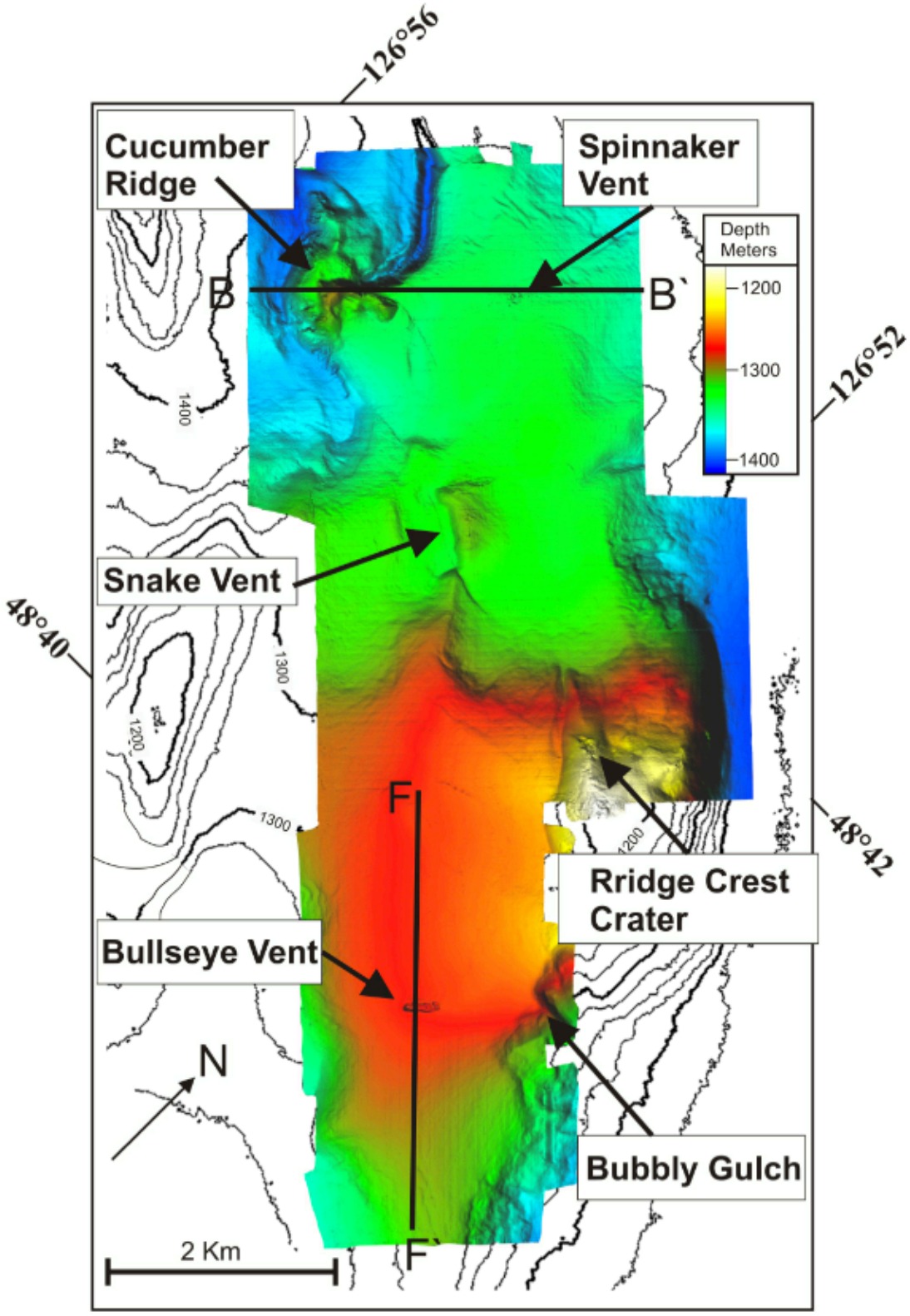

Figure 3.2 High-resolution bathymetry

Figure 3.2 (previous page) High-resolution bathymetry: Bathymetry of the study area with arrows showing key sites of investigation with their informal names. Profile line B-B´ is AUV line 20090724_0031 and is used for topographic controls on the AUV recordings (Section 3.2.4). Spectral analysis is applied to data from line F-F´, which is AUV line 20090723_0027 (Section 3.2.4).

3.2.2 Non Side-scan Chirp Sonar Reflectivity

Two chirp sonars exist on the AUV: a "regular" chirp sonar and side-scan sonar. The regular chirp sonar measures the height of the AUV off the seafloor. It does this by measuring the time between the initial chirp signal emitted and its arrival back at the AUV. The arrival time of the signal gives the depth, and the strength of the arrival (amplitude) provides information on seafloor hardness (discussed in greater detail in Chapters 4 and 5). A problem associated with this measurement of "hardness" is how proximal topography affects the energy response. Where topography is sloping, energy is lost due to the reflective beam being oblique to the angle of incidence. To create an accurate amplitude measurement the arrivals have to be scaled appropriately for surface topography. This correction was provided by MBARI, using the high-resolution bathymetry and calculating response angles for the given AUV position. Figure 3.3 shows the amplitudes corrected for regional topography over the northern grid (day 2, Figure 3.1).

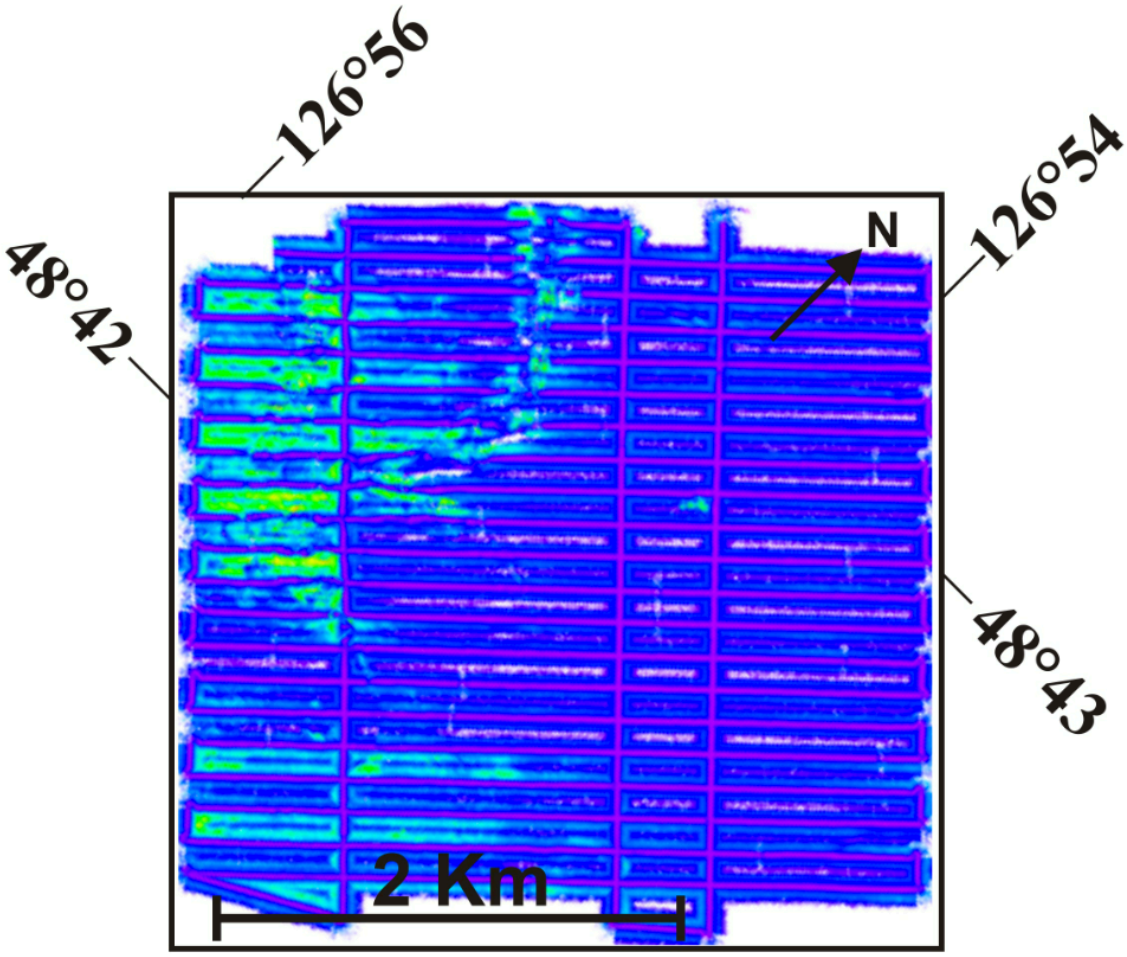

Figure 3.3 Vertical incidence sonar corrected for topography

Amplitude of vertical incidence chirp sonar reflections adjusted for seafloor topography. The northern most grid (surveyed day 2, Figure 1.1). Correcting the data for changes in bathymetry does not illuminate any lateral changes in seafloor reflectivity. As lateral changes in reflectivity are known to exist from the presence of carbonates (see Chapters 4, and 5), the limited variation in this reflectivity for this data set does not warrant further investigation. A color scale is not available, however lighter values (greens) are high and darker values (blues) are low.

The seafloor amplitude response (backscatter) is a useful method for inferring seafloor geology quantitatively. Correcting the data for changes in seafloor slope and giving preference to the 0° response (directly below the AUV) can illuminate seafloor geology. Unfortunately variations in reflective strength are sparse and show little

dynamic range where significant variations would be expected. The problem has been diagnosed to occur from the sensitivity of the unit that was quoted "to have been set to high" during the expedition (personal communication with C. K. Paull and D. Caress, 2012). Due to the sparseness of this type of data, and lack of data quality, little reflective information (quantitative or otherwise) is extractable and thus not pursued further.

3.2.3 Side-scan Sonar Reflectivity

The Edgetech 110 and 410 kHz chirp side-scan sonar measures the seafloor structures through an acoustic fan beam projected orthogonal to the AUV. Like the chirp sonar (non side-scan) described above, reflective strength is also affected by changes in seafloor elevation. Hills perpendicular to the AUV's flight path will generate relative highs, while valleys will create relative lows; therefore side-scan data are also corrected for seafloor bathymetry. Side-scan data have additional processing complexities; because swath paths overlap, measurements at the edge of paths often conflict. For this reason, measurements that overlap often create conflicting responses. To sidestep this problem, backscatter values are all displayed looking in the same direction, effectively showing only half of all recordings. The result is a "shingling" of the results with an azimuthal preference. Figure 3.4 (left) shows an illustration of how the AUV track direction and swath overlap. Figure 3.4 (right) shows how this overlap is handled in the processing with each lap gaining an azimuthal preference. Like the bathymetry, the reflective data were collected during three separate dives over three days. Data from the three days of

surveys were spliced together (Figure 3.5) where bright colors are backscatter highs (green to red) and dark colors are backscatter lows (blue to black).

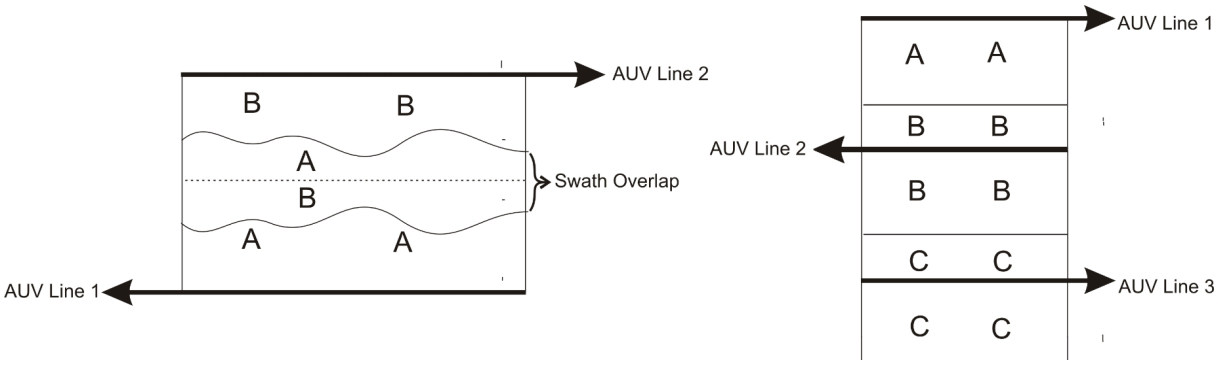

Figure 3.4 Sidescan backscatter "shingling" method

During the deployment (left) the AUV records reflective information twice through the same area. The area of overlap AB will have conflicting reflective values unless the surface was flat and the AUV maintained the same height. Giving an azimuthal preference (right) to the AUV recordings results in a "shingling" of the AUV recordings.

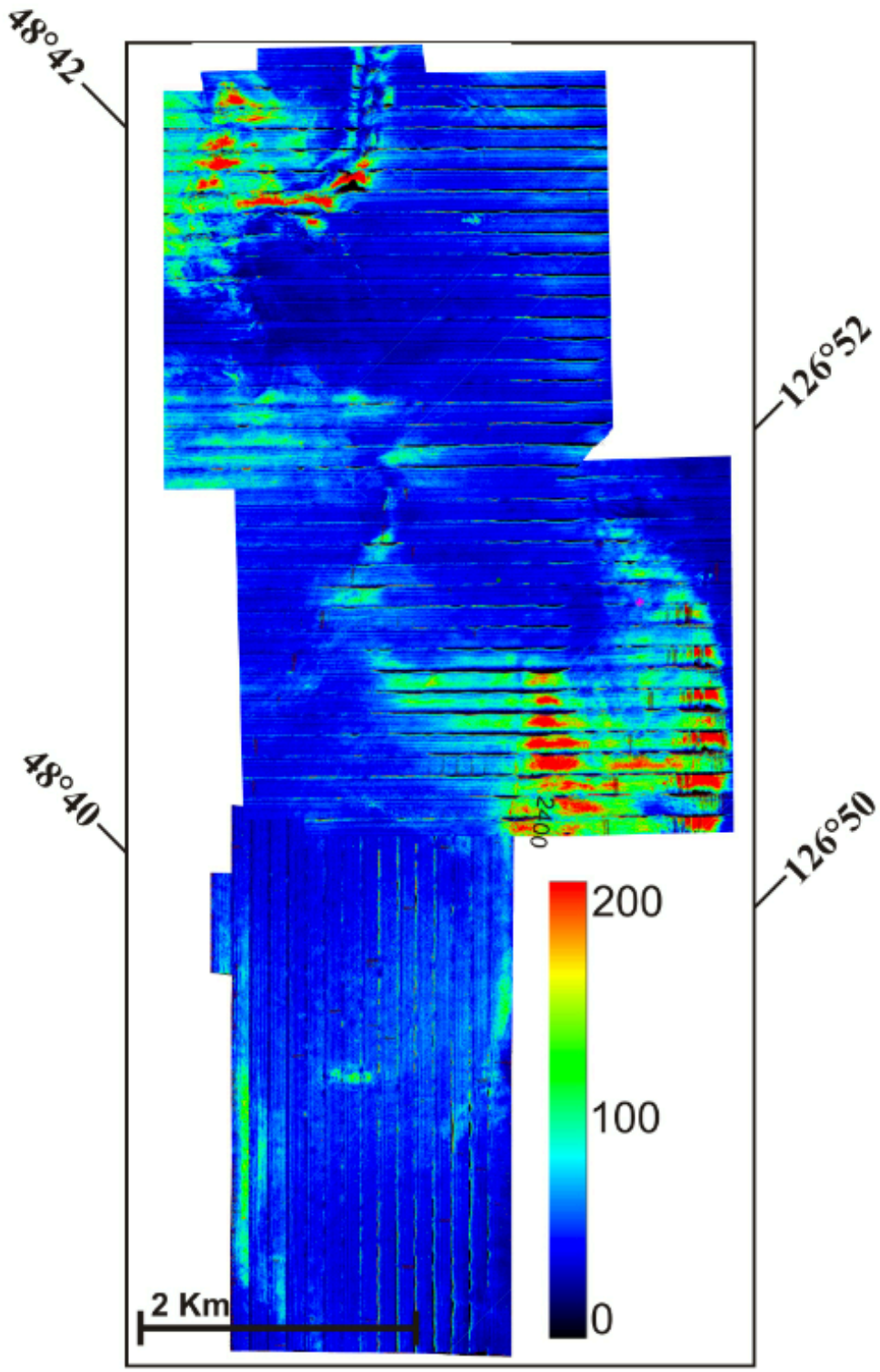

Figure 3.5 Combined side-scan sonar backscatter (grids 1-3)

Backscatter measurements over survey area pieced together from 3 different days (reds are highs, greens intermediate, and blues to blacks are lows).

3.2.4 Sub-Bottom Profiler

The 2-16 kHz sub-bottom profiler operates as a seismic source and receiver. Like traditional seismic, it measures the impedance contrasts within the subsurface and thus provides details associated with lithology and bedding. Unlike traditional lower frequency seismic data, the penetration depth of the AUV is less than 10% that of streamer towed seismic, due to the AUV's low energy and high frequency signal (Figure 1.6).

The AUV uses the regional bathymetry through the area to create a rough tracking elevation. During the survey, when the vehicle encounters topography changes unresolved by the regional bathymetry it adjusts itself to maintain its preferred height. Due to the AUV maintaining the same height above the seafloor, the uncorrected result would make the seafloor appear relatively flat. Adjusting the response times to accommodate for changes in the AUV elevations above the seafloor reveals the seafloor bathymetry, and better resolves the subsurface structures. Figure 3.6 shows AUV sub-bottom profiler data for line 20090724_0031 (location in Figure 3.2) before adjusting for AUV height and the time-shifted AUV results. The shifted AUV line shows increases in topography especially apparent between shot points 500 and 1500, at the topographic feature known as Cucumber Ridge.

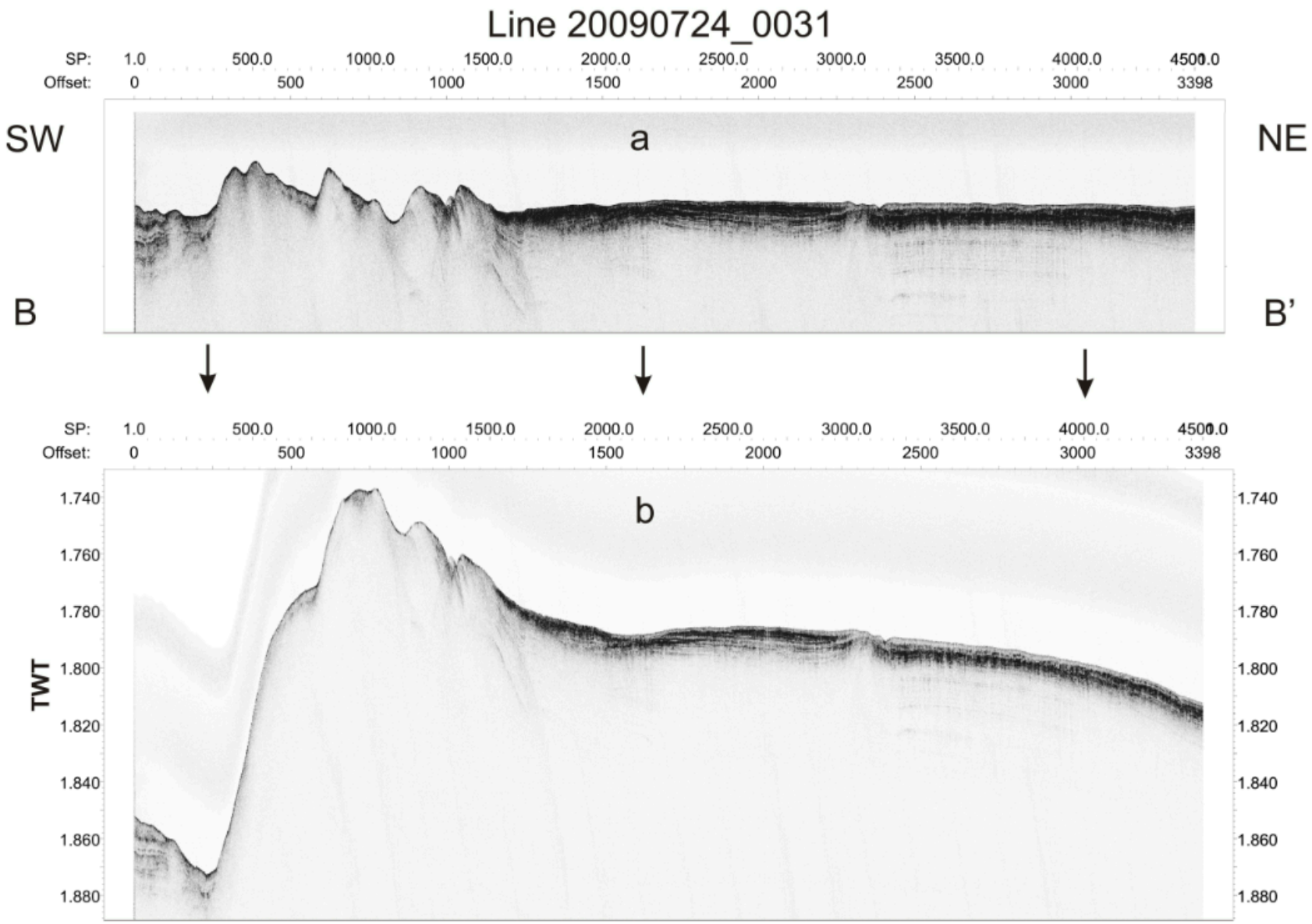

Figure 3.6 Sub-bottom profiler time adjustment

Figure 3.6 (previous page) Sub-bottom profiler time adjustment: Line 20090724_0031 before and after compensation for AUV elevation. The upper seismic image (a) shows AUV recordings as it tries to maintains a height of ~50 m above the seafloor, in an area where the seafloor elevation changes rapidly. Seismic image (b) shows the corrected sub-bottom profiler seismic section adjusted for the change in AUV flight height. The shifted AUV line shows increases in topography especially apparent between shot points 500 and 1500, at the topographic feature known as Cucumber Ridge.

Limited seismic penetration compared to streamer-towed seismic is (predominantly) due to the strength and frequency of the signal. The high frequency of the sub bottom profiler makes it more susceptible to the effects of acoustic attenuation compared to lower frequency seismic data. This vulnerability to attenuation occurs because acoustic waves oscillating at higher frequencies (shorter wavelengths) attenuate faster than lower frequency waves (longer wavelengths). The result is an apparent increase in bed thickness with depth (Figure 3.7a) due to the faster attenuation of shorter wavelength, higher frequency signal. To record the thickness of a sedimentary bed accurately, the wavelength has to be ¼ of the bed thickness. AUV line 20090723_0027 in Figure 3.7 (profile F-F′, Figure 3.2) has excellent seismic penetration and shows increasing bed thickness with depth. To detect losses in the spectral content, a spectral analysis was carried out on line 20090723_0027 in which the frequency of near-surface reflections was compared to that of deeper reflections over shot points 400-4300. Figure 3.7 (c) and (d) show the computed spectral content between times 1.705-1.720 s and 1.724-1.740 s respectively. Unfortunately, only envelope data were provided by MBARI, not raw amplitudes. Envelope data have lost the original phase content as part of the

processing workflow already embedded within the AUV system. Figure 3.7 (c) and (d) show little change in frequency content over the computed time intervals. Figure 3.7 (e) shows a seismic wiggle trace for shot point 4200, the shot shows positive amplitude values only and much of the high frequency content is lost.

Figure 3.7 (following page): Spectral analysis for frequency content. AUV line 20090723_0027 shows increasing bed thickness with depth, and a closeup between shot points 400-4300. The locations of the spectral windows are shown in (b) with the upper window between 1.705 and 1.720 seconds (c), and the lower window between 1.724 and 1.740 seconds (d). The computed spectral content is shown in the corresponding (c) and (d) graphs. The vertical axis of both (c) and (d) show 10% total energy remaining (y-axis) and a frequency range between 0 and 3500 Hz. Little variation is seen in the spectral content due to the data having lost its frequency content during processing. The remaining "envelope" data can been seen at shot point 4200 where polarity inversions are not visible, confirming the loss of oscillatory information.

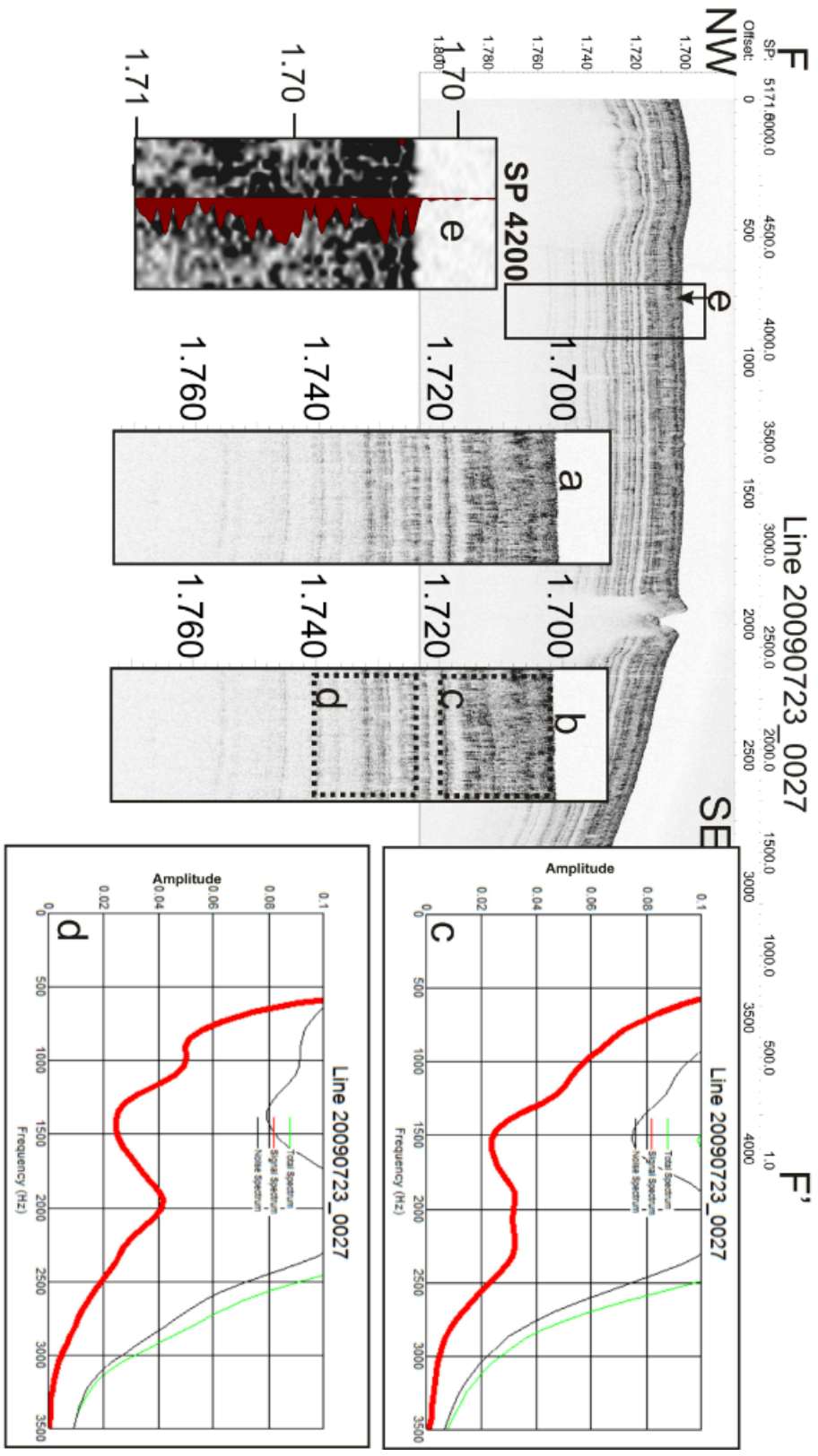

Figure 3.7 Spectral Analysis Of Profiler Data

4 ROV and AUV Observations

This chapter presents ROV observations and AUV data for the study area. ROV observations include seafloor images of cold-vent sites, sonar recordings of gas plumes, and a seafloor push core R1554 with description and physical property analysis. AUV observations are presented initially with bathymetry and backscatter maps of the survey area. Individual sites of interest are then described in detail with sub-bottom profile data and locally enhanced bathymetry and backscatter maps.

4.1 Robotic Underwater Vehicle (ROV) Visual Observations

During the 2009 joint MBARI and NRCan cruise, photographic images were taken at specific waypoints during ROV dives. This section will investigate individual dive locations in the study and describe sea floor cold-vent related activity. Figure 4.1 shows the regional bathymetry in the area with the location of dive sites identified by yellow boxes labeled a, b, c, and d.

4.1.1 ROV Seafloor Waypoints and Images

Zoomed survey grids with specific ROV waypoints are shown for Spinnaker Vent (Figure 4.2), Ridge Crest Crater (Figure 4.3), Bullseye Vent (Figure 4.4), and Bubbly Gulch (Figure 4.5). The color scale (depth) of the regional bathymetry is the same for all figures except Bullseye Vent. At Bullseye Vent the color scale was changed to enhance

topography, so a separate color bar is included for the figure. Figures 4.2-4.5 indicate specific waypoints on the seafloor as numbers; the numbers on these waypoints correspond to the following images in Figure 4.6-4.9. The ROV images at these sites are referenced in Chapter 4 to supplement the AUV data for analysis of the specific zones of interest.

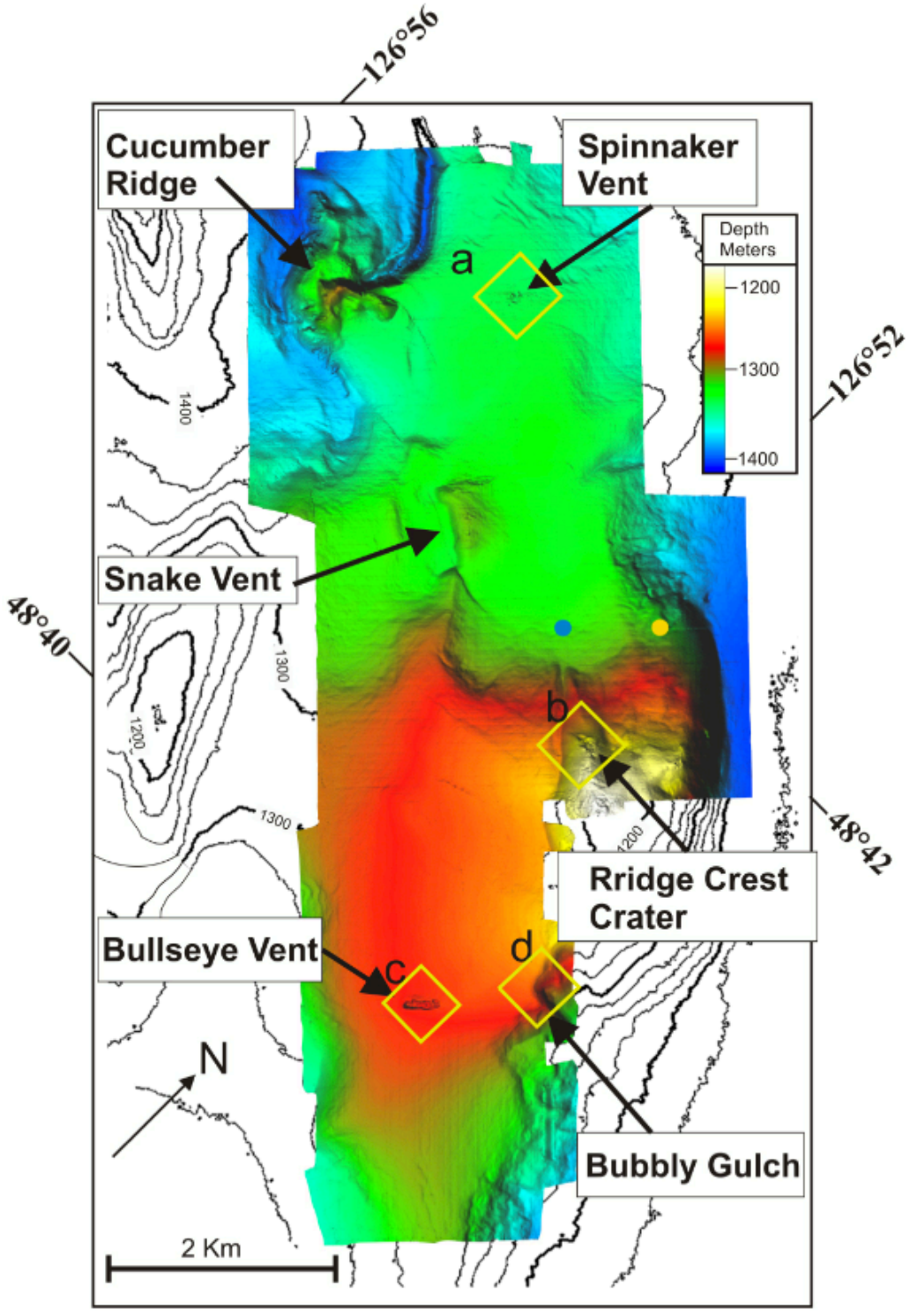

Figure 4.1 High-resolution bathymetry outlining ROV dive and core locations

Yellow boxes a-d show the general locations for seafloor images recorded from the ROV dive. Core R1554 location is shown by the yellow dot, and ODP site 889 is shown by the blue dot.

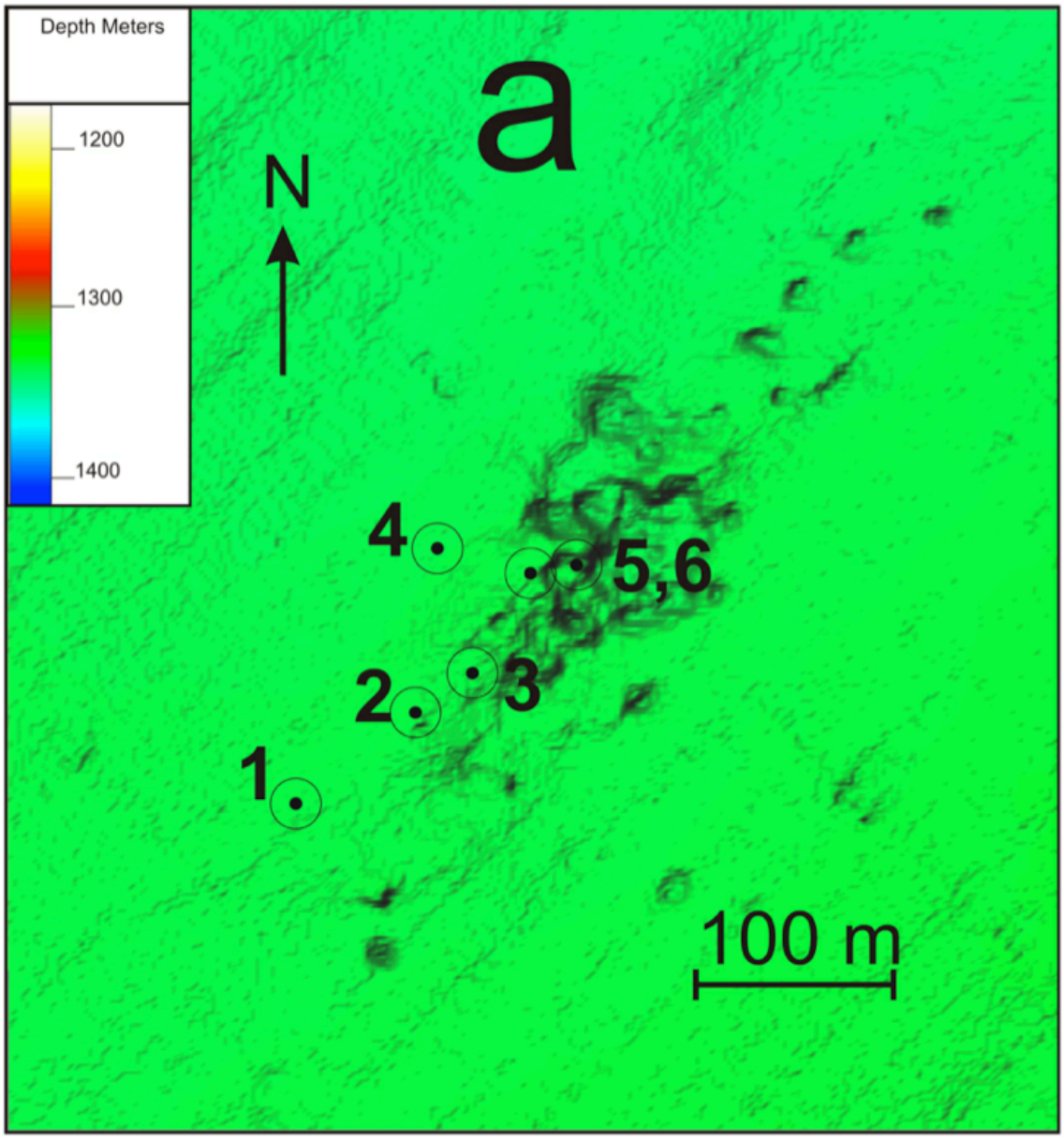

Figure 4.2 Spinnaker Vent ROV dive waypoints

Zoomed grid of Spinnaker Vent; seafloor observations for waypoints 1-6 are seen in Figure 4.6.

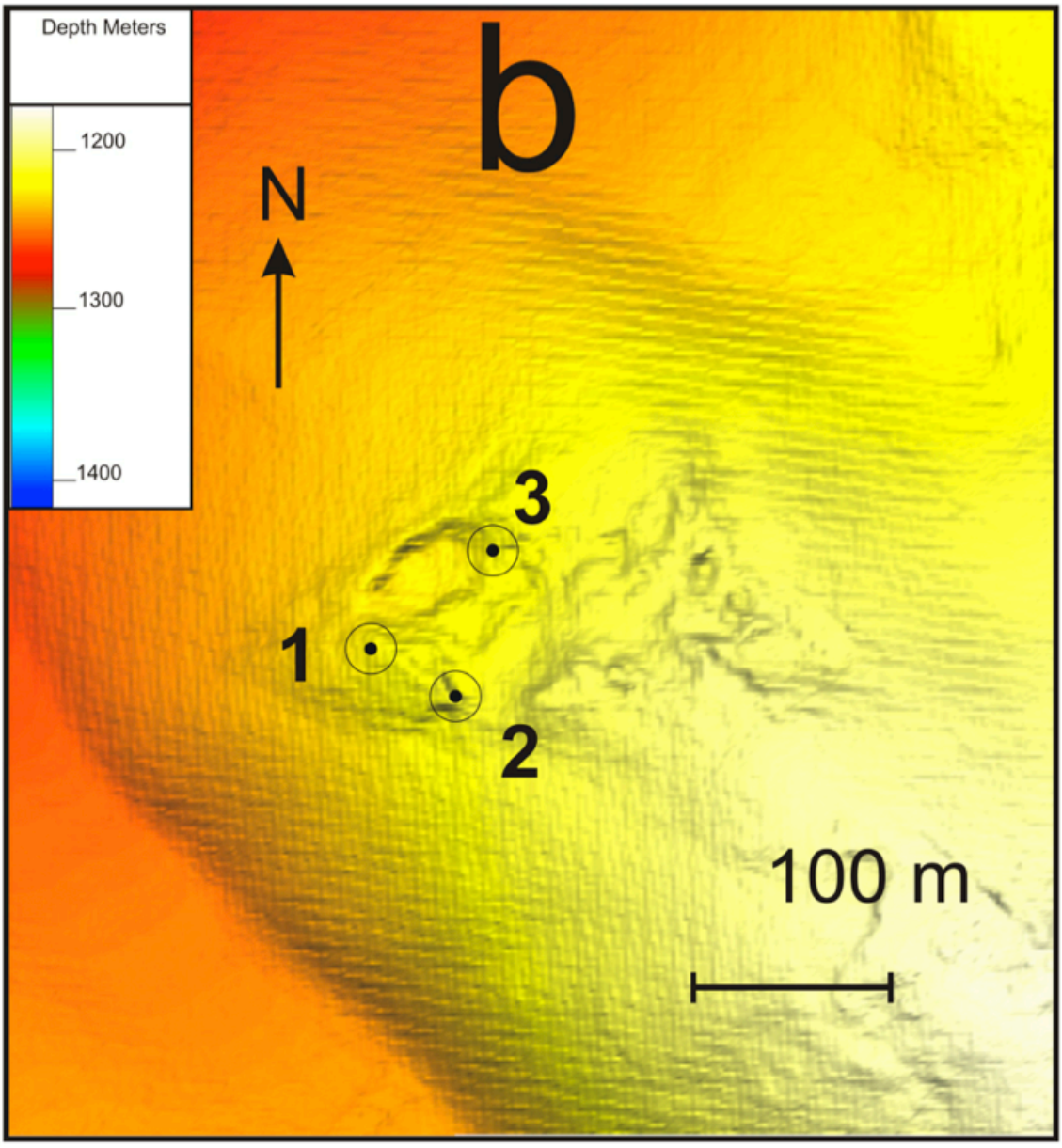

Figure 4.3 Ridge Crest Crater ROV dive waypoints

Zoomed grid of Ridge Crest Crater; seafloor observations for waypoints 1-3 are seen in Figure 4.7.

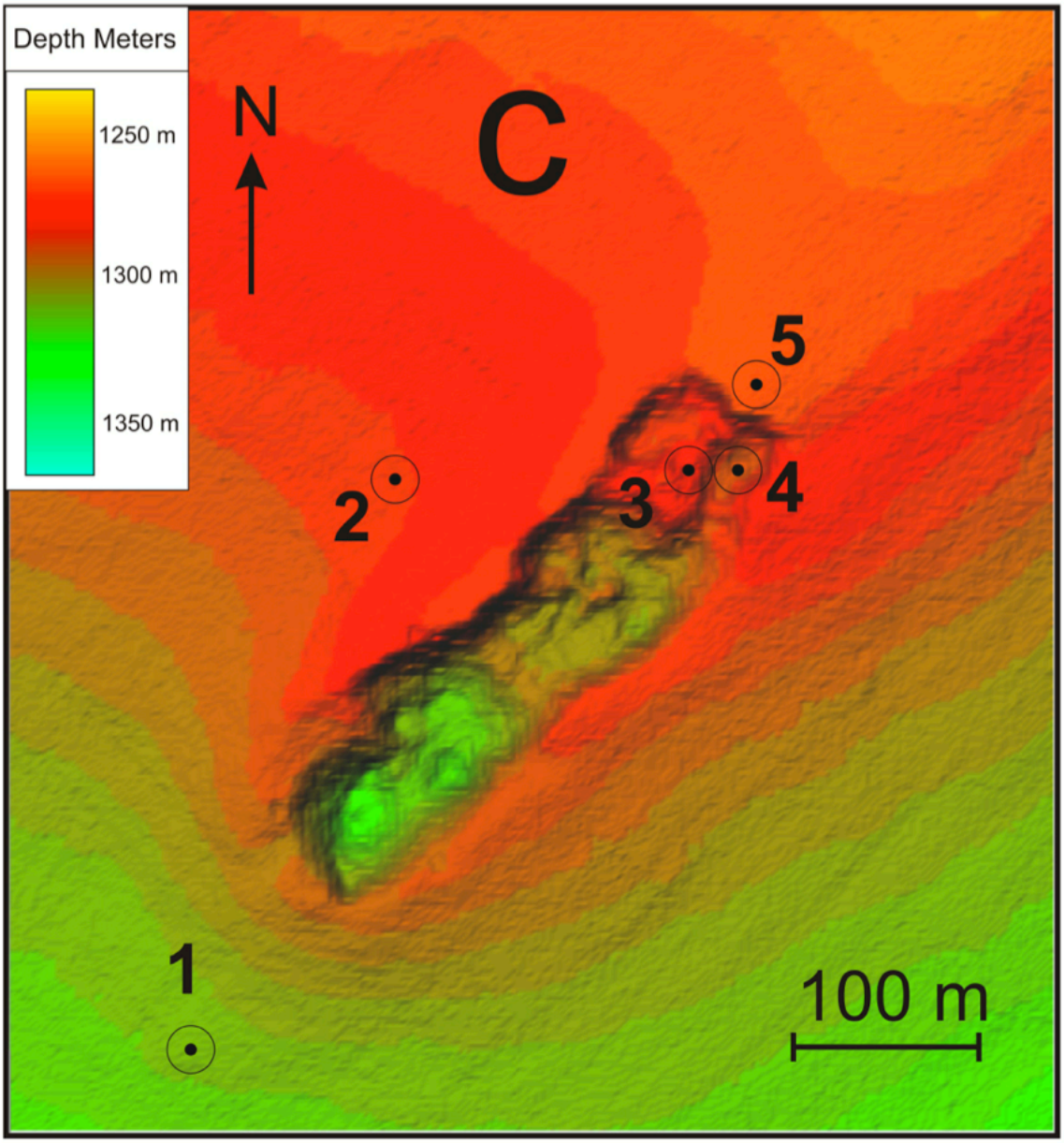

Figure 4.4 Bullseye Vent ROV dive waypoints

Zoomed grid of Bullseye Vent, seafloor observations for waypoints 1-5 are seen in Figure 4.8.

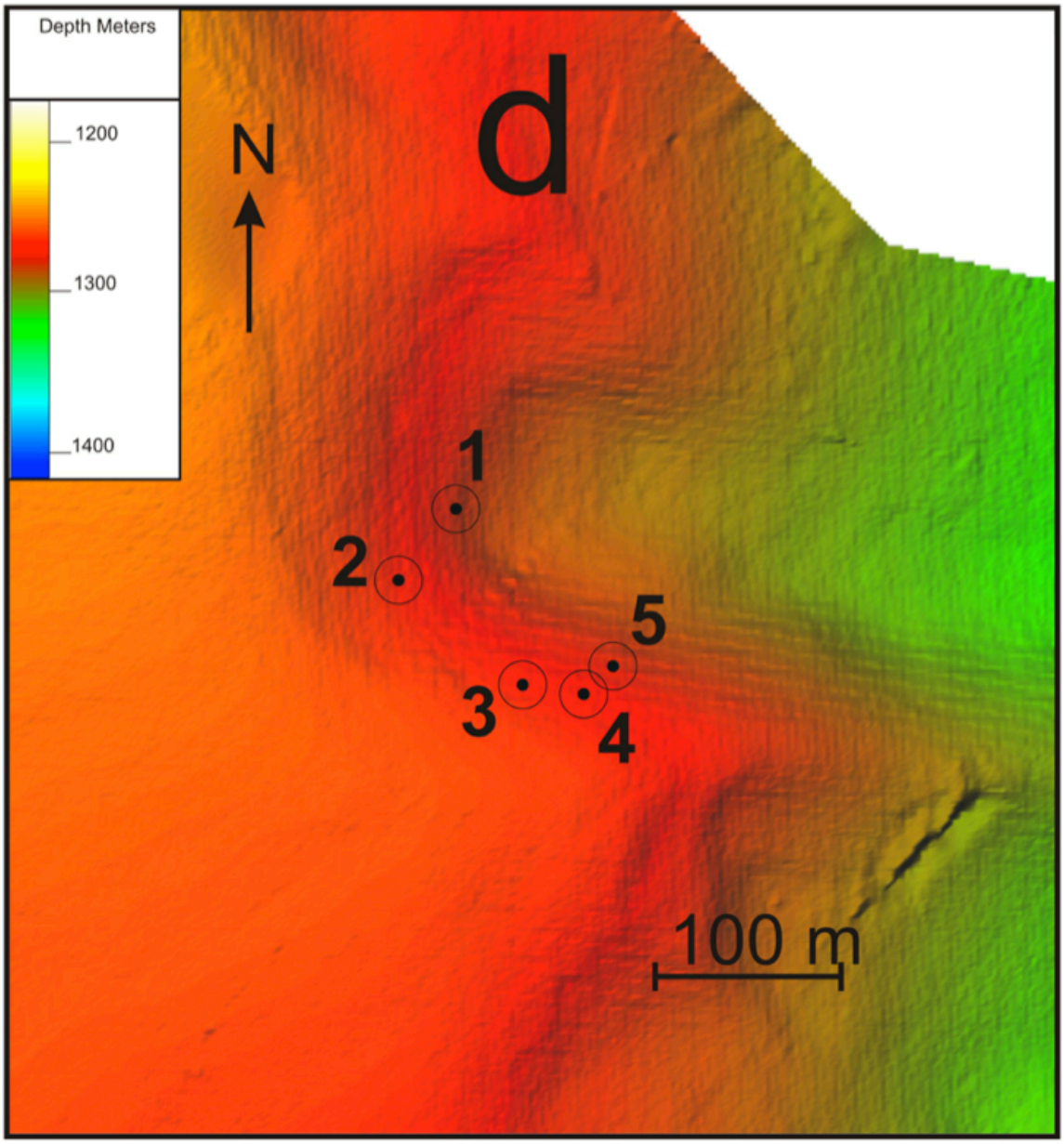

Figure 4.5 Bubbly Gulch ROV dive waypoints

Zoomed grid of bubbly gulch, seafloor observations for waypoints 1-5 are seen in Figure 4.9.

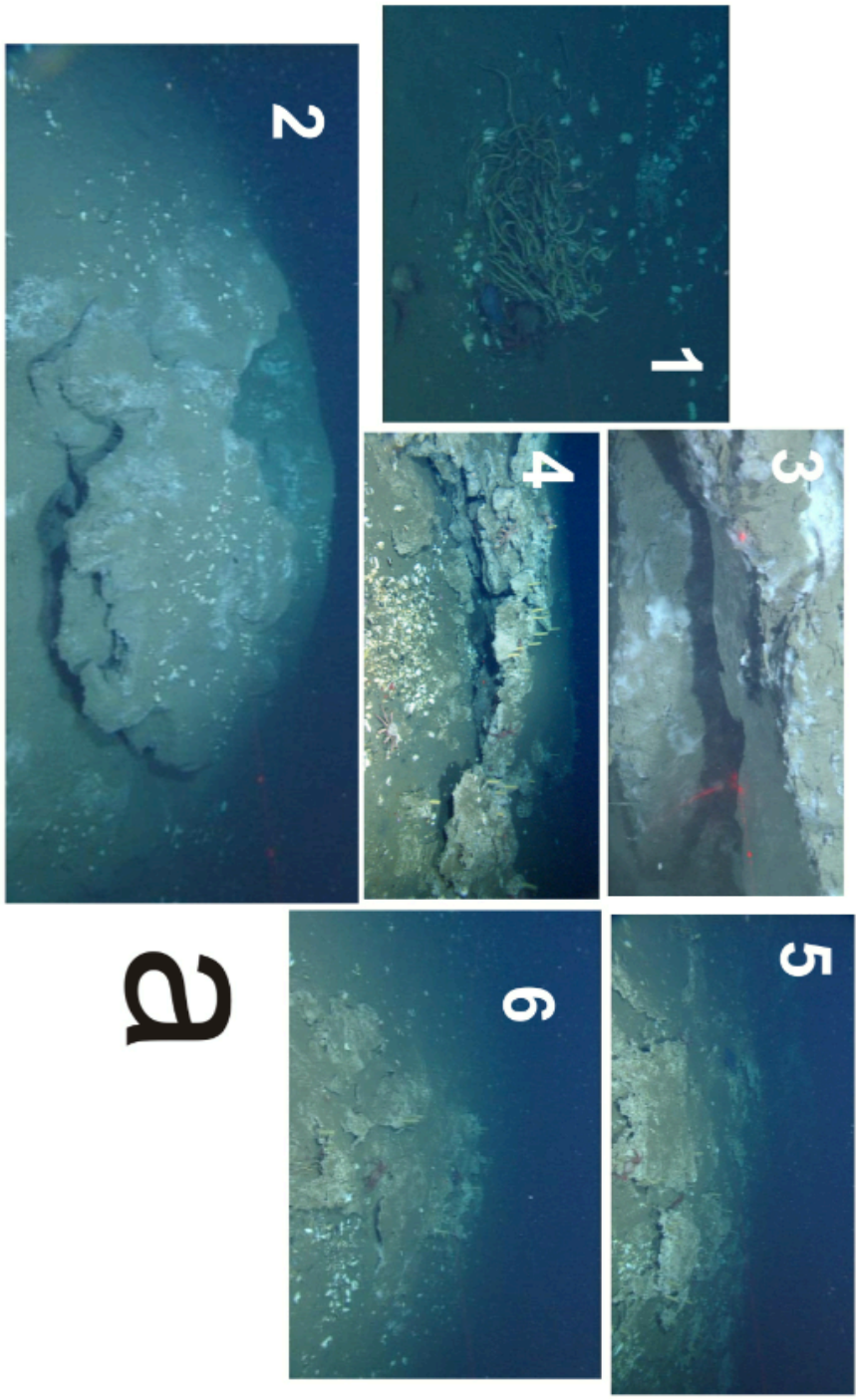

Figure 4.6 ROV dive images Spinnaker Vent

ROV dive at Spinnaker Vent with images for waypoints 1-6 in Figure 4.2 showing tubeworms and clams (1), the Spinnaker Vent Feature (2), gas hydrate between layers of carbonate (3), and accumulations of carbonates supporting colonies of tubeworms and shell fragments on the seafloor, (4-6) more accumulations of authigenic carbonate with communities of clams and tubworms.

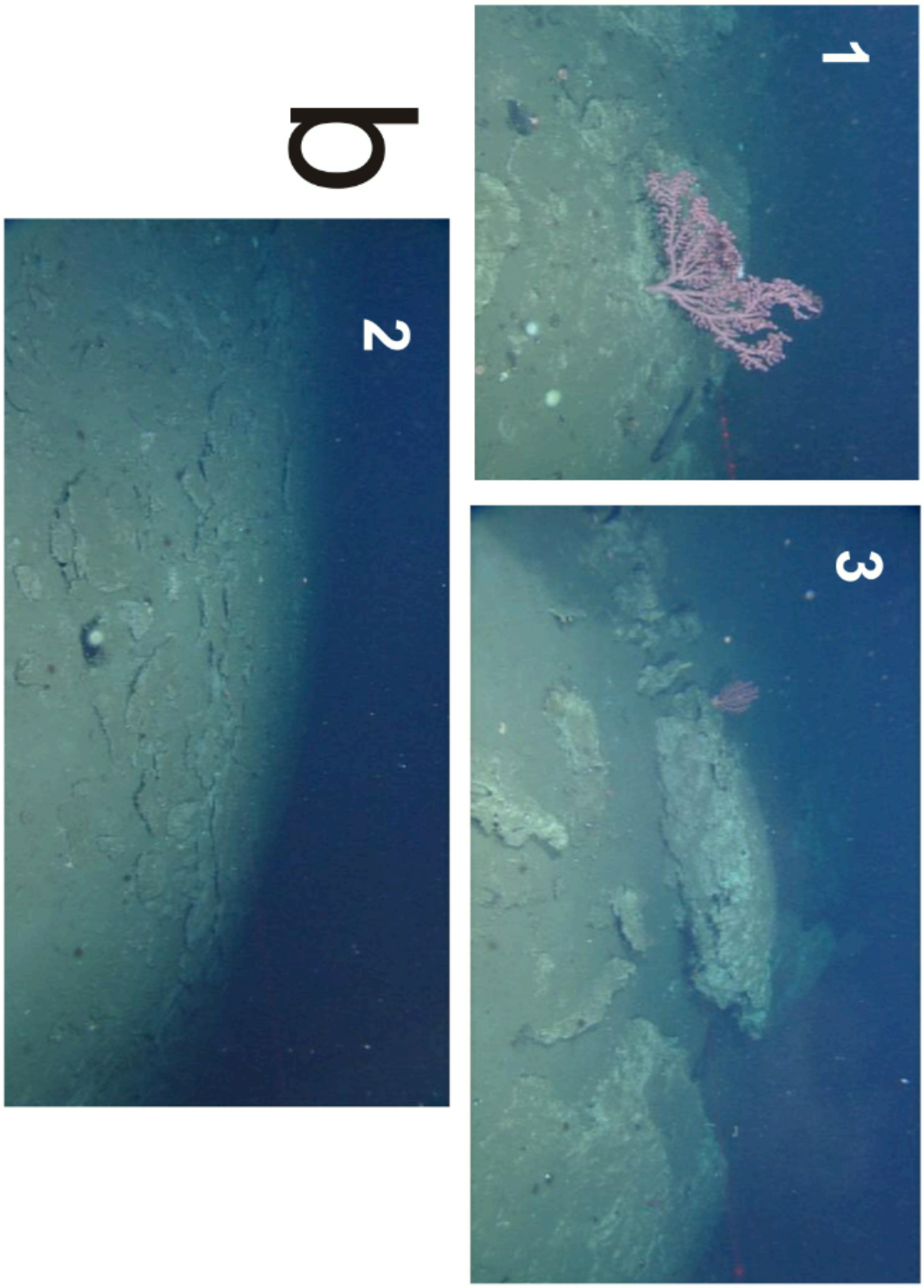

Figure 4.7 ROV dive images Ridge Crest Crater

ROV dive at Ridge Crest Crater with images for waypoints 1-3 in Figure 4.3 showing bubble gum coral (1), large carbonate slabs (2), and carbonate pavements approaching the crater (3).

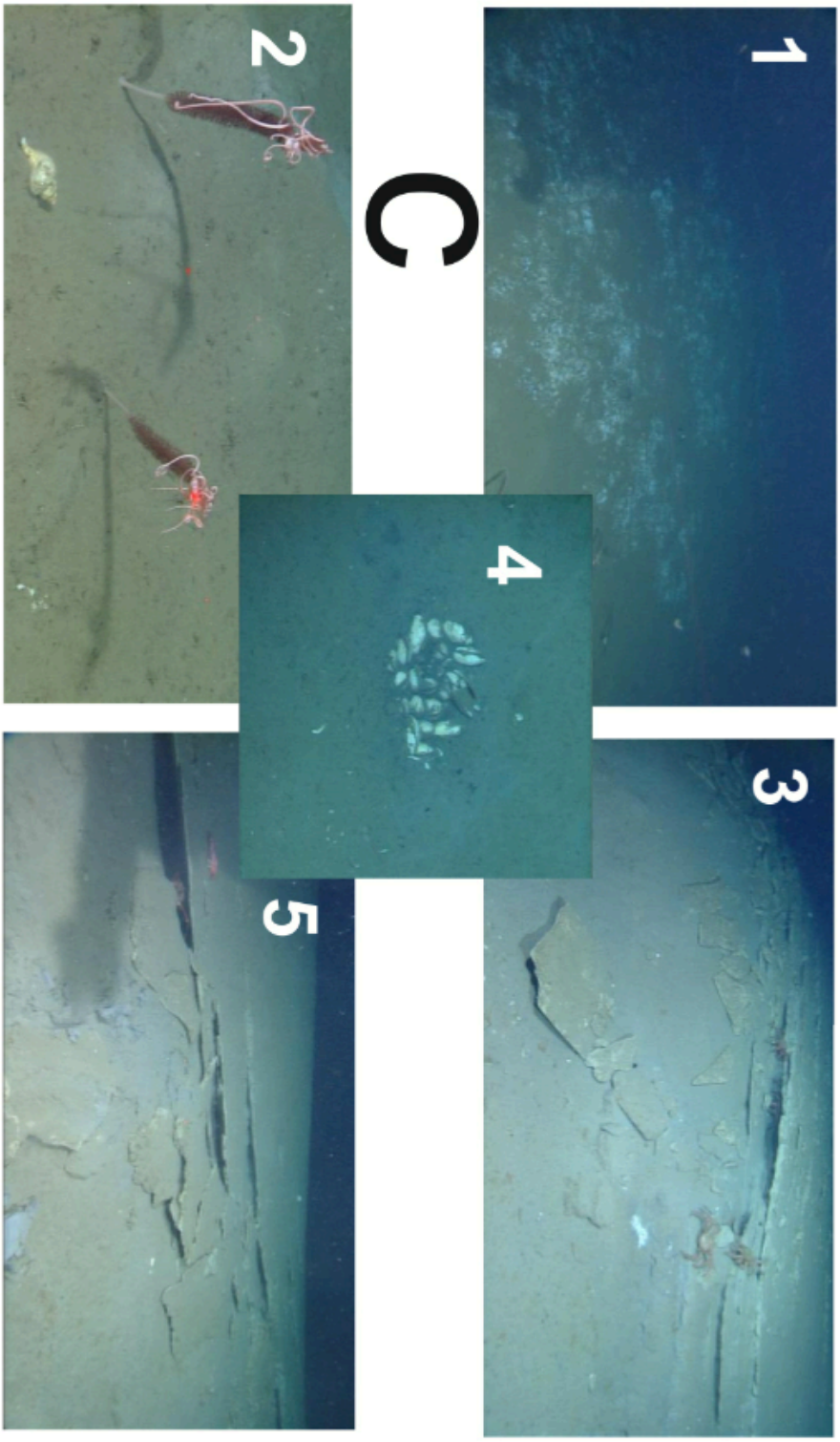

Figure 4.8 ROV dive images Bullseye Vent

ROV dive at Bullseye Vent with images for waypoints 1-5 in Figure 4.4 showing bacterial mats (1), sea pens (2), carbonate pavements (3,5), and a small depression with clams (4).

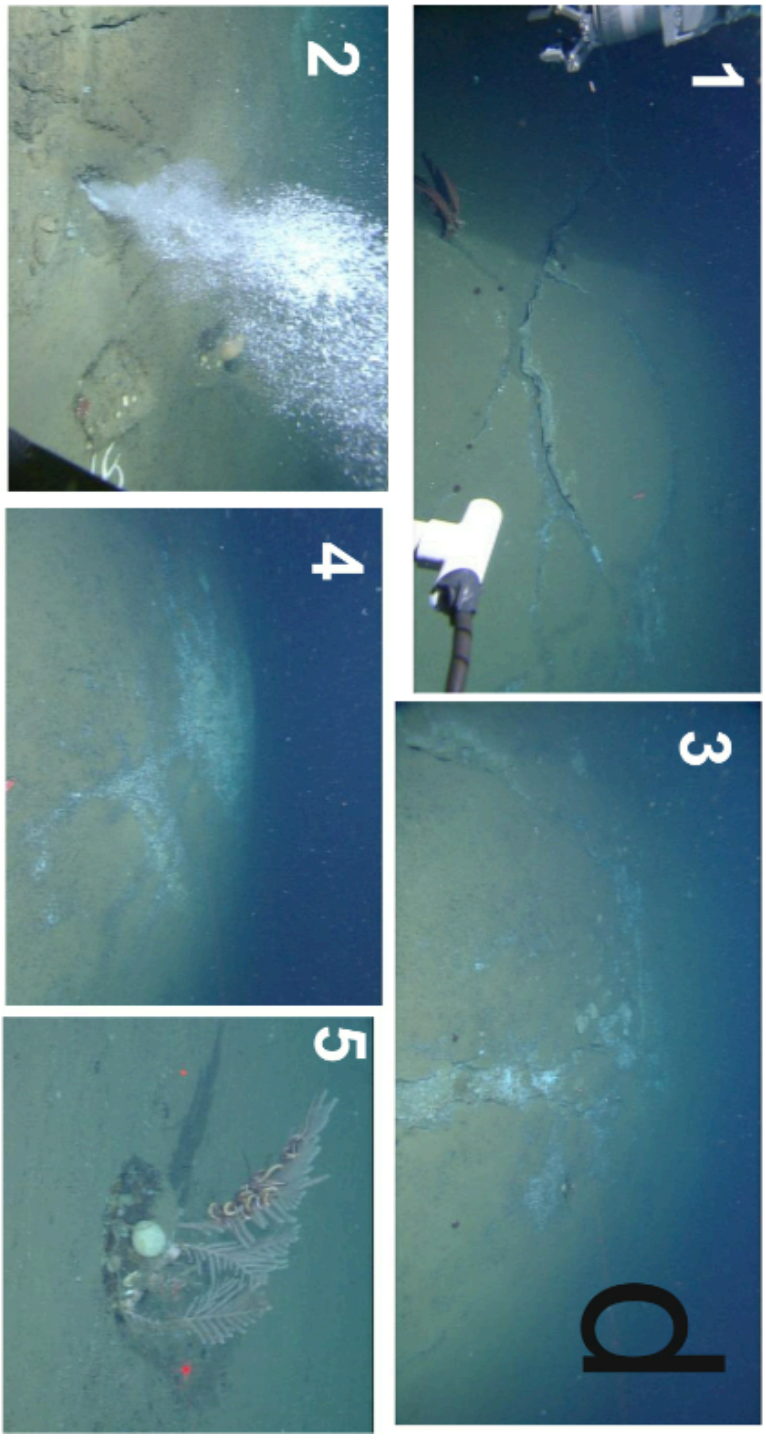

Figure 4.9 ROV dive images Bubbly Gulch

ROV dive at Spinnaker Vent with images for waypoints 1-6 in Figure 4.5 showing seafloor blister cracks and associated bacterial mats (1, 3, 4), methane degassing (2), and an unknown seafloor plant (5).

4.1.2 Chemosynthetic Communities

Chemosynthetic communities, as visual indicators for methane venting at the seafloor, are seen throughout the region at different venting sites. In the northern portion of the study region at Spinnaker Vent, many tubeworms, clams, and bacterial mats were seen. Figure 4.6 shows CBC associated with Spinnaker Vent in the north.

At Bullseye Vent, an area previously studied and investigated by ROVs, almost no communities are seen. The vent area itself is roughly 350 m long and 100 m wide. Northeast and southwest of Bullseye Vent trending along roughly the same azimuth, the seafloor is coated with expansive bacterial mats and active methane bubbling from the surface. These fine-scale seafloor bacterial mats are not discernable on the bathymetry; however, side-scan sonar data show distinctive backscatter highs through this region of biological activity. Figure 4.8(1) shows bacterial mats encountered approaching Spinnaker Vent from the southwest. Bacterial mats become wider northeast towards Bubbly Gulch along the Bullseye Vent strike.

4.1.3 Authigenic Carbonates

Ridge Crest Crater (central), Cucumber Ridge (north-west), Bullseye Vent (south), and Spinnaker Vent (north-east) all contain accumulations of authigenic carbonate. Carbonate may develop as in thin pavements, large carbonate slabs, or as carbonate aggregate often associated with biological activity. Figures 4.6-4.9 show a variety of different carbonates seen during ROV dives in this study area.

4.1.4 ROV Sonar

ROV observations at the site of intermediate reflectivity northeast of Bullseye Vent showed large bubbles plumes extending >50 m above the seafloor. These methane bubble plumes had large tails and could be easily observed from 50 m away through the ROV-mounted sonar (Figure 4.10). The irregular yet intensive venting patterns in this area are documented during the ROV track between Bubbly Gulch and Bullseye Vent.

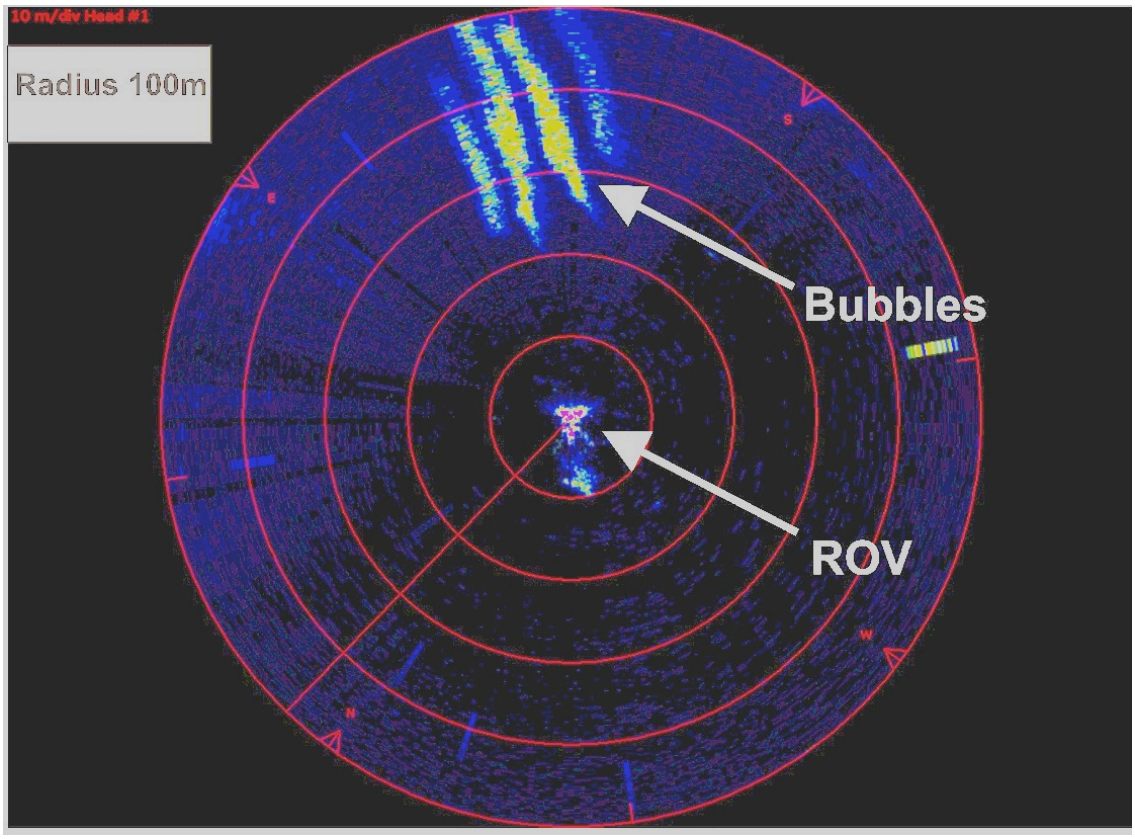

Figure 4.10 ROV Sonar Bubble Plumes

ROV Sonar showing bubble plumes and their tails. This sonar image was recorded from the ROV mounted sonar showing the distance to bubbles plumes emanating from the seafloor nearby. The bubbles expand as they rise from the seafloor and have tails due to their motion in seafloor currents.

4.2 Sediment Core

A shallow push core was collected during the NEPTUNE-Canada cruise of June 2012 to investigate a region of anomalous backscatter low, and a possible high impedance reflector just slightly below the subsurface. The core was retrieved from mid-continental slope in roughly 1250 m water depth and 1.6 km north of the regional structural high (Ridge Crest Crater) near ODP site 889. Figure 4.1 shows the location of push core site R1554 (yellow circle) and ODP drill site 889 (blue circle). A total 49 cm of core was retrieved by the ROV ROPOS showing a rich history in a short sediment sequence. Figure 4.11 shows the core R1554 with a Munsell Color scale.

4.2.1 Core Description

The base of the core is marked by grey (inorganic) clay glacial remains, followed by intermittent sandy turbidite packages separated by hemipalagic mud deposits (total thickness of 20 cm). At the top of the core is a 22 cm sandy mud package with the near surface (9-14 cm) having a more brown to olive color. This top-most layer of a slightly more brown-olive color is interpreted as either a reworking of the shallow near surface sediment column by either physical or biological processes, or as a separate layer entirely due to a change in sediment source. Figure 4.12 shows an image of the core and a more detailed description. However, in this thesis, the origin of the material is not further investigated (although carbon-dating on foraminifera is being conducted, but was not completed by the time of submission of the thesis) and only physical property measurements and how they relate to the AUV data are being analyzed.

4.2.2 Physical Properties

Physical property measurements were conducted on the core, for which P-wave velocity, density, and magnetic susceptibility were measured (Figure 4.13). Sand packages show P-wave velocity highs of 1760 m/s and densities of near 2.2 g/cm^3. P-wave velocities of the mud vary between 1400-1500 m/s with densities of 1.4-1.6 g/cm^3. Much of the near-surface velocities were not displayed due a loss in measurement quality, a possible result from core dewatering. The magnetic susceptibility increases gradually with depth until the lower-most clay layer is reached at ~40 cm below seafloor.

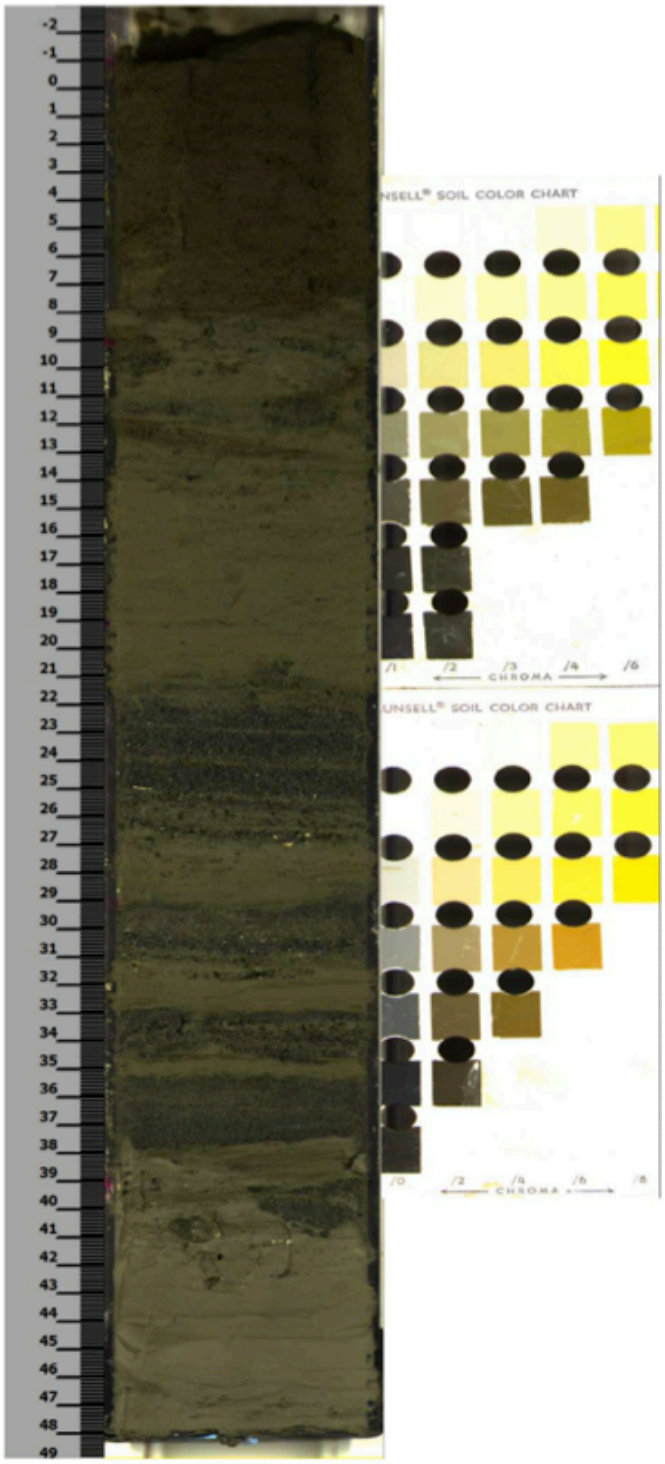

Figure 4.11 Core R1554 With Munsell Colors

Sediment core photo with Munsell Colors, muds are near 5Y 4/2.

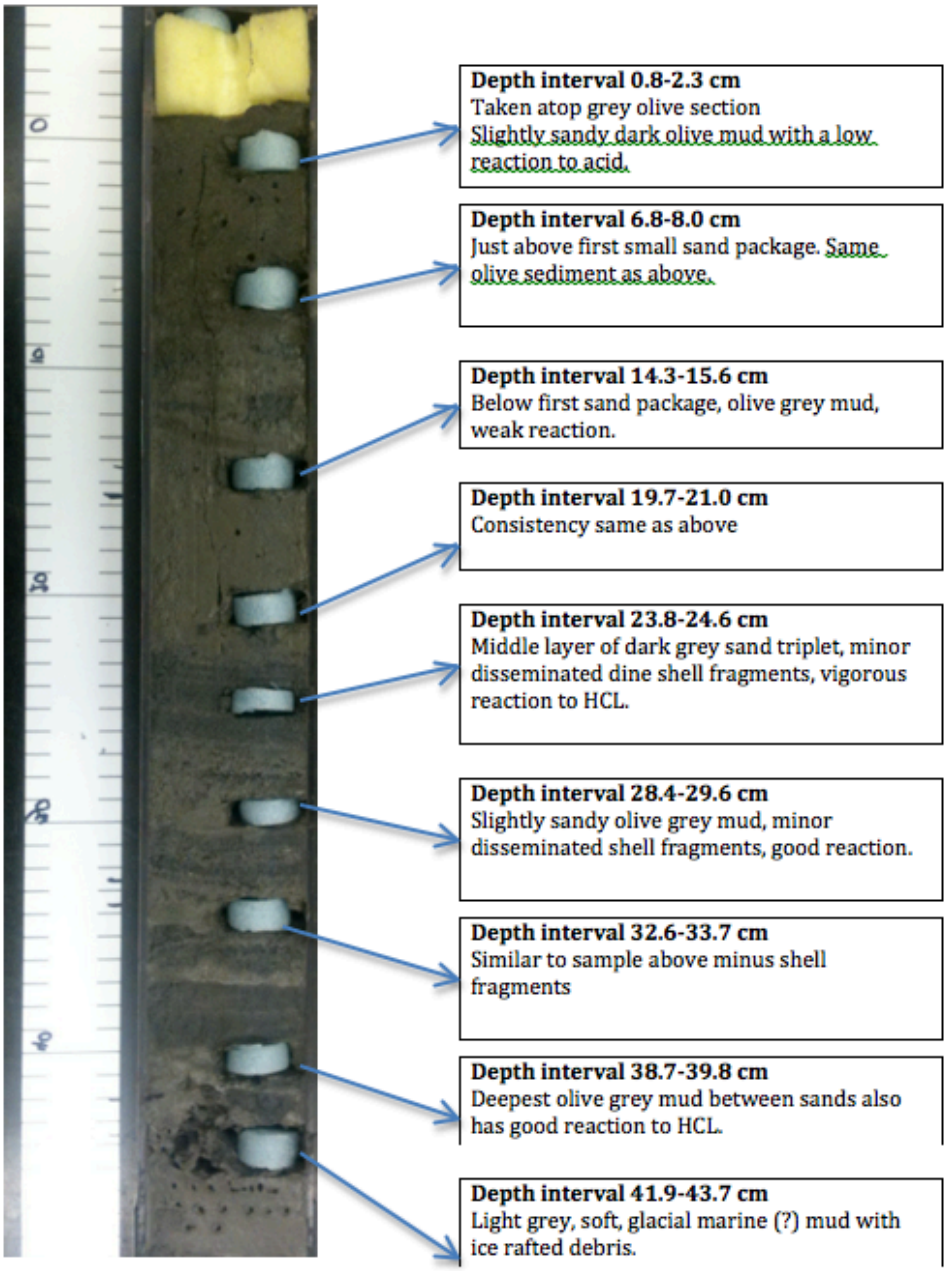

Figure 4.12 Sediment Core R1554 Description

Sediment description for core R1554, the top 20 cm are mostly mud, the middle 20 cm have turbidite sequences, and the bottom 10 cm is clay.

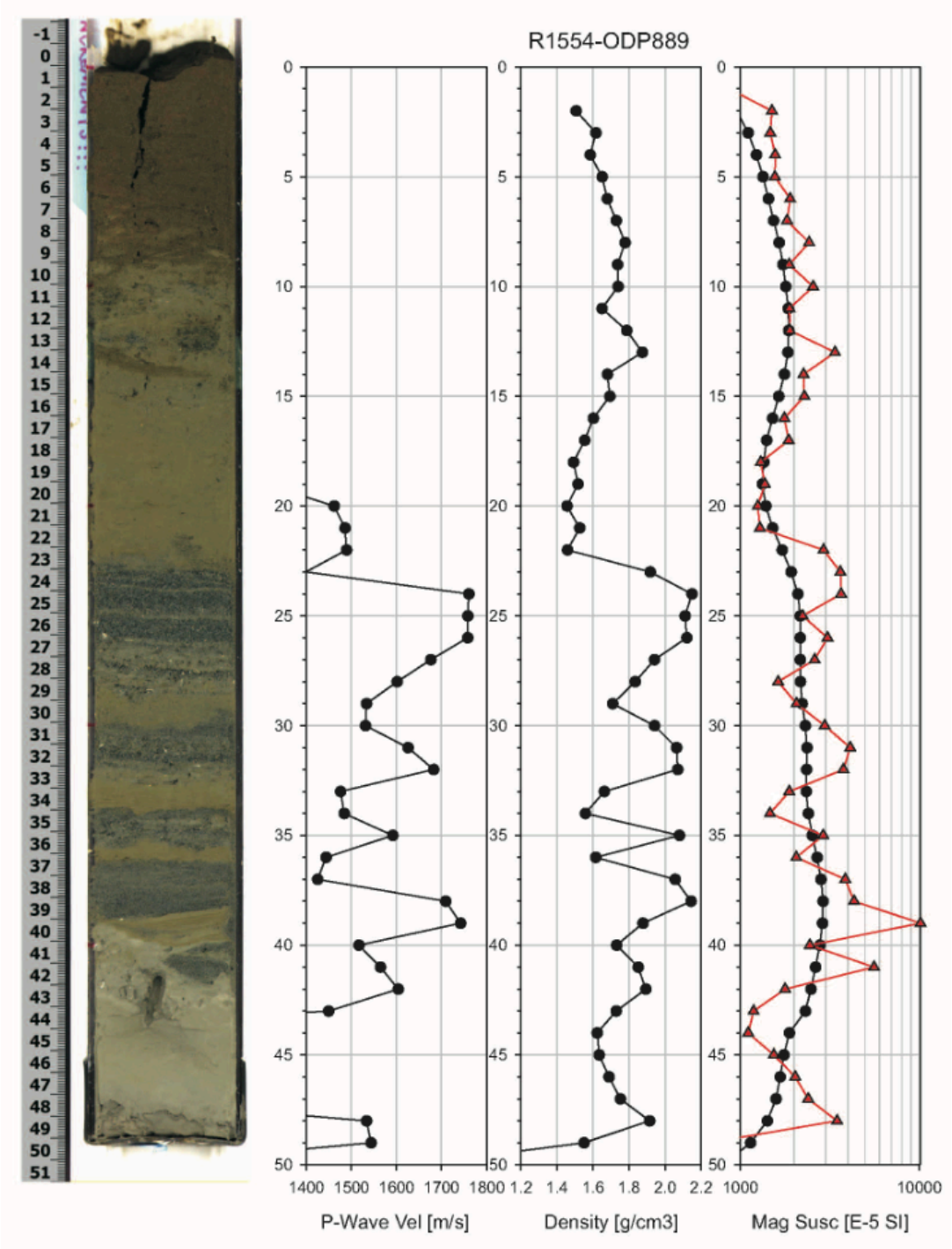

Figure 4.13 Core R1554 Physical Properties

Calculated physical properties are P-wave velocity, density, and magnetic susceptibility.

4.2.3 Carbon Dating

The carbon dating results for samples taken from core R1554 (Figure 4.12) are shown in Table 4.1. Only six of the nine samples were dated; the top two samples within the mud unit are devoid of foraminifera and contain mostly lithic sediments with quartz and muscovite. Sediments of Holocene age are not encountered in the samples that are dateable (below 14 cm). The samples below 14 cm range in age from near ~1300 years to a maximum of ~21,00 years. Generally the sediment does not show a standard depositional history (age increasing lineally with depth). Most of the sediment ages taken within the mud show ages of ~1300 years to ~1500 years, and correspond with mid to late Pleistocene. The only outlier, and the oldest sample (20,800 years) was taken in the sand unit of a turbidite sequence (depth 23.8-24.6 cm, Figure 4.12). This sample places an age to the sands that were transported to this area (early to mid Pleistocene) during a turbid event.

Table 4.1

Foraminifera Carbon Dating

Depth	Age	Age Error	δ13C	Δ14C
14.3-15.6 cm	14,950	55	-0.57	-845.49
19.7-21.0 cm	12,300	40	-0.48	-785.05
23.8-24.6 cm	20,800	110	-0.63	-925.62
28.4-29.6 cm	14,150	60	-0.16	-829.84
32.6-33.7 cm	12,850	45	-0.61	-799.93
41.9-43.7 cm	13,700	55	-0.69	-819.83

Table 4.1: The carbon dates and of foraminifera samples with age errors, δ13C (VPDB), and Δ14C (radioactive activity) taken from core R1554. Sample locations are seen in Figure 4.12. Samples are dated by National Ocean Sciences Accelerator Mass Spectrometry (NOSAMS) facility.

4.3 AUV Observations

Due to the abundance of evidence for venting and data sets collected with the AUV and ROVs, individually screening all bathymetry pockmarks or sub-bottom profiler lines in this thesis would be cumbersome. Alternatively, this thesis will investigate the most prominent vent sites of interest for potential future IODP drilling or for site investigation with NEPTUNE-Canada as previously outlined in Chapter 3. Looking at multiple data sets for a given site is done to provide a comprehensive understanding of the site. Specific sites will be investigated in order from roughly north to south by examining (1) high-resolution bathymetry, (2) sub-bottom profiler data, and (3) side-scan reflectivity (backscatter). Where available, AUV seafloor-data are combined with still photos taken during the ROV investigations.

(1) Compared to the regional bathymetry data over the accretionary margin, the AUV bathymetry shows much improved vertical and horizontal resolution; larger structures (> 5 m) are better resolved and smaller features that were otherwise not visible are exposed. The resolution of the bathymetry allows inspection for subtle changes (< 1m) in seafloor morphology, elucidating known vent sites, discovering new vent sites, and mapping seafloor expressions of other structural features. Figure 4.14 shows features that stand out from the bathymetry previously identified (Figure 4.1). The dashed arrows partially enclosing sites A through E show the viewing direction from which these sites will be viewed in three dimensions.

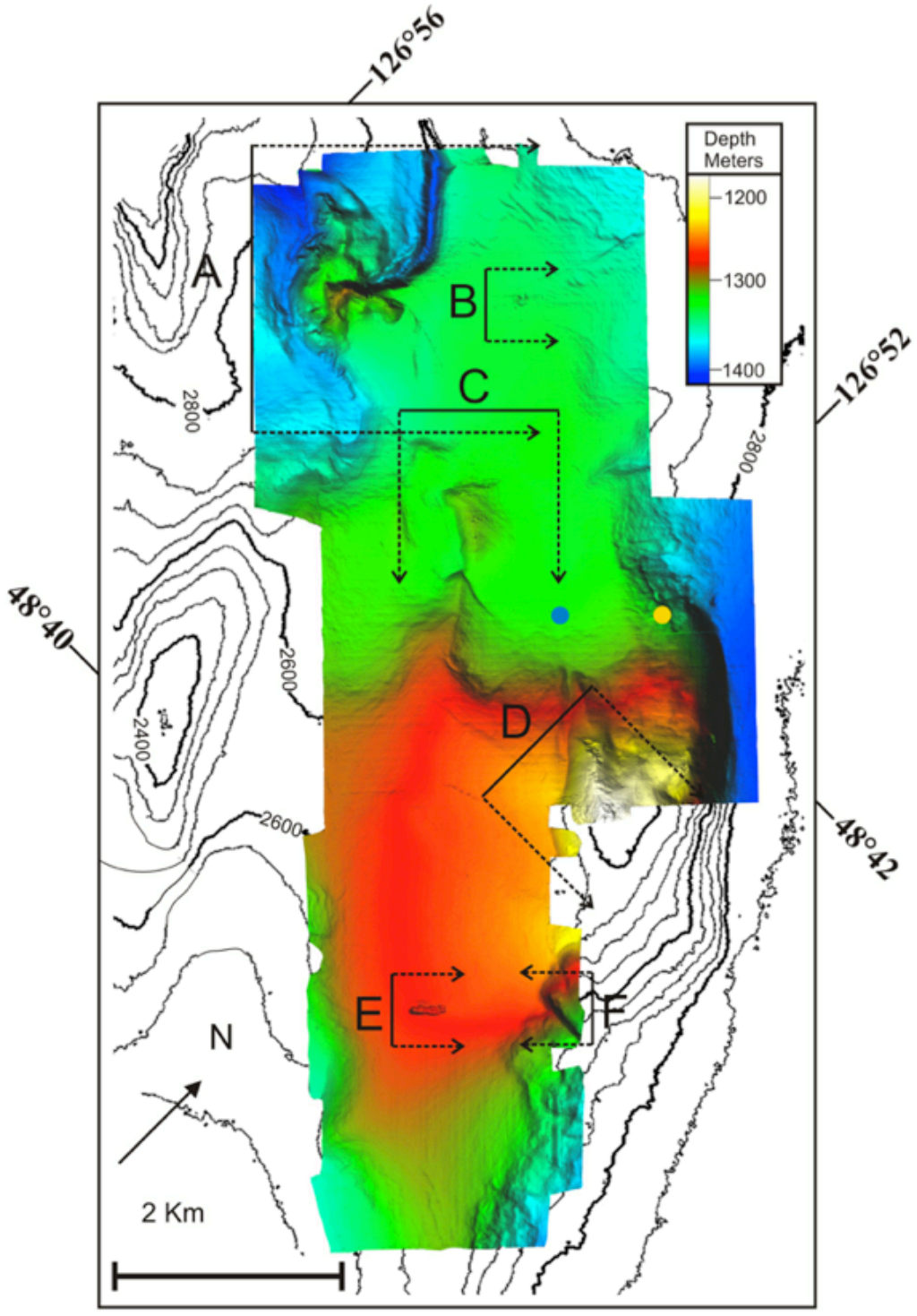

Figure 4.14 Regional Bathymetry With 3D Image Locations.

This regional bathymetry map outlines the locations of 3D images A-F. Description of vent sites progress north to south with Cucumber Ridge (A), Spinnaker Vent (B), Snake Vent (C), Ridge Crest Crater (D), Bullseye Vent (E), and Bubbly Gulch (F). Core R1554 location is shown by the yellow dot, and ODP site 889 is shown by the blue dot.

(2) Acoustic backscatter data allow comparison of the relative hardness of seafloor sediments. The acoustic backscatter map is shown in Figure 4.15 overlain with regional bathymetry. Figure 4.16 shows backscatter values without the bathymetry overlay. The AUV backscatter data are not calibrated to produce quantifiable results. Where ground truth data from ROV expeditions exist (cores, photo), the relative hardness of seafloor sediments allows variations in geology to be inferred. Areas with higher rates of change in seafloor bathymetry have distinctively higher relative backscatter values, potentially because of an incomplete correction for slope affects as discussed in Chapter 3. Acoustic backscatter relationship to seafloor geology will be evaluated in detail in Section 5.3.

(3) Sub-bottom profiler lines through the study area illuminate subsurface structure and shallow sediment geology. These lines add additional context to many of the features already identified in the bathymetry and allow for the discovery of other subsurface features that do not directly show any surface expression such as hardness or bottom roughness in morphology. Figure 4.17 shows the location of sub- bottom profiler lines inspected in this chapter. The vertical scale on these lines is recorded in two-way travel (TWT) time. TWT is the time it takes for a seismic wave to travel from the source, to the reflective interface, and back to the receiver. In these shallow settings of imaged sub-seafloor, TWT can be easily related to depth by assuming a constant sediment P-wave velocity close to that of water (1500 m/s).

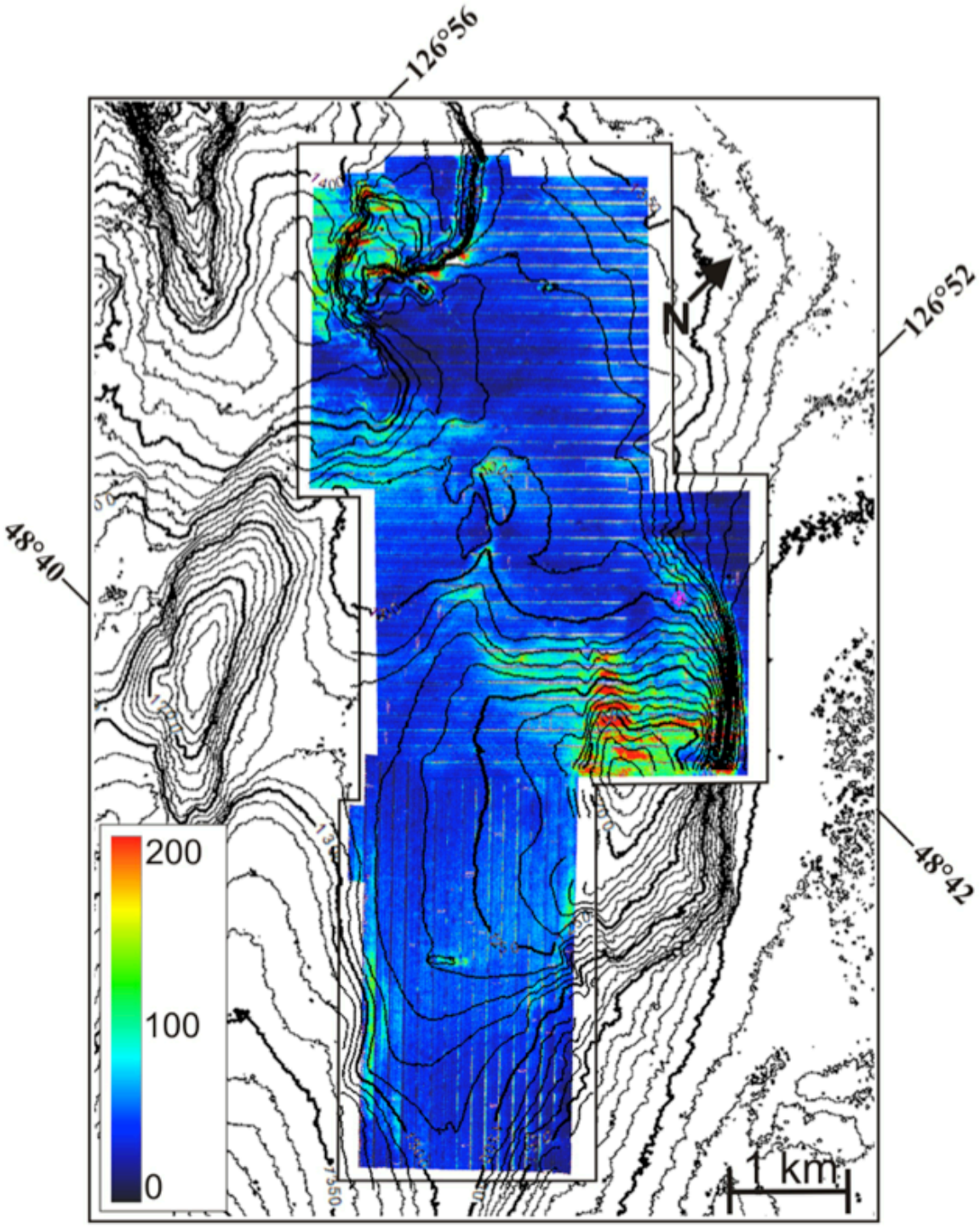

Figure 4.15 Regional backscatter with bathymetry contours

Acoustic backscatter with regional bathymetry overlain. Regional bathymetry is gridded at a smaller contour interval (25 m) than in previous figures (50 m). This is done to achieve parity with the higher resolution gridding of AUV bathymetry shown inside the box surrounding the backscatter measurements.

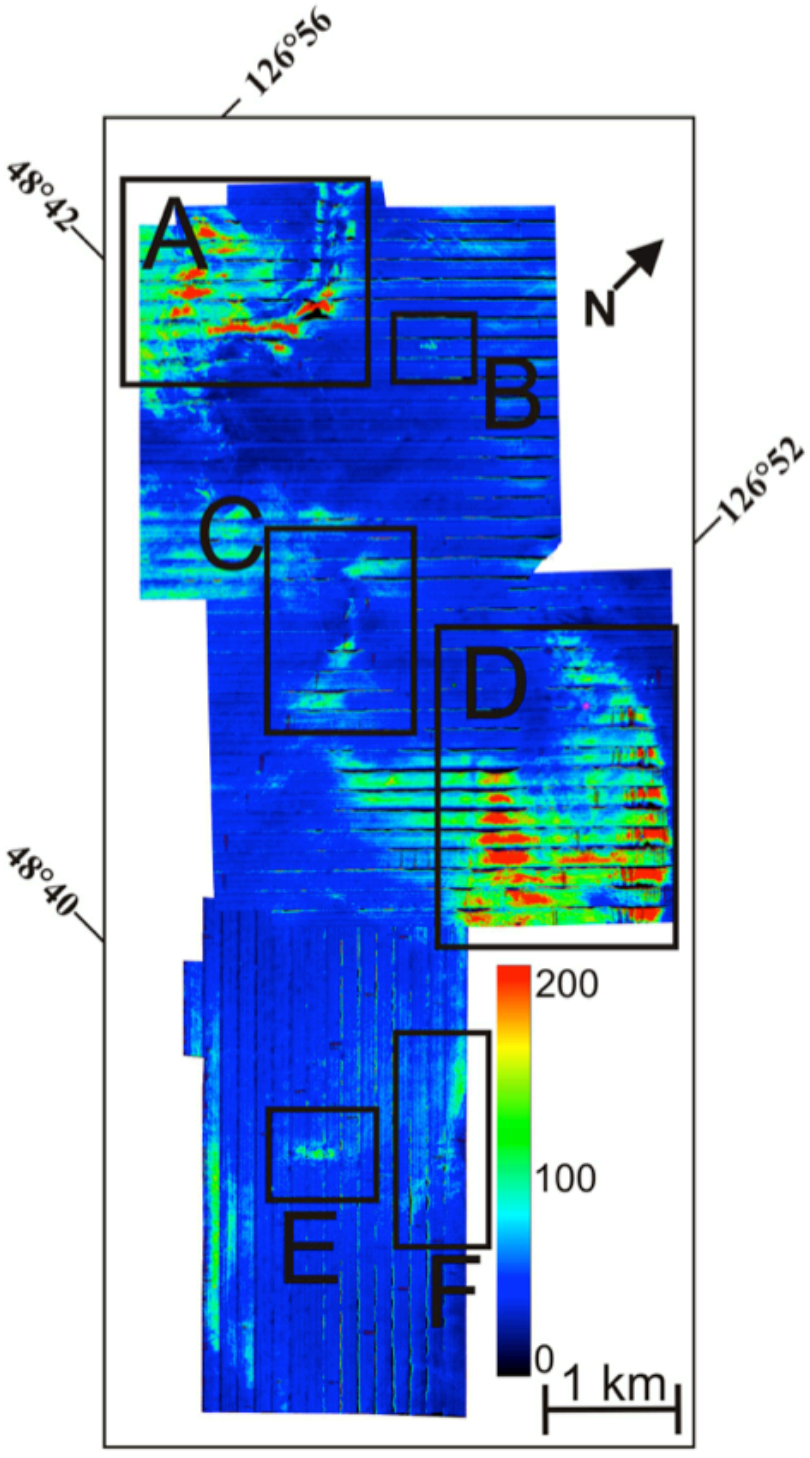

Figure 4.16 Regional backscatter with sites of interest outlined.

Acoustic backscatter with sites of interest A-F boxed in black. The boxed sites are (A) Cucumber Ridge, (B) Spinnaker Vent, (C) Snake Vent, (D) greater Ridge Crest Crater area, (E) Bullseye Vent, and (F) greater Bubbly Gulch area.

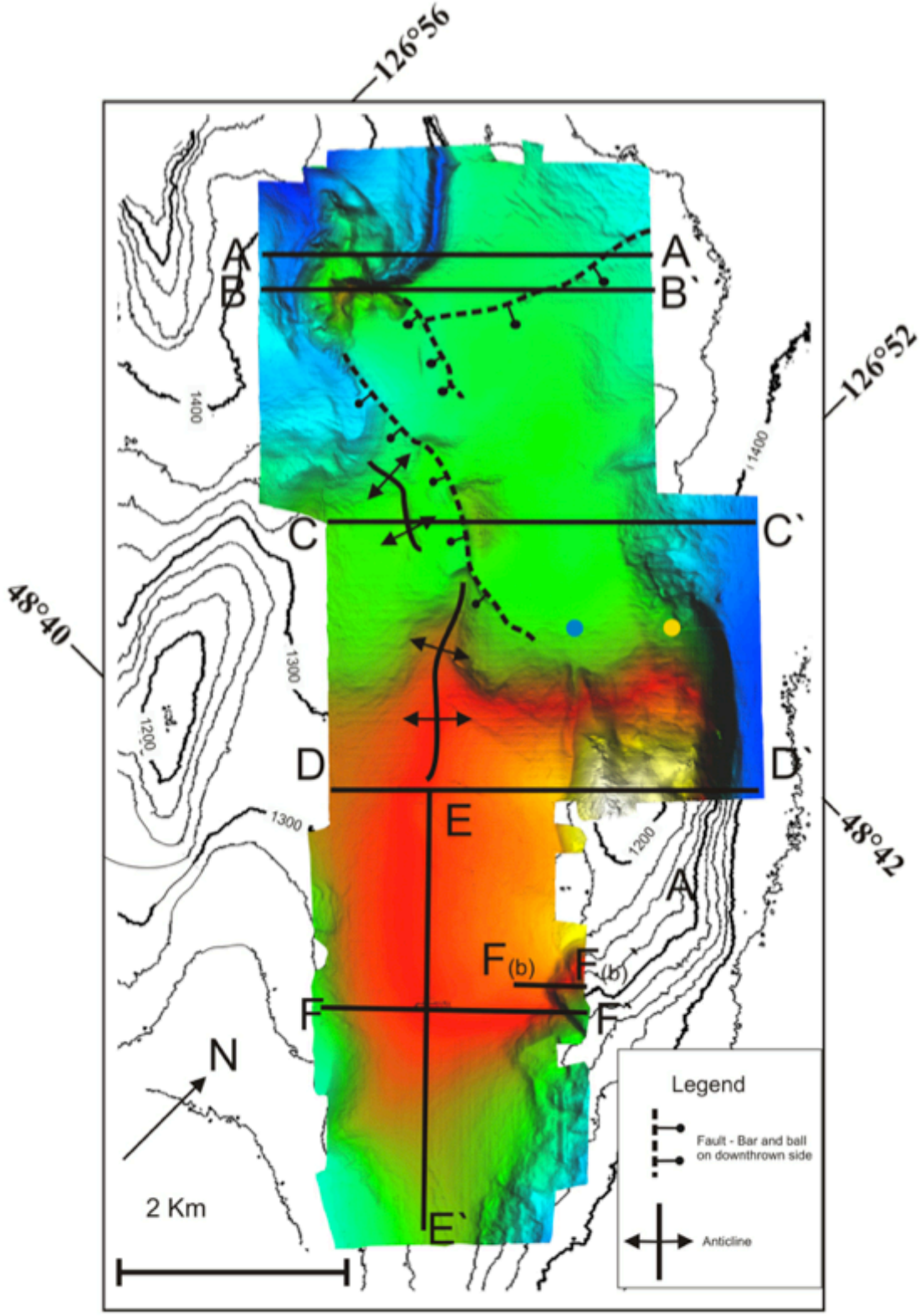

Figure 4.17 High-resolution bathymetry with AUV track lines

Figure 4.17 (previous page): High-resolution bathymetry with selected AUV track lines. Each AUV line is selected to show subsurface structure of sites identified in the bathymetry, (A–A˙) shows Cucumber Ridge, (B-B˙) Spinnaker Vent, (C-C˙) Snake Vent, (D-D˙) Ridge Crest Crater, (E-E˙) Bullseye Vent, and (F-F˙) Bubbly Gulch (and Bullseye Vent). F_b-$F_{b'}$ is small subset transect of Bubbly Gulch showing structure-related stratigraphic venting. The coloured dots show the location of ODP drill hole 889B (Blue) and push core R1554 (Orange).

4.3.1 Cucumber Ridge

Cucumber Ridge shows the largest variability in size and shape of any feature in the study area. The surveyed ridge is only a small part of a longer northwest-southeast trending ridge system marking the western boundary of the slope basin in the study area. The ridge has the greatest seafloor slopes surveyed by the AUV with slope angles exceeding 10° to a maximum of 15°. At the base of Cucumber Ridge (on the northwest side) is a previously unrecognized feature, a meandering northwest-southeast trending gully that is slightly deeper (10-20 m) than the seafloor to the west. Figure 4.18 shows a 3D image of Cucumber Ridge with a height of 100 m above the surrounding seafloor sediments.

Backscatter values for Cucumber Ridge are shown in Figure 4.19. The backscatter responses of the ridge are higher than those of the surrounding seafloor. Steep slopes are denoted by backscatter highs (reds), and the highs are truncated to the southeast of the ridge by backscatter lows (blues). These lows southeast of Cucumber Ridge are the lowest observed in the study area and will be discussed in Chapter 5. During dives with the ROV ROPOS in 2000 and 2001 (Riedel, 2001; He, 2007) extensive carbonate outcrops were identified all along the slopes of Cucumber Ridge.

Sub-bottom profiler data for Cucumber Ridge are shown in Figure 4.20 and Figure 4.23 (line 20090724_0035 and line 20090734_0031). Both Figure 4.20 and Figure 4.23 (presented in Section 4.3.2 with Spinnaker Vent) show the ridge between shot points 500-1500. The majority of the ridge shows no internal structure. The ridge lacks internal reflections is especially apparent from shot points 300 to 700, and 1400 to 1800. Some shallow sediment structures are visible between shot points 700 and 1500. Just northeast of the ridge on line 20090724_0035 (Figure 4.20), slope basin strata northeastwardly dipping and seismic penetration is lost at shot point 2400. From shot point 2400 to 4200, a distance of more than 1 km, strata are only imaged in the near surface (10 ms) Deeper strata are resolvable again northeast of shot point 4200.

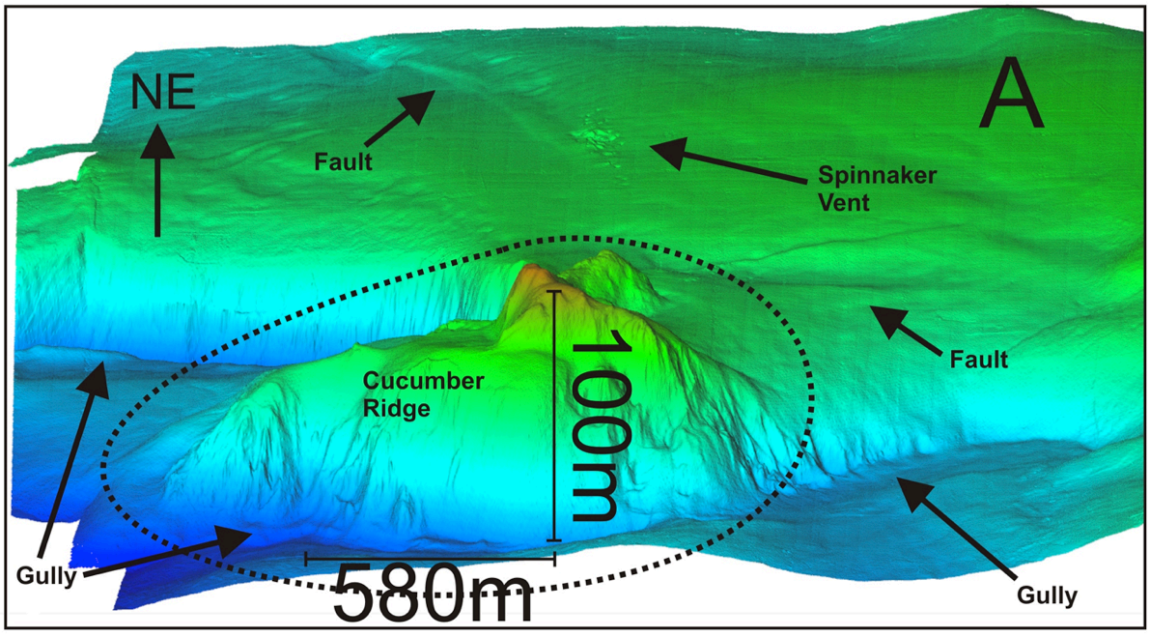

Figure 4.18 3D perspective of Cucumber Ridge

A 3D perspective of Cucumber Ridge looking northeast. For the location of the ridge see Figure 4.14(A). Seafloor slopes have angles of 10° to a maximum of 15°, and are the steepest in this study area. The gully is shown in light to dark blue at the base of the ridge meandering northwest to southeast through the area.

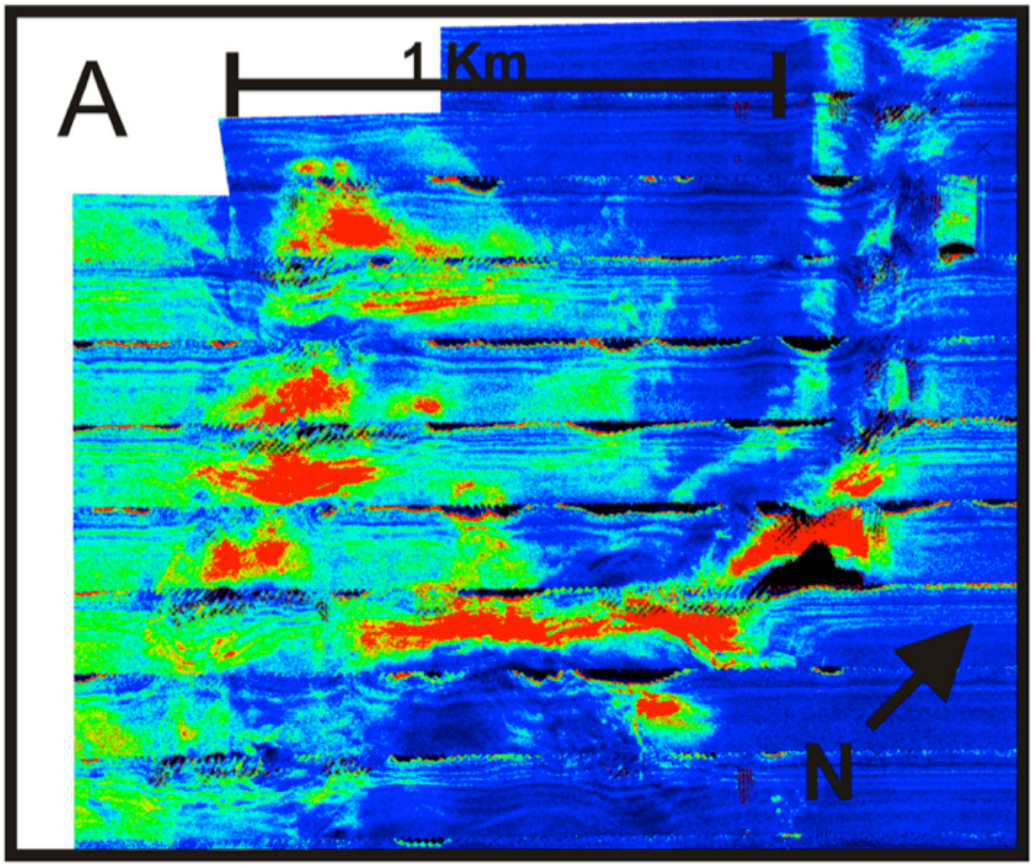

Figure 4.19 Backscatter image of cucumber ridge

Reflectivity measurements at Cucumber Ridge. For the location of the ridge see Figure 4.16, the ridge's backscatter responses are higher than the surrounding seafloor. Slopes are denoted by backscatter highs (reds), however highs are truncated to the southeast of the ridge by backscatter lows (blues). The lows southeast of Cucumber Ridge are among the lowest in the study area and will be inspected in more detail in chapter 5.

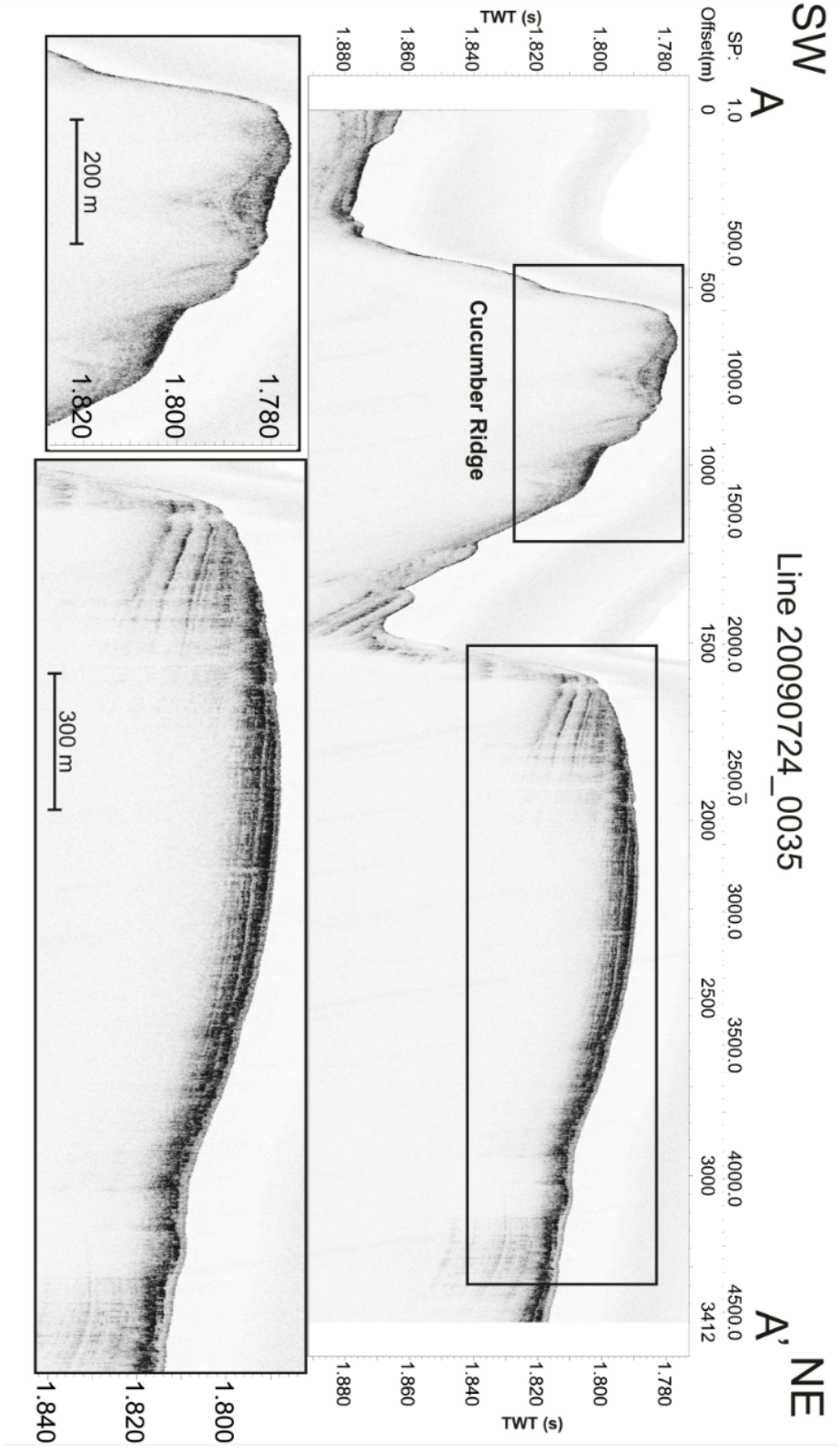

Figure 4.20 Sub-bottom profiler across Cucumber Ridge

Figure 4.20 Sub-bottom profiler across Cucumber Ridge (previous page): AUV profile A-A′ across Cucumber Ridge by AUV line 20090724_0035. The location of the line is shown in Figure 4.17. The transparency of the ridge is apparent between shot points 300 to 700, and 1500 to 2000. The bottom left box shows small amounts of sediment structure visible in the near surface (5-6 ms TWT, or ~4.5 m). The bottom right box shows the loss of acoustic penetration. Strata are dipping northeastwardly as seen between shot points 2100 and 2400. Past shot point 2400, acoustic penetration is reduced to 10ms (TWT) or ~7.5 m for more than a kilometer. At the northeast end of the line, past shot point 4200, deeper strata are again visible.

4.3.2 Spinnaker Vent

In contrast to Cucumber Ridge, Spinnaker Vent is a small bathymetric feature (Figure 4.21). The vent area is defined by a linear trend in pockmarks at the surface oriented off north with an azimuth of 35°. The linear venting trend extends over 500 m and is 150 m wide at its center. Pockmark widths range from 2-3 m diameter at either end of the vent area, while the largest pockmark at the center of the venting trend is 60-65 m in diameter. Pockmark depressions range from a maximum of 1-1.5 m at the center of the trend and decrease to a few tens of centimeters on either end.

Figure 4.22 shows an enhanced view of the reflectivity of Spinnaker Vent. The vent shows relative reflectivity higher than the surround seafloor. Authigenic carbonate and CBC are known to be present at the seafloor of Spinnaker Vent from ROV observations (Chapter 3). East and northeast of the vent, backscatter values increase as part of an east-west trend extending to Ridge Crest Crater.

Sub-bottom profiler data for Spinnaker Vent is best shown in Figure 4.23 by AUV line 20090724__0031. This line is the closest profiler line to Spinnaker Vent; the line runs parallel to the strike of the vent and 75 m northwest of the vent site. Visualization of

Spinnaker vents subsurface is limited by low profiler penetration in this area (Chapter 5 discusses this issue in more detail). Small structure is still visible in the near surface shown in the large box of Figure 4.23. From earlier studies (Riedel et al., 2010; Riedel 2001) it is known that Spinnaker vent is along a major fault system that cuts through the sediments to depths below the BSR.

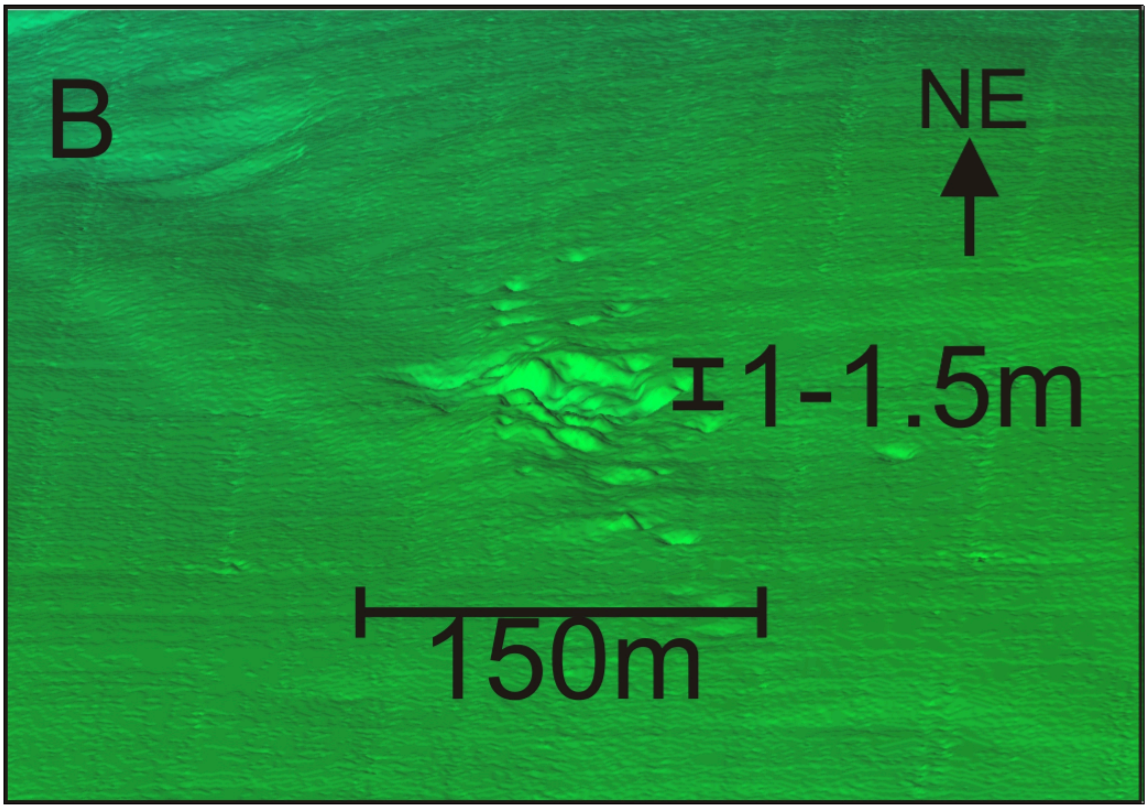

Figure 4.21 3D perspective view of Spinnaker Vent

Spinnaker Vent is ~500 m in length with pockmark diameters ranging form 2-3 m widths at the tip and tail of the venting trend to 60-65 m at vents center. Pockmark depressions range from 1-1.5 m and get shallower towards the tails of the vent until undetectable. The azimuth of the fault running through the area of Spinnaker Vent is 13-18°.

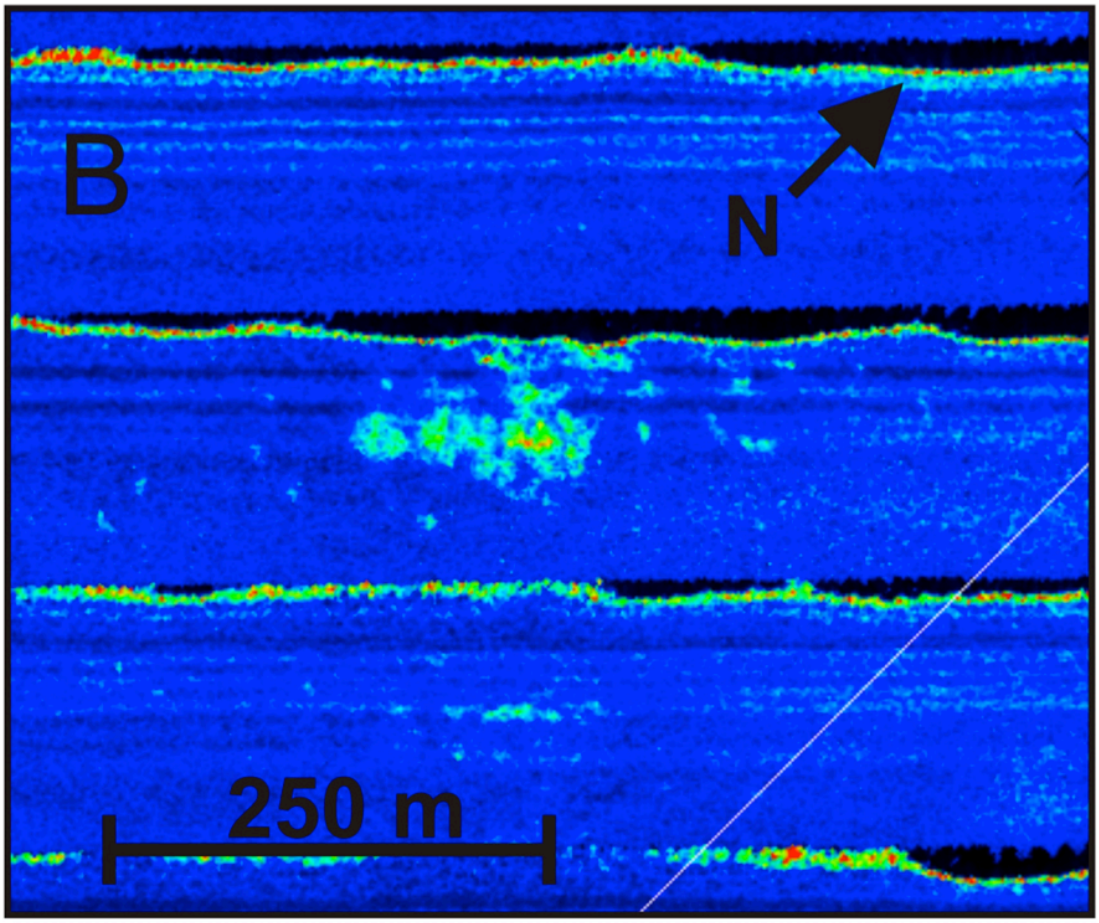

Figure 4.22 Backscatter image of Spinnaker Vent

Reflectivity values at Spinnaker Vent are higher than the surrounding seafloor. Location of figure shown in Figure 4.16. Seafloor authigenic carbonate and CBCs have been documented at the seafloor of Spinnaker Vent by ROV observations (see Chapter 3).

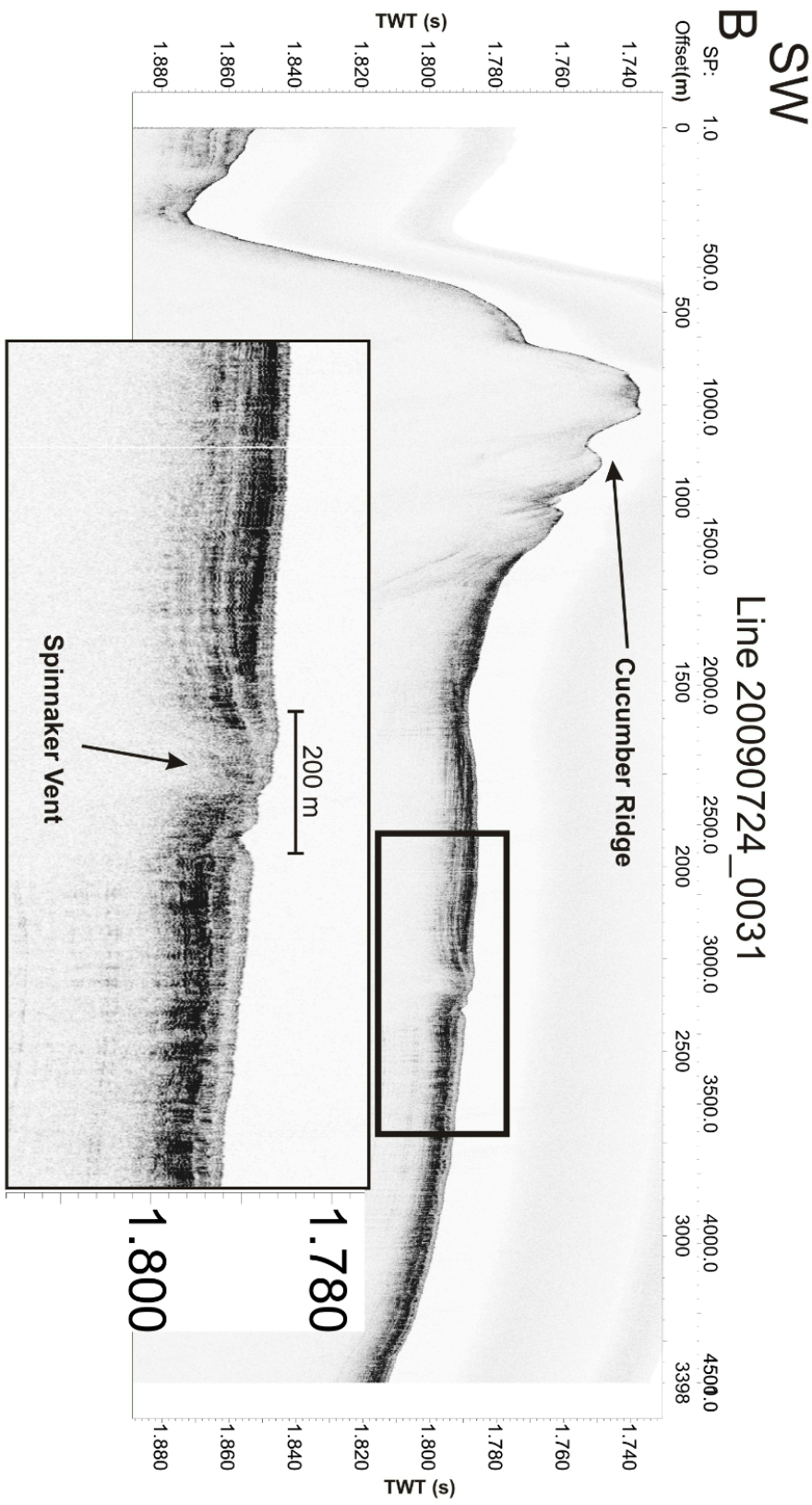

Figure 4.23 Sub-bottom profile across Cucumber Ridge and Spinnaker Vent

Figure 4.23: Sub-bottom profile across Cucumber Ridge and Spinnaker Vent (previous page). AUV profile B-B´ through Spinnaker Vent by AUV line 20090724_0031. The enlargement shows greater detail of the near surface at Spinnaker Vent. This line runs parallel to vent strike 65 m to the north of the vent.

4.3.3 Snake Vent

Snake Vent was not known to exist prior to the acquisition of the AUV data, and it is informally named here in this thesis for the first time. Snake Vent is predicted to be a cold-vent due to it having similar characteristics commonly encountered at other vent sites identified in this study area (i.e. occurs along a fault line, irregular seafloor morphology, high acoustic backscatter, etc.). Its name is based on the "snake"-like curvature of the vent in the regional bathymetry and reflectivity. Figure 4.14 (C) shows the position of Snake Vent in the study area and Figure 4.24 shows the 3-dimensional view of Snake Vent at the seafloor. Pockmarks at the vent range in depth from 0.5 m to 1 m, and pockmark diameters range from 10 m to 40 m. The vent occurs along a roughly northwest to southeast (azimuth 300°) trending seafloor structural high through the center of the slope basin. The change in seafloor bathymetry at this site is 15 m at its steepest (Figure 4.24). Snake Vent lies on the hanging wall of a shallow dipping fault running through the area seen in the bathymetry (Figure 4.17). The seafloor expression of this fault can be followed in the bathymetry from the southern end of Cucumber Ridge to just south of the Snake Vent site.

Backscatter values at Snake Vent are visible in Figure 4.25. Local backscatter measurements are higher (red to yellow) relative to the surrounding seafloor sediment (dark blue). Backscatter values 1 km northwest and 1 km southeast of the Snake Vent

show the snake like character of the seafloor. Reflectivity progresses through the area in a curved pattern with a backscatter high starting south of the vent and progressing north through the venting area. The backscatter highs veers northwest following the fault that connects with Cucumber Ridge (Figure 4.17).

Sub-bottom profiler data through the area is seen in Figure 4.26 along a line perpendicular to the venting trend (profiler line 20090725_0010). Data through this area shows deformed and offset sediment horizons. A prominent sediment fold is visible between shot point 4700 and 4300 with limbs plunging towards the northeast and southwest respectively. The fold axis, plunging towards the northwest, runs roughly perpendicular to the AUV lines. A fault is visible 480 m east of the fold between shot points 3500 and 4000. The fault line extends northwest towards Cucumber Ridge.

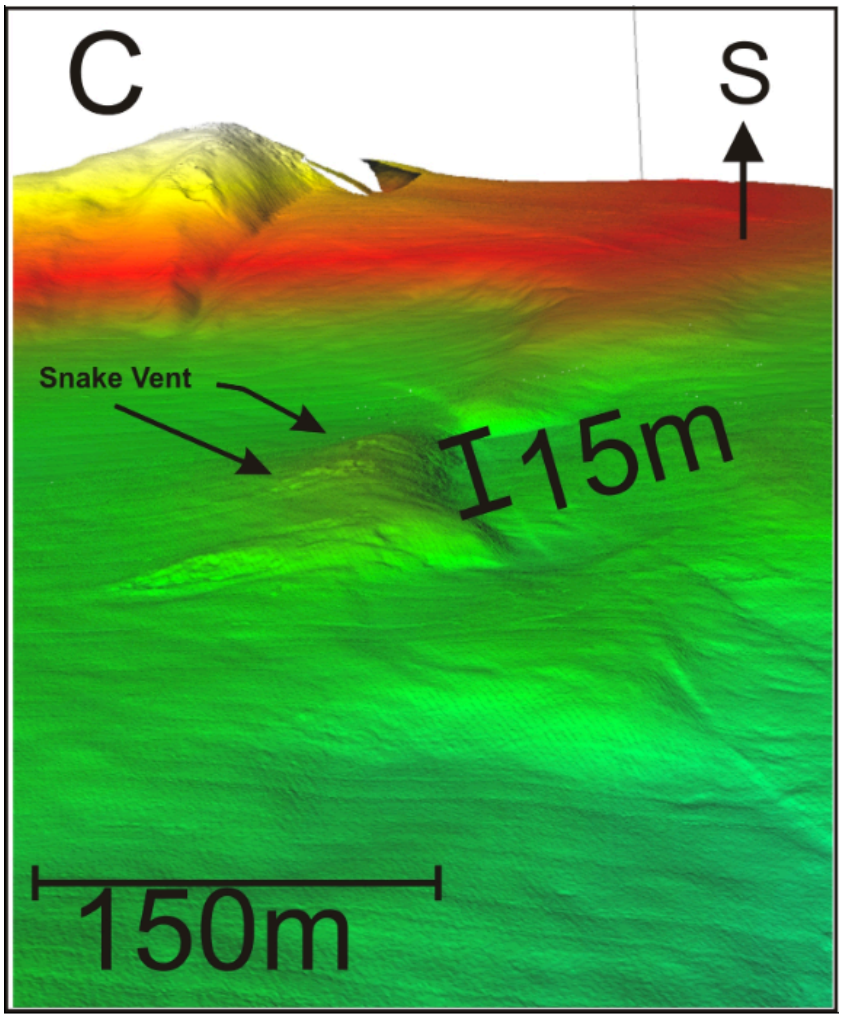

Figure 4.24 3D perspective of Snake Vent

At Snake Vent pockmarks range from 0.5 m to 1 m depth and from 10 m to 40 m in diameter. Changes in bathymetry at this site are 15 m at its steepest point. Snake Vent lies on the hanging wall of a shallow dipping fault (Figure 4.17), and is centered at shot point 3500 of sub-bottom profile 20090725_0010 (Figure 4.26).

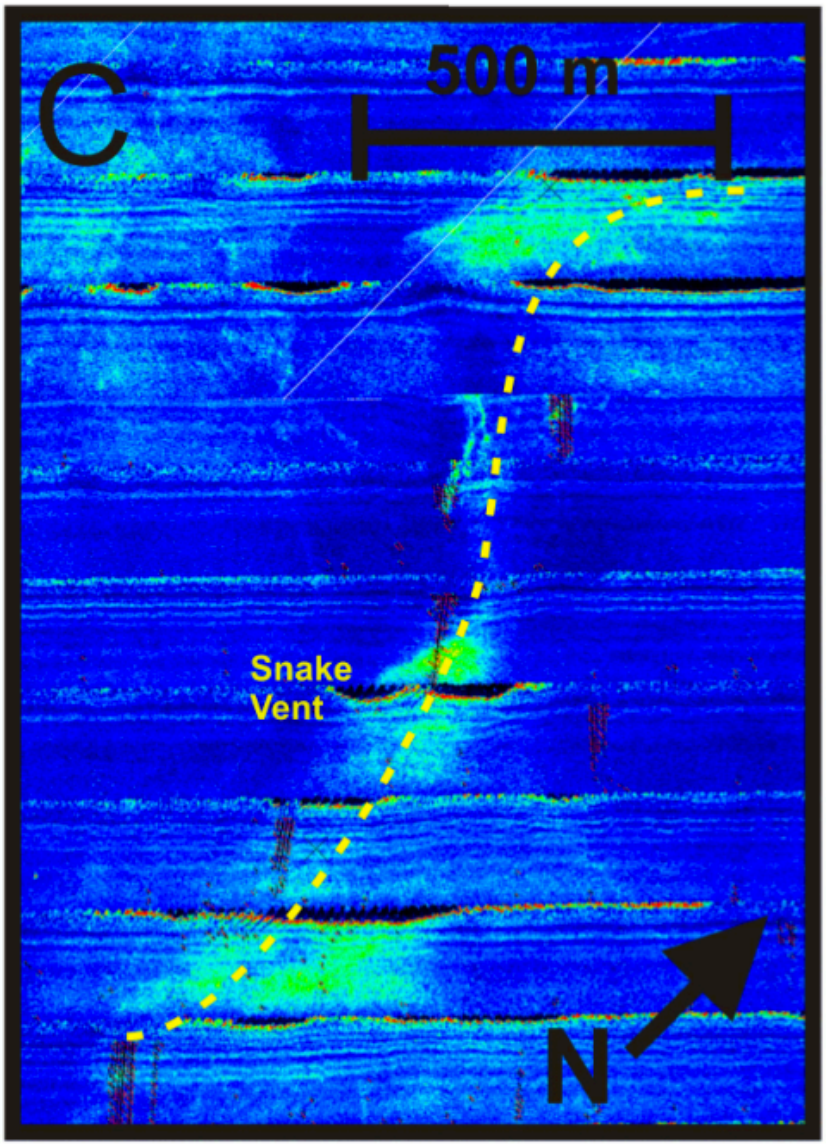

Figure 4.25 Backscatter image of Snake Vent

Reflectivity measurements at Snake Vent, backscatter measurements are higher (red to yellow) relative to the surrounding seafloor (dark blue). Location of figure shown in Figure 4.16. High reflection values bend through the area shown by the light green, and traced by the yellow dashed line.

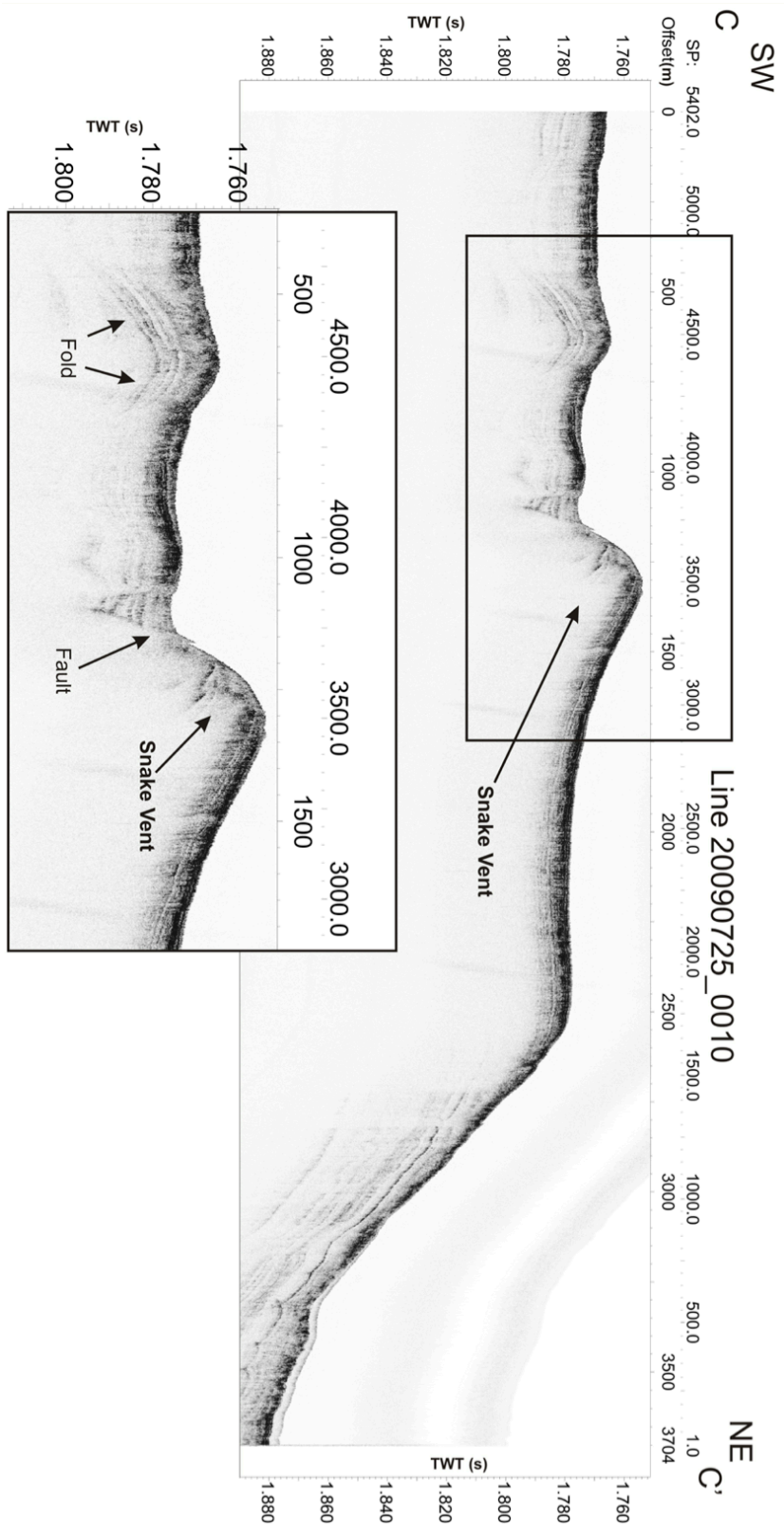

Figure 4.26 Sub-bottom profiler through Snake Vent

Figure 4.26 Sub-bottom profiler through Snake Vent (previous page): AUV profile C-C′ through Snake Vent by AUV line 20090725_0010. Sediment folds are visible between sot pint 4700 and 4300 with limbs plunging towards the northeast and southwest respectively. The fold axis runs roughly perpendicular to the AUV lines plunging towards the northwest. A fault is visible 480 m east of the fold between shot points 3500 and 4000, the fault line extends northwest towards Cucumber Ridge.

4.3.4 Ridge Crest Crater

Ridge Crest Crater, shown in Figure 4.1 (D), is the highest point surveyed by the AUV, and marks the northeast boundary of the slope basin. The topographic highs were previously interpreted as ridges of mostly accreted sediments that lack any coherent reflectivity in conventional seismic data (e.g. Riedel et al., 2002; Yuan et al., 1996). Figure 4.27 shows the 3 dimensional view of the ridge. Ridge Crest Crater is the roughly 9000 m^2 region outlined by the black dashed line. For the purposes of this study, Ridge Crest Crater will be generically described as the summit of the ridge including the lower crater portion. East of the ridge, depths drop to ~1500 meters below sea level (mbsl) in the adjacent slope basin (Figure 2.3). The ridge has a symmetrical surface with its summit at 1230 mbsl. Seafloor slopes are ~7-8° on the southwest and northeast sides of the ridge. The surface of Ridge Crest Crater is heavily pitted with a rough topography associated with the presence of large blocks of authigenic carbonate (Figure 4.7). Depressions are 1.5 m to 5 m deep at the ridge summit and further northwest downslope in the cratered region. Seafloor irregularity extends west downslope from the crest of the ridge. At the western base of the ridge (where the ridge meets the slope basin sediments), a gully deepens towards the northwest from the limits of vertical resolution (50 cm) to 12 m at its northwest limit. The gully can be seen at the base of ridge in Figure 4.27 extending

northwest and truncating at the base of the accreted ridge slope. This rough topography is very similar to that observed with the same AUV tool on Southern Hydrate Ridge (Paull et al., 2009). There, the topography was extensively studied with repeated ROV investigations over many years and has shown that this type of topography is associated with seafloor carbonate outcrops and gas hydrates. The observation of such similar topography on the northern Cascadia margin is significant and changes the interpretation of the role of the topographic highs (as explained in Chapter 5).

Backscatter values at the ridge are the highest observed in the study area. Figure 4.28 shows the backscatter reflectivity for the ridge; reflective highs are apparent at the summit of the ridge, and the highs are maintained moving northwest downslope. Authigenic carbonate (highly reflective) is known to be present at the ridge summit from ROV observations (Figure 4.7).

Sub-bottom profiler data over Ridge Crest Crater (Figure 4.29) shows that no internal reflectors are present at its summit, similar to Cucumber Ridge. Northeast of the summit between shot points 1000 and 2000 stacked strata are visible to a maximum depth of 30 ms TWT below sea floor. Northeast and southwest of the ridge summit, slopes are steep and sub-bottom profiling is unable to image any potential sedimentary structure. Between shot points 2400 and 4500 sedimentary layers in the slope basin rise upwards towards the accretionary ridge. The eastern limit of the slope basin is visible where sedimentary horizons truncate against the slope of the ridge (shot point 2400).

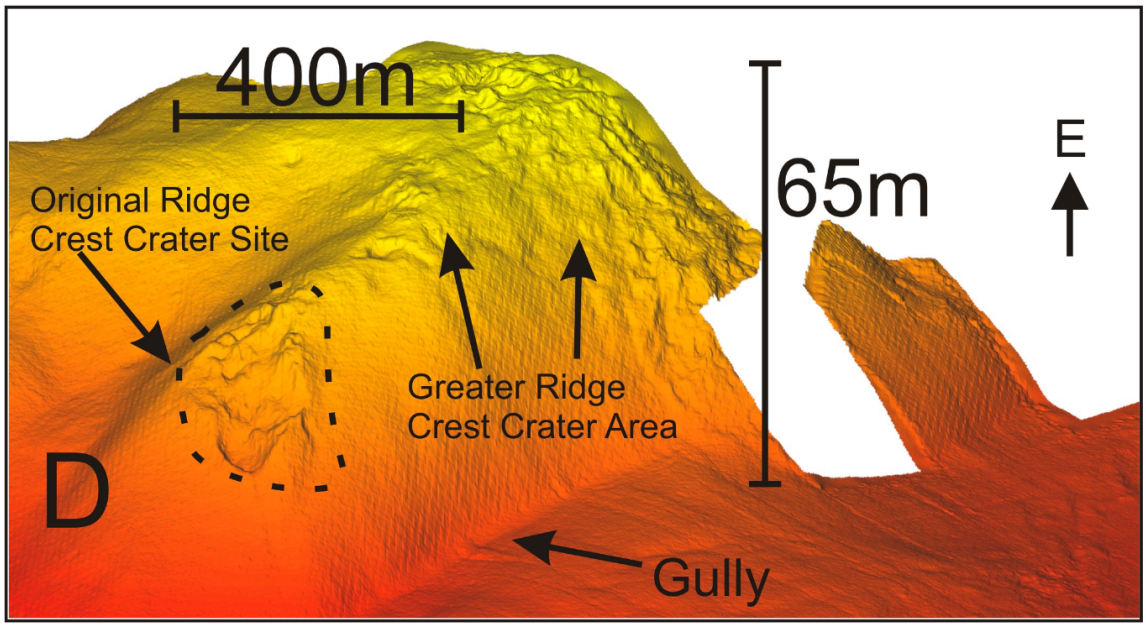

Figure 4.27 3D perspective of Ridge Crest Creater

The crater is the roughly 9000 m^2 region outlined by the black dashed line. This study generically defines Ridge Crest Crater as the fill summit of the ridge including the lower crater portion. Seafloor slopes approaching from the ridge from the southwest or northeast are ~7-8°. Depressions are 1.5 m to 5 m in height at the ridge summit and further northwest downslope in the cratered region. Seafloor irregularity extends west down slope from the crest of the ridge. At the western base of the ridge where the ridge meets the slope basin sediments is a gully that gets deeper towards the northwest form 50 cm to 12 m at its northwest limit (outside of this figure).

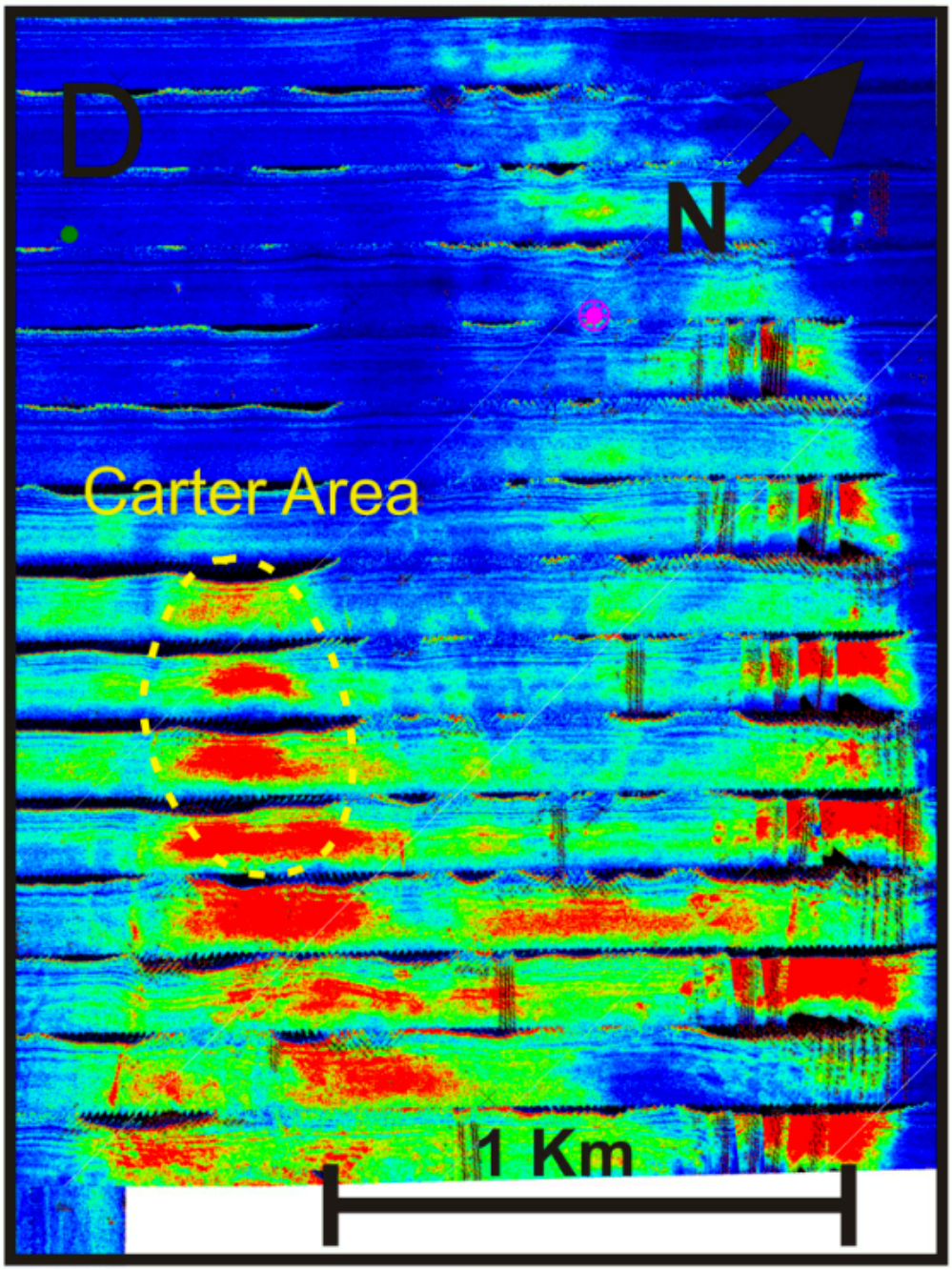

Figure 4.28 Backscatter image of Ridge Crest Crater

Reflectivity measurements at Ridge Crest Crater, reflective highs (red to white) are apparent at the summit of the ridge, and the highs are maintained moving northwest downslope. Location of figure shown in Figure 4.16. Authigenic carbonate is known to be present at the ridge summit from ROV observations (Figure 4.7). The dashed yellow line outlines the location of the crater area.

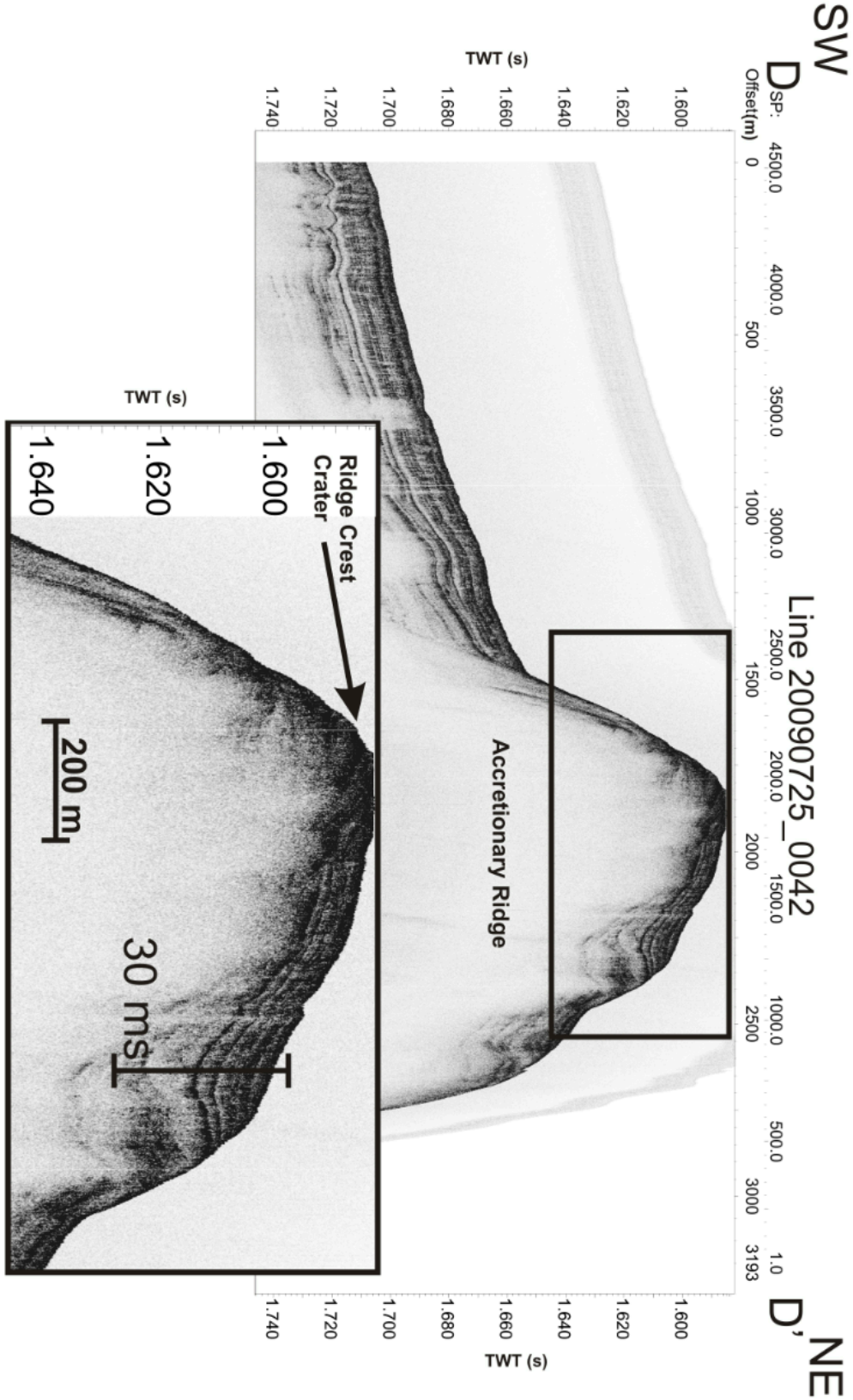

Figure 4.29 Sub-bottom profiler across Ridge Crest Crater

Figure 4.29 (previous page): AUV profile D-D′ through Ridge Crest Crater by AUV line 20090725_0042. Ridge Crest Crater shows no internal reflections at its summit, northeast of the summit between shot points 1000 and 2000 stacked strata is visible to a maximum depth of 30 ms TWT, ~22 m (bottom box). Northeast and southwest of the ridge slopes are steep and sub-bottom profiling is unable to record any potential sedimentary structure. Between shot points 2400 and 4500 sedimentary layers present in the slope basin rise upwards towards the accretionary ridge. The eastern limit of the slope basin is visible truncating against the slope of Ridge Crest Crater (shot point 2400).

4.3.5 Bullseye Vent

Named initially for its circular appearance in 3D seismic time-slice data (Riedel et al., 2002), Bullseye Vent is in fact an elongate structure with pockmark-type topography, as revealed for the first time by this AUV survey. Bullseye Vent is isolated within the slope basin between the two regional topographic highs. The location of the vent is shown in Figure 4.14(E) and the 3D bathymetry is shown in Figure 4.30; the vent is a 350 m long scar on the seafloor trending southwest to northeast with an azimuth of 44°. On the northwest and southeast sides of the vent, topography rises by 4 m above the surrounding seafloor towards the lip of the feature. The vent depression has topographic relief of 3-5 m and is described as a "scar-feature", a term used by Paull et al. 2009. A minor bathymetry high exists southwest and northeast of the vent site (<1m - 1m), and parallel to the strike of the vent. The minor bathymetry changes northeast of Bullseye Vent gradually bend towards the north approaching the base of Ridge Crest Crater.

Backscatter reflectivity values at Bullseye Vent are higher than the surrounding seafloor (within about 1000 m). Figure 4.31 shows Bullseye Vent's enhanced seafloor reflectivity (greens to reds) against the surrounding seafloor (blue). Seafloor ROV observations place authigenic carbonate at the seafloor within Bullseye Vent (Figure 4.8). Along strike to the northeast away from Bullseye Vent, a regional trend of backscatter highs extend towards Bubbly Gulch and north towards Ridge Crest Crater. These reflectivity trends are coincident with minor changes in bathymetry previously mentioned.

Sub-bottom profiler data is visible in Figure 4.32 for Bullseye Vent. As this vent has been previously identified by seismic as a conspicuous feature (Riedel et al., 2002) on the seafloor, multiple cross lines were obtained parallel to the vent strike. This was done to constrain the subsurface structure of the vent site more accurately. In profiler data perpendicular to vent strike (Figure 4.32), the vent site is apparent due to a loss of seismic penetration between shot points 2400 and 2700. Seismic penetration is at its best in the seafloor sediments surrounding Bullseye Vent (near 60 ms), and seismic penetration is lost in the area of the vent. Approaching the vent form the northwest, sedimentary horizons are horizontal, and at the lip of the vent (shot point 2750) beds are no longer imaged. This loss of recording is potentially due the higher slopes approaching the vent, which are a maximum of 3°. On the east beds dip more steeply beneath the lip than farther east, and, sub-seafloor penetration is lost progressively from shotpoints 2300 to shotpoint 2550. Figure 4.33 shows profiler data directly across the vent in the strike direction. Sedimentary strata in this area have a regional down-dip to the southwest. The vent lies between shot points 1100 and 1700. Similar to the vent-perpendicular line,

seismic penetration is lost at the vent site. To the southwest, beds dip away from the vent. To the northeast, bed dips are horizontal and begin to dip northeast at shot point 1800.

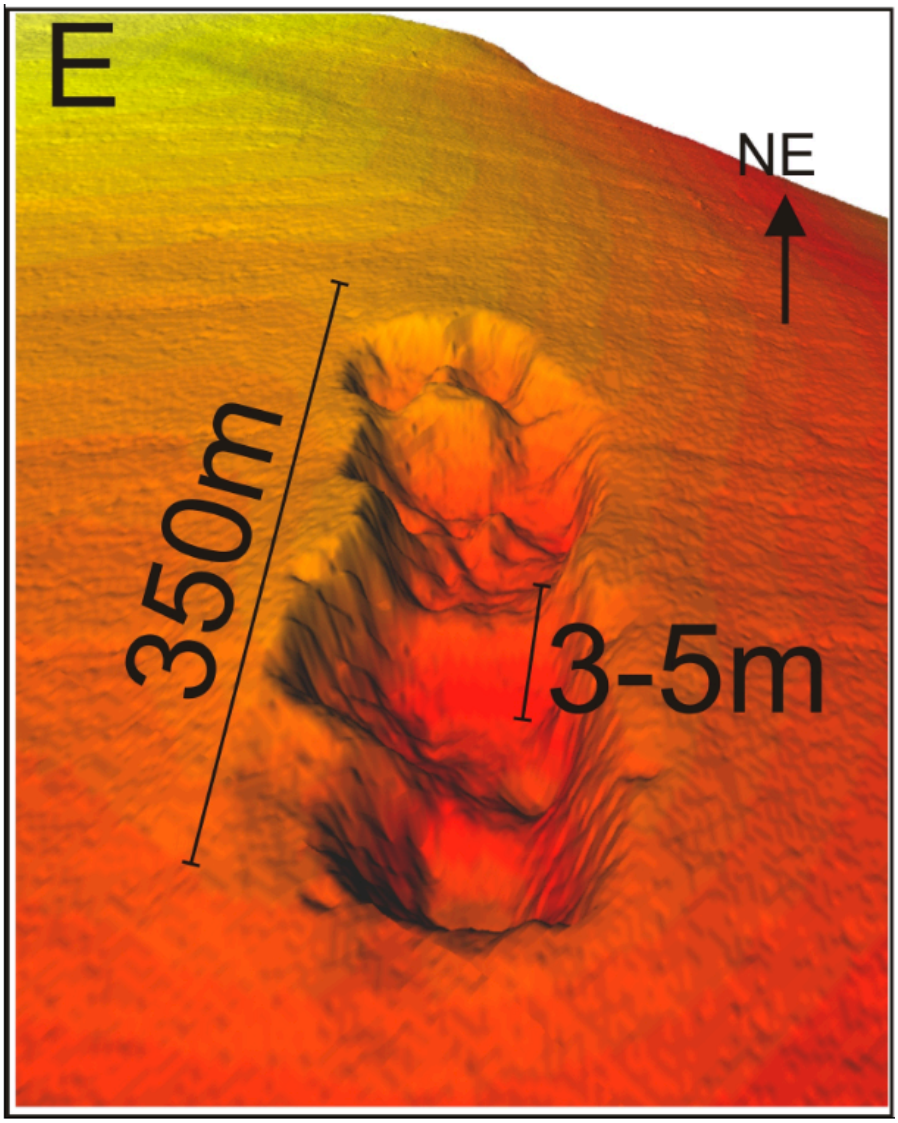

Figure 4.30 3D perspective of Bullseye Vent

The vent is a 350 m long scar on the seafloor trending southwest to northeast with an azimuth of 44°. Approaching the vent topographic rises by 4 m above surrounding seafloor towards the lip of the feature. Directly past the lip the vent drops into a bowl with 3-5 m topographic relief.

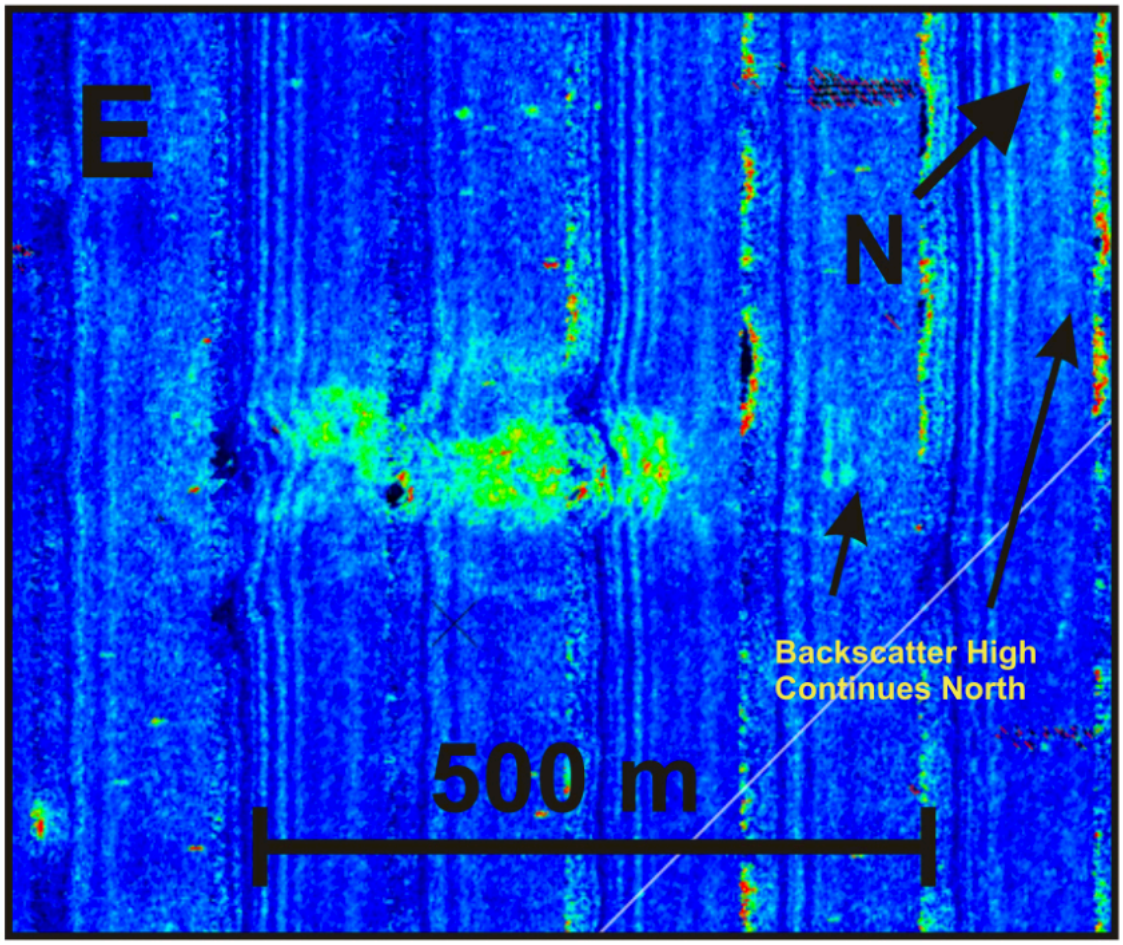

Figure 4.31 Backscatter Image Of Bullseye Vent

Reflectivity measurements at Bullseye Vent, Bullseye Vent's enhanced reflectivity values are represented by green to red color against the surrounding seafloor reflectivity of low backscatter (blue color). Location of figure shown in Figure 4.16. Seafloor ROV observations place authigenic carbonate at the seafloor surrounding Bullseye Vent (Figure 4.8).

Figure 4.32 (following page) Sub-bottom profiler through Bullseye Vent, perpendicular to vent axis: AUV profile E-E´ perpendicular to Bullseye Vent line 20090723_0027. The vent site is located between shot points 2400 and 2700 where seismic penetration is lost. Northwest of the vent, sedimentary horizons are horizontal, and at the lip of the vent (shot point 2750) beds are no longer imaged. Southeast of the vent, beds dip slightly away from the vent. Penetration is lost progressively between shot points 2300 and 2550.

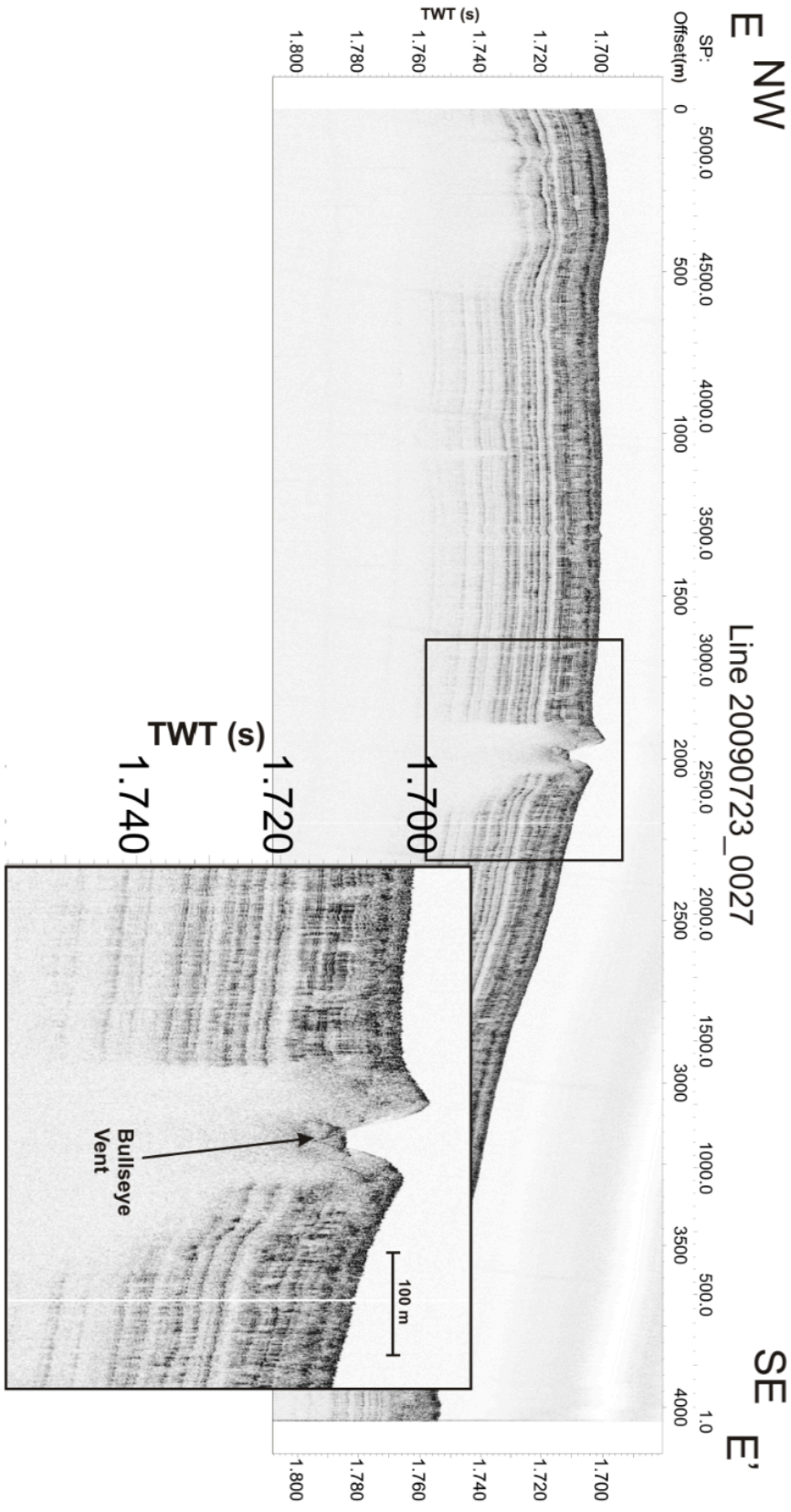

Figure 4.32 Sub-bottom profiler through Bullseye Vent, perpendicular to vent axis

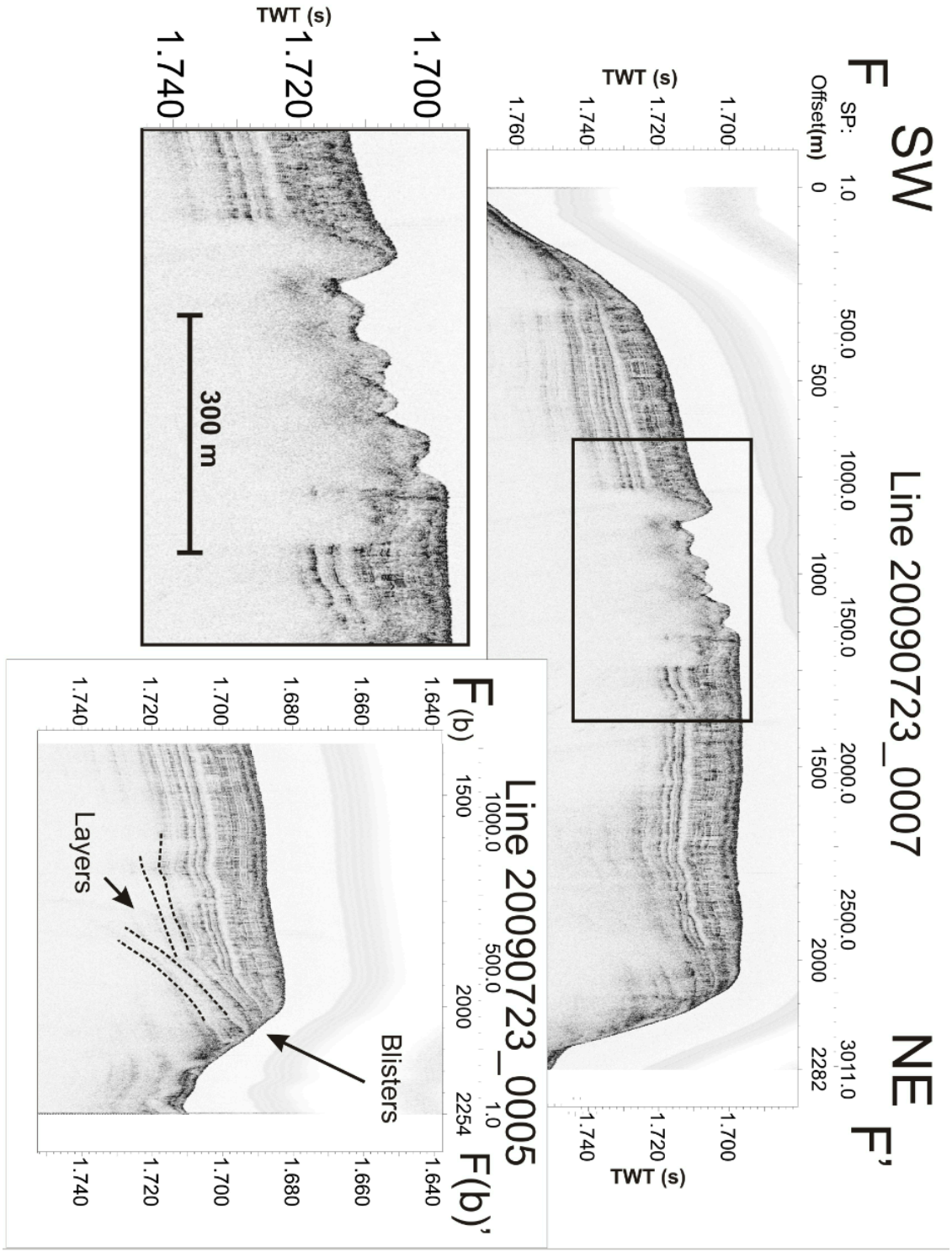

Figure 4.33 Sub-bottom profiles across Bullseye Vent to Bubbly Gulch, parallel to vent axis

Figure 4.33 (previous page) Sub-bottom profiles across Bullseye Vent to Bubbly Gulch, parallel to vent axis: AUV profile F-F′ line 20090723_0007 parallel to Bullseye Vent strike and Near Bubbly Gulch. This line runs directly above the vent scarp and along strike. Sedimentary strata in this area have a regional down dip to the southwest. The vent lies between shot points 1100 and 1700. Approaching from the southwest beds dip upward towards the vent and penetration is lost at shot point 1100. Approaching from the northeast bed dips are horizontal and begin to dip down at shot point 1800. Seismic penetration is lost at shot point 1600. Acoustic imagery near the gulch shows well-stratified layers that dip upwards to the edge of the surveyed area past shot point 2500. The gulch lacks subsurface similarities to other observed venting sites in the survey (e.g. Bullseye Vent just 900 m southwest) characterized in profiler data by a loss of acoustic signal. Supplemental profile F_b-F_b′ shows the dipping strata that breaches the surface at the gulch. The horizontal migration of fluids in this area may be the cause for just aggressive venting visible at the gulch. In this area seafloor cracks, blisters, and methane degassing is commonly visible at the seafloor (Figure 4.9).

4.3.6 Bubbly Gulch

Bubbly Gulch lies 900 m northeast of Bullseye Vent along the same strike as the vent axis. It was previously recognized as a gas venting site by the occurrence of gas plumes observed in ship-mounted echo-sounder data. This site, investigated by ROV in 2009 (Figure 4.9), is named for the intensive venting associated with small seafloor mounds that, when penetrated by a coring device, vigorously degassed (Paull et al., 2009). Due to the intensity of methane degassing present at this site, a report was completed prior to the 2009 dive for the Environmental Protection Safety Panel (EPSP) of IODP. The gulch lacks similar characteristics to other vent sites in the area, such as changes in bathymetry, seafloor reflectivity, or subsurface structure measured by the sub-bottom profiler. Figure 4.17 shows the location of the gulch on the northeastern edge of the AUV survey. As mentioned in the EPSP report, much of the degassing at the gulch may be due to the horizontal migration of fluids and gasses (possibly buoyancy driven)

though the regional strata that have a shallow dip of 0.9° towards the west. The extent to which the gulch is fed by horizontally migrating fluids versus vertically migrating fluids is undetermined. The gulch is interpreted to arise as the result of recent slumping at the edge of the slope basin. Outside the survey area just northeast of the gulch, the seafloor elevation drops by 100 m over roughly 500 m. ROV inspections of the slumped and eroded area show "blisters" at the seafloor (less than 0.5 m in height). These seafloor blisters show surface cracks associated with active gas bubbling, and they are covered with bacterial mats (Figure 4.9).

High acoustic backscatter values are associated with Bubbly Gulch (Figure 4.35). A yellow line in the backscatter plot outlines a north-to-south trend in the reflectivity. A broad region of moderate reflectivity is found in the south, while very high reflectivity values occur to the north in a narrow band with a length of nearly 500 m.

Sub-bottom profiler data for Bubbly Gulch (Figure 4.33), along profiles F-F′ and F_b-F_b′ (locations in Figure 4.17), show well-stratified layers that generally dip to the southwest. Strata breach the surface at the northeast end of the profiles, where the seafloor is eroded at the gulch.

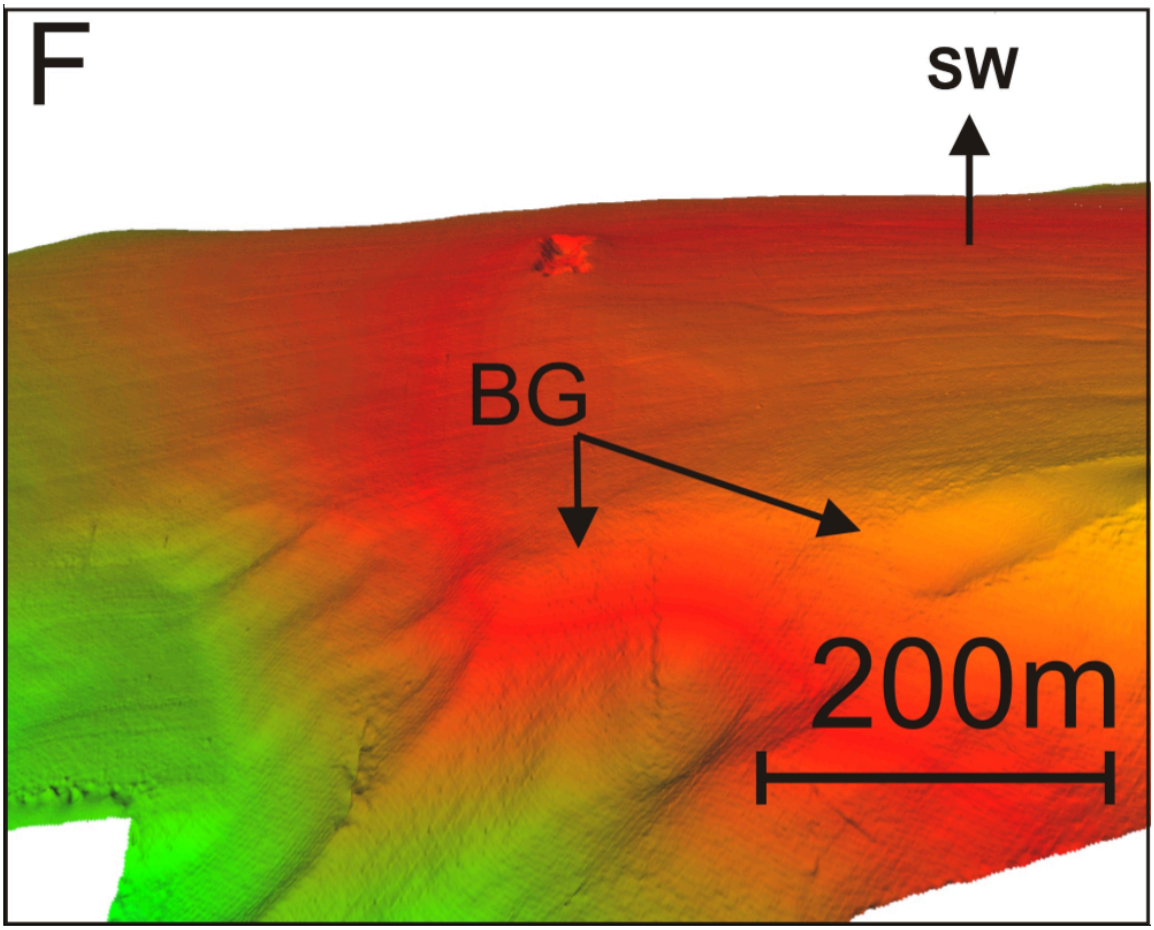

Figure 4.34 3D perspective of Bubbly Gulch

The gulch lacks similar characteristics distinguished by AUV recordings at other vent sites such as changes in bathymetry, seafloor reflectivity, or subsurface structure measured by the sub bottom profiler. Outside the survey area just northeast of the gulch the seafloor elevation drops by 100 m over roughly 500 m. The gulch lies 900 m northeast of along the same strike of Bullseye Vent seen in the distance.

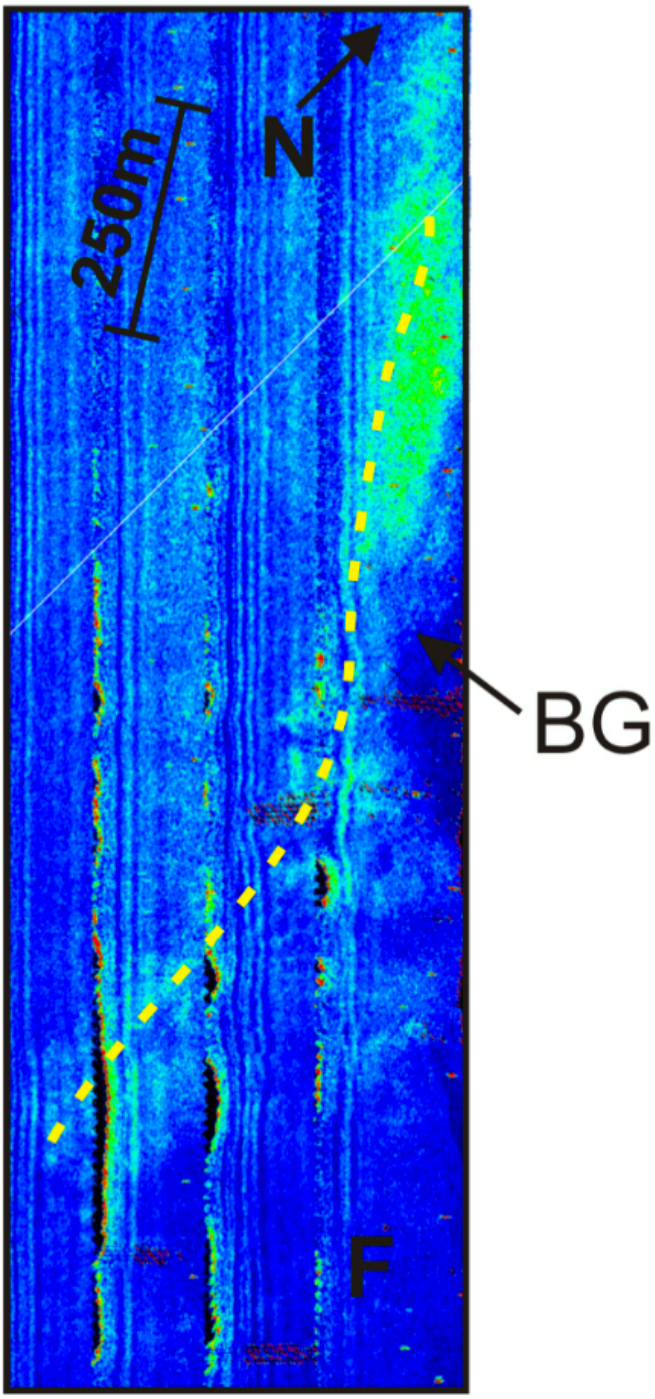

Figure 4.35 Backscatter image of Bubbly Gulch

Reflectivity measurements at Bubbly Gulch, a yellow line in the backscatter outlines a reflective north to south trend. Location of figure shown in Figure 4.16. This area of high seafloor reflectivity originates in the south (light green colors) and progresses north as the reflectivity becomes more intense over the kilometer.

5 Discussion and Interpretation

In this chapter I discuss visible surface features of cold vents and attempt to explain what mechanisms exist in the subsurface to generate these features. Backscatter recordings are examined qualitatively for the acoustic signature of cold vents, and how they differ throughout this study area. Sub-bottom profiler seismic recordings illuminate the near-surface structure of the top 40 m of sediments. Multichannel seismic data image well past the depth of the BSR which forms the lower limit of the hydrate stability field. Other seismic methods (DTAGS) are better at resolving shallower depths, yet still are limited in the very near surface. AUV sub-bottom profiler data help bridge that gap by imaging the very near surface (5 - 50 ms TWT), and at a higher resolution than surface seismic data. For mapping the occurrence of cold vent systems, shallow imaging is crucial, since small surface features (venting sites, carbonate mounds, CBCs, pockmarks, etc) are revealed only by near-seafloor sonars, high-resolution bathymetry, and ROV observations. Shallow AUV sub-bottom imaging allows the examination of discrete cold vent communities to be extended into the subsurface.

The penetration of the sub-bottom profiler data varies throughout the study area. A limiting factor for the profiler data interpretation arises from the amount of acoustic signal loss, or acoustic “blanking” through the study area. AUV lines show multiple zones of acoustic signal loss, and two distinct occurrences are identified: (1) regional (extending of many hundreds of meters to kilometres) seismic blanking, often with diffuse vertical boundaries at the edges, and (2) localized (few hundred meters) seismic blanking, often sharply truncated. Figure 5.1 shows the spatial extent of the different

styles of acoustic blanking recorded with the sub-bottom profiler. Finally, this chapter discusses possible fluid migration pathways from structural relationships visible on sub bottom profiler data. Faults and folds present in the areas are displayed in Figure 5.1 as well as the locations of AUV track lines discussed in this chapter.

5.1 Regional Blanking

Widespread acoustic attenuation of seismic energy is apparent over an area of nearly 6 km^2, as shown in the blue outline in Figure 5.1. The area is marked by an absence of signal at depths greater than 6-7 mbsf (~10 ms TWT). AUV line 20090724_0027 (location in Figure 5.1) shows an example of the prevalence and extent of widespread blanking observed in the AUV data. Line 20090724_0035 (Figure 5.2) corresponds to profile A-A´. Southwest of shotpoint 2400 and northeast of shotpoint 4150, beds are imaged dipping downwards towards the northeast. Between these shotpoints, it is not expected that these beds should change their thickness or lithology, so their seismic signature should still be visible. The seismic response of these beds is not recorded and two explanations for this loss in seismic penetration are presented in Sections 5.1.1 and 5.1.2.

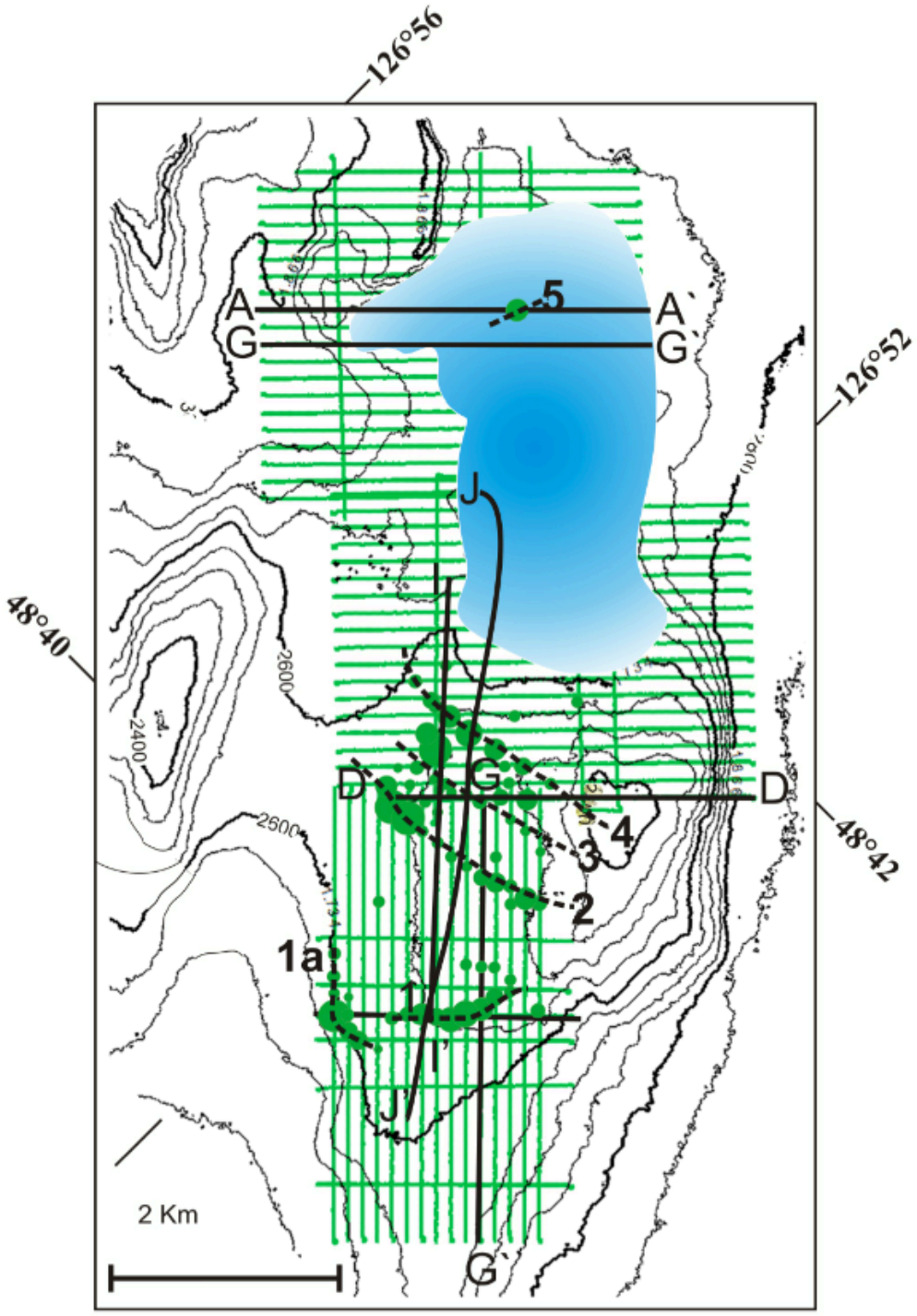

Figure 5.1 Extent of regional and localized blanking on the grid of AUV lines

AUV lines (green) are shown overlaying regional bathymetry. The blue area shows the extent of regional blanking, and green circles show the zones of localized blanking. Letters and numbers show AUV lines through the blanking zones and the individual blanking trends respectively. Venting trends are shown by dashed black lines and are numbered 1-5.

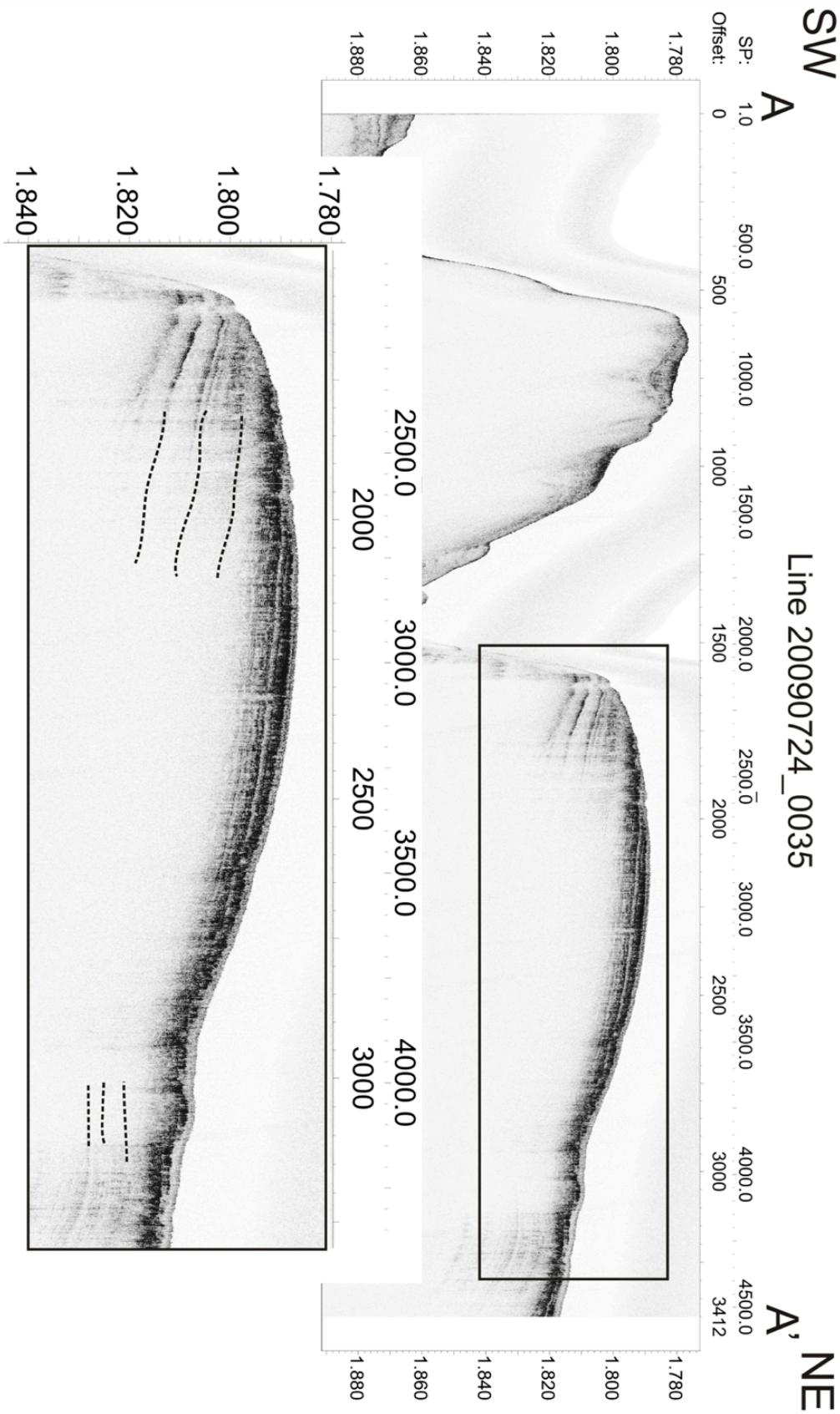

Figure 5.2 Profiler line A-A' showing regional blanking northeast of Cucumber Ridge

Figure 5.2 (previous page) Profiler line A-A' showing regional blanking northeast of Cucumber Ridge: AUV line 20090724_0035 showing regional blanking through the area. Location of profile line seen in Figure 5.1. Dark patches are present in the near surface suggesting above average impedance of near surface sediments. Between shotpoints 2400 and 4150 beds are imaged dipping downwards into the area of regional blanking. Assuming these beds do not change in thickness or lithology moving northeast, their seismic signature should still be visible. Dashed black lines indicate expected bed location where data is not available.

5.1.1 Cause of widespread blanking: Occurrence of free gas?

The attenuation of seismic energy is commonly attributed to free gas in many geological environments, and this has previously been used to explain blanking at Bullseye Vent (e.g. Zuehlsdorff et al., 2004). In this study area, the role of free gas must be interpreted in conjunction with the extent of potential gas hydrate stability. Free gas can occur below the BSR marking the deepest limit of possible gas hydrate stability, but free gas at shallower depths as seen in the acoustic blanking lies well within the theoretical gas hydrate stability zone. First, it could be expected that free gas at this depth would be captured within a solid gas hydrate structure rather than distributed freely through the sediments. For stable hydrate to form, the concentration of methane has to exceed the local solubility of methane in pore waters. For an example temperature-pressure phase diagram of the solubility of methane in marine sediments see Figure 2.8 in Chapter 2. Thus, if free gas were to be the cause of the blanking, one would also expect some occurrence of solid gas hydrate to be co-existing: if methane gas is present in abundance, it would thermodynamically first form gas hydrate. Only if all local water were used for hydrate formation, all remaining excess gas would then occur in the pore space as gas bubbles, resulting in the acoustic blanking. A complicating factor in this

discussion is the fact that the acoustic blanking starts at very shallow depths in the seismic records, almost immediately beneath the seafloor. Thus, the onset of blanking may be located above the SMTZ, i.e. in a zone where no methane is supposedly occurring, it is being consumed by reacting with the downward-diffusing seawater sulfate. Coring and geochemical analyses of pore waters suggest a regional depth of the SMTZ in the study area of 6 - 8 mbsf (Solem et al., 2002; Novosel, 2005; Riedel, 2001). Only in cold vents, the SMTZ is much shallower and may even be at the seafloor (e.g. Pohlman et al., 2003). Just beneath the SMTZ, methane concentration values in the sediment increase, but were not seen to exceed the local solubility threshold until much greater depths (Malinverno et al., 2008; Riedel et al., 2010). The onset of gas hydrate occurrence from the ODP and IODP boreholes suggests a top of gas hydrate occurrence at ~70-80 mbsf at Sites 889 and U1327, which are located within the regional acoustic blanking zone. This relatively deep onset of gas hydrate is equivalent to the depth where the methane concentration has reached and then exceeded the solubility threshold.

Additionally, if free gas were present and stable (i.e. not captured as solid hydrate) throughout this zone, simple buoyancy would likely result in migration upwards, either along dipping beds or the otherwise highly porous near-surface sediments. If this migration were occurring, frequent venting sites would be visible at the seafloor, especially just east of Cucumber Ridge, based on the mapping of regional bed dip seen at the edges of the acoustic blanking zone. Example dipping beds that intersect the seafloor are visible between shot points 2100 and 2300 in Figure 5.2. However, no venting has ever been recorded in shipboard echo sounding profiles, despite extensive coverage of the study area in several cruises since the mid-1990s. Also, the seafloor morphology defined

from the AUV data does not show any signs of typical vents (e.g. as seen at Spinnaker Vent or Snake Vent). Thus, it can be concluded that free gas can be ruled out as a cause for the presence of the widespread blanking in the AUV sub-bottom profiler data.

5.1.2 Cause of widespread blanking: Transmission losses from "hard" layers?

Two previous investigations have tried to answer the findings of increased seafloor reflection coefficients over widespread regions on the slope (Fink and Spence, 1999; Riedel, 2001), but were limited to seismic data with a surface towed streamer and airgun and lower seismic frequencies (< 120 Hz). Both approaches previously published argued for an increase in seafloor reflectivity from the presence of harder substrate. However, none of these studies encountered reduced acoustic transmission throughout this zone of high reflectivity. Fink and Spence (1999) suggested the presence of wide-spread carbonate pavements, whereas Riedel (2001) argued for sand-layers as cause of seafloor hardness. The study by Riedel (2001) also included some 3.5 kHz sub bottom profiler data, but the data were acquired using a hull-mounted transducer, thus limiting its lateral and vertical resolution. However, an apparent decrease in penetration depth over the zone of increased sediment reflection coefficients had already been noticed, but the new the AUV sub-bottom profiler backscatter data provide improved clarity.

Theoretically, higher reflection coefficients (above ~0.4) present in near-surface sediment may limit the penetration of acoustic energy into the subsurface due to simple transmission losses. The hardness of a lithological unit and its ability to reflect acoustic energy is determined by the unit's impedance (the product of the unit's acoustic velocity

and its density). Table 5.1 shows density, velocity, impedance, and calculated reflection coefficients for hemipalegic muds, sands, and authigenic carbonate. Reflection coefficients for the three different units are calculated for the seabed by Equation 5.1, where I_1 is the impedance of the top unit (water) and I_2 is the impedance of the lower unit (lithology). In all cases the top unit is water with a density of 1030 Kg/m^3 and with an acoustic velocity of 1485 m/s.

Equation 5.1:

(Reflection Coefficient) $$\mathbf{RC = (I_2 - I_1)/ (I_2 + I_1)}$$

Table 5.1

Marine Physical Properties & Reflectivity Coefficients

Sediments	Density	Velocity	Impedance	Reflection Coefficient with Water
Hemipalegic	1500-1600 Kg m^{-3}	1480 m/s	2.2-2.4 x 10^6 Kg m^{-2} s^{-1}	0.15-0.34
Sands (Core 1554)	2100 Kg m^{-3}	1700-1760 m/s	3.6-3.7 x 10^6 Kg m^{-2} s^{-1}	0.41-0.43
Carbonate	3000 Kg m^{-3}	3000-4000 m/s	9-12 x 10^6 Kg m^{-2} s^{-1}	0.7-0.8
Water	1030 Kg m-3	1485 m/s		

Table 5.1: Physical properties of marine sediments and calculated reflection coefficients with seawater using a density of 1030 Kg/m^3 an acoustic velocity of 1485 m/s. Density and velocity values for sands are taken from Core R1554, hemipelagic sediments values are from Johnson and Helferty (1990) and authigenic carbonate values are from Fink and Spence (1999).

The AUV backscatter recordings and sub-bottom profiler data provide another insight into the spatial variations in seafloor hardness throughout the study area. Additionally, the higher resolution of the AUV data offers additional insight into the mechanism for blanking and high seafloor reflectivity. As previously discussed in Chapter 4, Figure 4.15 and Figure 4.16 show the variations in seafloor acoustic response measured through this study area by the AUV. The highest values in this study area are present at and near the summits of Cucumber Ridge and Ridge Crest Crater (coloured red). For a backscatter comparison, a single channel seismic study was completed by Fink and Spence (1999) over the northern flank of Ridge Crest Crater and their zone of high reflectivity is shown in Figure 5.3. The red dot shows the location of ODP Hole 889B and the green dot shows the location of Push-Core R1554 (Figure 3.17) from this study. The reflection coefficients recorded in the study by Fink and Spence (1999) range from 0.1 to 0.5. Most of these higher reflection coefficients are concentrated near ODP drill hole 889B and surround the summit of the Ridge Crest Crater topographic high. Reflection amplitudes were corrected for spherical divergence to measure the reflective coefficients of the seafloor quantitatively. The maximum reflection coefficients of 0.4-0.5 are located in the same area as Push-Core R1554 (black dot, Figure 5.3). Losses in reflection strength could occur from a defocusing of acoustic energy due to the topographic high; over the ridge itself, reflection coefficients are 0.35-0.4 and slightly lower than in the area 1-2 km northwest and downslope of the ridge. Further east, down the east flank of Ridge Crest Crater, are reflective lows of 0.15.

The reflection strength mapped by Fink and Spence (Figure 5.3) does not correspond to the same reflection highs mapped by the AUV. This is not unexpected as

the frequencies are vastly different between the two studies. Fink and Spence suggested a 2 m-thick carbonate layer as the source of high reflectivity based on the amplitude character and synthetic seismogram modelling of 75 Hz data.

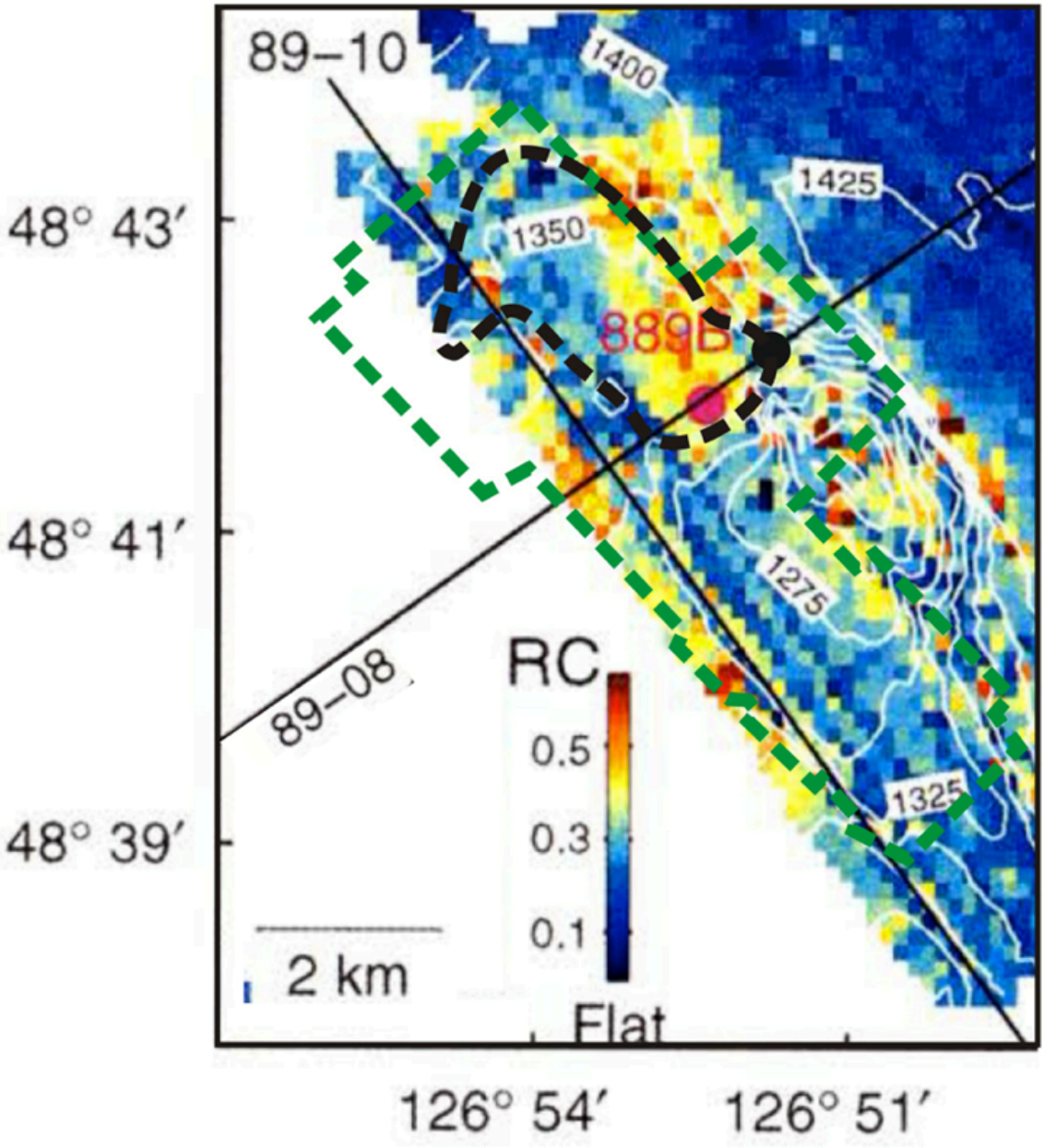

Figure 5.3 Reflectivity values as calculated by Fink and Spence (1993)

Figure 5.3 (previous page) Reflectivity values as calculated by Fink and Spence (1993)
The ratios between multiple/primary amplitudes over the flat slope basin to the northeast were used to determine the flat scale. The reflection coefficients measured are in more agreement with sands measured from core R1554 than with seafloor carbonate (figure edited from Fink and Spence, 1999). The red dot shows ODP drill hole 889, and the black dot shows push core R1554. The dashed green polygon outlines they AUV survey area and the dashed black line outlines the area of regional blanking.

The area of regional seismic blanking extends from the central Cucumber Ridge towards the base of Ridge Crest Crater. Slope basin sediments are filled with stacked turbidite sections, as suggested by Westbrook (1994) and confirmed through cores taken in the region (e.g. ODP Leg 146 Site 889, IODP Expedition 311 Site U1327, and the Push-Core taken for this study near Ridge Crest Crater by ROPOS). The seismic velocities associated with the sands seen in the Push-Core (Table 5.1) are roughly 1750 m/s and densities are above 2.0 kg/m^3. The expected reflection coefficients for sands recovered from this study area are thus between 0.41 and 0.43. While these reflection coefficients are not as high as those of carbonate, the "stacked" sand packets of turbidite could account for high transmission losses in seismic energy at shallow depths. The acoustic blanking is observed only in the high-frequency sub-bottom profiler data and 3.5 kHz data, but not in the low-frequency airgun data. Since the sand layers are only a few centimetres each in thickness, only the high-frequency data can resolve such thin layers. Thus, the high-frequency data are more sensitive to consecutive transmission losses at each layer boundary. With a velocity of 1500 m/s and a frequency range of 2-16 kHz, the shortest possible wavelength is 10 cm. Thus, one quarter of a wavelength (limit of resolution) is ~2.5 cm. For the 75 Hz airgun data, wavelengths are in the order of 10 m

near the seafloor (resolution ~2.5 m) and thus no finer detail is resolved that affects the transmission loss.

In combination, the lack of visual proof of carbonate pavements in the area where the Push-Core was taken, and the recovery of a sand-rich lithology in the Push-Core and in one regional piston core (Novosel, 2003; Riedel, 2001), suggest that the regional blanking and high seafloor reflectivity are due to an unusual sand-occurrence rather than the presence of carbonate (which further would require some form of methane-rich environment such as that seen at the vent sites). Figure 5.4 shows a seafloor image recorded during the collection of the push core R1554 during the 2012 Neptune dive. During the approach to the drill site, and after, hard pavements of authigenic carbonate were not encountered. However, the absence of carbonate cannot be certain without percent $CaCO_3$ values and $\delta^{13}C$ measurements from the sediment.

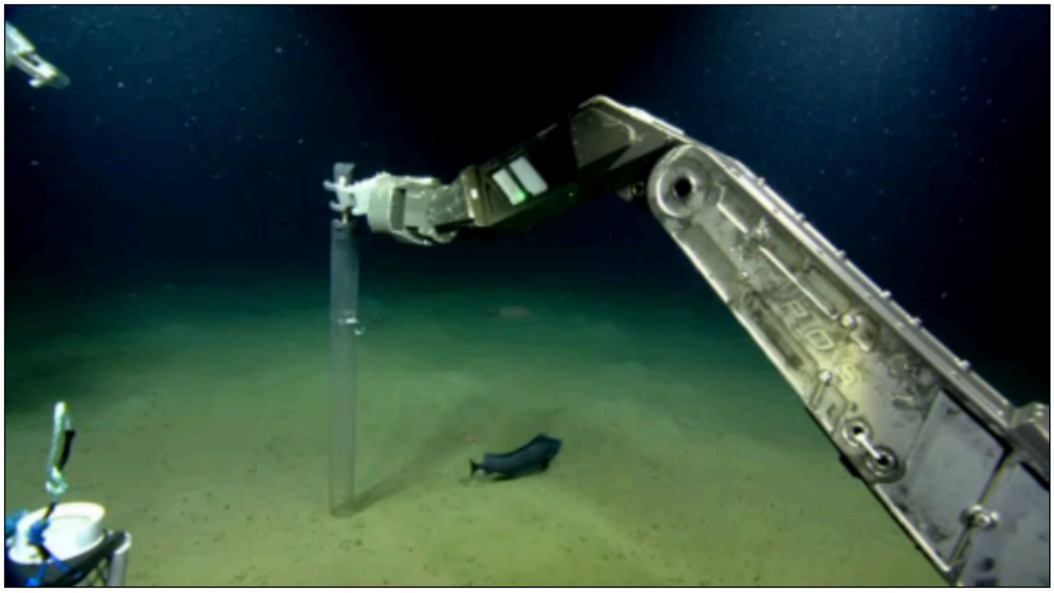

Figure 5.4 Core R1554 seafloor screen capture

NEPTUNE's ROV ROPOS collects core R1554 from the seafloor north of the eastern ridge (see yellow dote Figure 4.1, or green dot Figure 5.3). Before and after the collection of the core, no visual presence was recorded in the region.

5.2 Localized Blanking

Unlike widespread attenuation in sub-bottom profiler recordings discussed in Section 5.1, localized blanking is present intermittently throughout the study area. Localized seismic attenuation is a commonly observed feature in regions experiencing a history of active fluid venting (e.g. Bullseye Vent). Riedel et al. (2002) has already reported on the presence of acoustic blanking in this study area through the use of single channel and high-resolution hull-mounted 3.5 kHz seismic data. Additional investigations on the blanking of vents using the DTGAS system were made by Wood et al. (2002) and He et al., (2009). Although DTAGS data already improved vertical resolution and imaging "sharpness" of the vents by the higher frequency content (up to 1 kHz) and smaller Fresnel zone, the data require rather complex processing, somewhat limiting their use and lateral resolution capability. Also the exact location of the line acquired is uncertain, as the deep-towed streamer is poorly located laterally and vertically (for more detail see He et al., 2009 and He, 2007). Thus, the AUV data are improving our understanding of the nature of the vertical blanking zones as they are accurately located and acquired close to the seafloor (~50 m) with a very small Fresnel zone (~3 m).

Figure 5.5 shows a profile northwest to southeast through the center of the study area showing several typical examples of the vertical blank zones. The cause for seismic attenuation in these areas is not fully understood (e.g. compare discussions in Riedel et al., 2002; Zuehlsdorff et al., 2004; Riedel et al., 2006); possible causes of attenuation include free gas and heterogeneity within the sediment column from the presence of

hydrate and/or authigenic carbonate. Since these zones of blanking are linked with semi-vertical fluid and gas migration pathways, they are generally called “vent chimneys” throughout the literature (e.g. Stoian et al., 2008). These migration channels visible through sub-bottom profiler recordings are variable in width and height in the sediment column. Mapping the presence of the vent chimneys outlines venting trends in the subsurface. These trends are expressed in Figure 5.1 by green dots. However, as already noted previously (e.g. Riedel, 2001), some of these "chimneys" only appear to be vertical because of the extreme vertical exaggeration used in displaying seismic profiler images. They often are rather wider than tall and, when plotted at a 1:1 scale, resemble the shape of a disk or hockey puck (personal communication, Roy Hyndman).

In the following, spatial trends in the vertical blank zones are discussed, compared to previous findings using airgun data, and re-interpreted. Additional fine-scale details, not previously identified and appreciated in the study area are introduced and discussed.

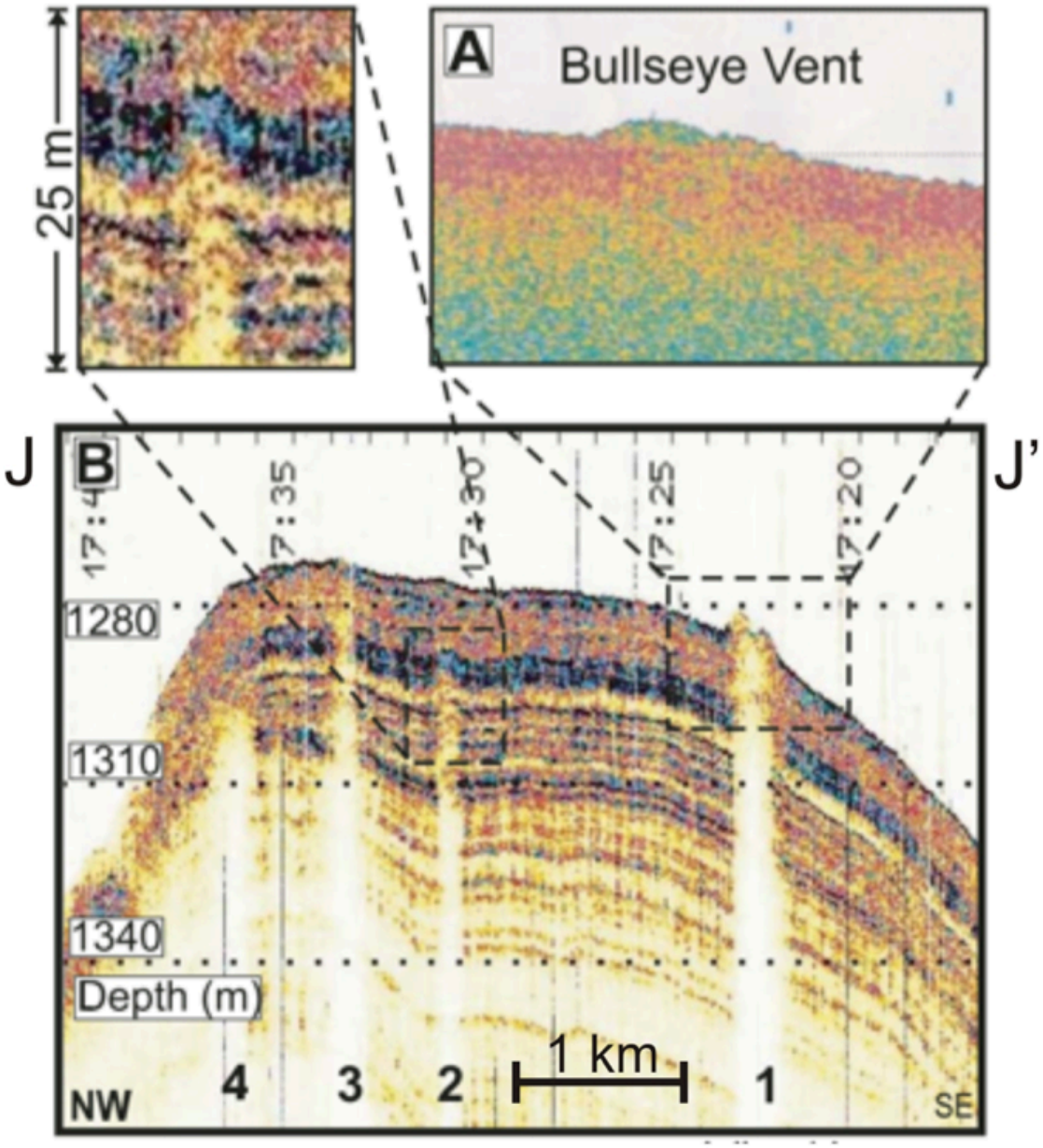

Figure 5.5 Single channel seismic (SCS) Line 27

This seismic line runs northwest to southeast through the center of the study area (Figure 5.3). Vent chimneys 1 and 3 extend from the BSR to the seafloor (Riedel, 2001).

5.2.1 Spatial Trends In Blanking

Acoustic blanking of vent sites with an almost linear E-W trend was previously observed (Riedel et al., 2002) and associated with regional faulting in the study area, but resolution (lateral and vertical) were relatively poor due to the low frequency content of the data. The same area was covered by the AUV which allows a much more detailed delineation of these trends

The circles in Figure 5.1 show the width of the vent sites at the surface under the assumption that sub-bottom profiler lines have intersected the vent at its center. Intersecting cold vent sites at their center is, however, statistically unlikely (or only a total coincidence) so the diameters provided in Figure 5.1 set a lower boundary for the vent diameter. There are five venting trends labeled in Figure 5.1. Venting trend 1 is orientated parallel to the Bullseye Vent depression and trends southwest to northeast (azimuth of 44°.). To the southwest of this Trend 1, there is another venting trend (1a) that may extend west beyond the area covered by the AUV survey. This trend is not well constrained in the subsurface but appears to be unlinked to Bullseye Vent. It should be noted that, coincidentally, the DTAGS line interpreted by He et al. (2009) does show a small vertical blank zone that coincides with the Trend 1a seen in the AUV data.

Venting Trends 2, 3, and 4 are oriented approximately east to west. Venting Trend 5 is associated with Spinnaker Vent. The surface expression of Spinnaker Vent (i.e. occurrences of pockmarks) is orientated roughly southwest to northeast (azimuth of 35°) as shown in Figure 4.21. As previously noted, Spinnaker Vent is difficult to describe from the sub-bottom profiler data, as it exists within the zone of regional acoustic

blanking. In this area acoustic penetration is low, so bedding structure at and surrounding the vent site is not clearly visible. Only some shallow structure is visible in the very near surface of Spinnaker Vent, for ~10 ms TWT or 7-8 m.

5.2.2 Structure of individual Cold Vent Sites

Cold vents vary in size and shape throughout the study area. This section will describe the most prominent vents present and consider subsurface structural features potentially responsible for fluid and gas migration initiating vent-outlet formations at the seafloor. Sites investigated are (1) Spinnaker Vent, (2) Snake Vent, (3) Ridge Crest Crater, and (4) Bullseye Vent. For a general description of all regional features including morphology and location see Chapter 4. Bubbly Gulch is not discussed in this section since the sub-bottom profiler data do not show any blanking or other distinguishing characteristics of the subsurface structure.

(1) Spinnaker Vent

The sub-seafloor structure of Spinnaker Vent is the most difficult to resolve in all of the study area using only the AUV data. The vent is located between shot points 2500-3500 of AUV line 20090724_0031 (Figure 4.23). The site is clearly constrained by distinct bathymetric features showing small surface pockmarks, 1-3 m deep (Figure 4.21). The sub bottom profiler imaging of Spinnaker Vent shows little penetration depth and the subsurface features remain poorly resolved. Bedding at Spinnaker Vent though appears slightly offset vertically by a fault (Riedel et al., 2010) running roughly south to north

and extending north beyond the AUV surveyed area (Figure 4.17). The seafloor and shallow sedimentary beds rise towards the surface approaching Spinnaker Vent. In Figure 4.23 beds to the south of Spinnaker Vent (left of vent) are slightly elevated compared to the north (right of vent). Offset of the beds is a maximum of 4 meters and suggests a northern hanging wall. Confidence in offset measurement and inferred hanging wall are low due to the lack of penetration through the area. A more complete view of the faulting around Spinnaker Vent was provided in Riedel et al., (2010) using multi-channel and single-channel airgun data, as well as 3.5 kHz Huntec data clearly linking the surface expression of Spinnaker Vent to a larger deep-rooted growth-fault system. Notably, the surface expression of pockmarks and carbonate outcrops associated with Spinnaker Vent trend at ~35°, whereas the underlying fault as imaged in the airgun seismic data as defined by Riedel et al. (2010) and seen as subtle ridge on the AUV bathymetry trends at ~25°, an approximate 10° difference.

(2) Snake Vent

Snake Vent area is associated with a small topographic high in the center of the survey area (Figure 4.7, Figure 4.24). The pockmarked surface of this vent field has a relief similar to that of Spinnaker Vent (1-3 m). The cold vent lies on the hanging wall of a normal fault trending northeast to southwest through the region. Line 20090725_0010 (Figure 4.26) shows Snake Vent and its associated fault between shot points 3000-4000. Just 200 meters directly southeast and 650 meters southwest of Snake Vent lie two more structural highs. These sites are not fault related like Snake Vent but the result of an anticline (Figure 4.17).

(3) Ridge Crest Crater

Ridge Crest Crater is part of the eastern topographic high (accretionary ridge), which is the highest region surveyed in this study and is characterized by large slabs of authigenic carbonate upwards of 6 meters thickness. The crater-zone that was surveyed with the ROV in 2009 (hence the regions name) is an area of ~0.02 km^2. Line 20090725_0042 (Figure 4.29) shows some layering in the sediment column between shot points 2000-1000 at the summit of the ridge. The lack of resolution in this area is a combination of topographic effects, transmission losses from the presence of carbonates, and the homogeneous (non-layered) sediments encountered in accretionary ridges. Ridge Crest Crater has seen a history of venting confirmed by ROV observations at its surface (Figure 4.7). The summit of the ridge is pitted with large carbonate slabs, which would have developed only through a lengthy history of fluid advection.

(4) Bullseye Vent

Bullseye Vent is well constrained through sub-bottom profiler lines. AUV line 20090723_0027 (Figure 4.32, shot points 2500-2700) and perpendicular line 20090723_0007 (Figure 4.33, shot points 1000-1600) show the detailed subsurface structure of Bullseye Vent. The uplift of the beds near the vent is similar to that encountered at Spinnaker Vent but more defined as the penetration of Bullseye Vent is not hindered by transmission losses. As no fault or fold is visible in the near surface on sub-bottom profiler data, the subsurface structure allowing for the formation of Bullseye Vent is uncertain. Riedel (2001) proposed a fault through the area as inferred from

deeper-penetrating seismic profiles. A deeper fault through the area allowing for fluid and gas migration would agree with similar cold vent formation features encountered in the area.

5.3 Patterns In Seafloor Backscatter at Cold Vents

Here, the linkages between high backscatter and CBCs (e.g. clams and tube worms), and gas hydrate are described. Qualitative examination of backscatter values combined with ground truth through ROV observations allows for extrapolation to areas not visualized by a ROV. Figure 5.6 is a replot of the regional AUV backscatter showing areas of interest to be discussed in Section 5.3.

5.3.1 Carbonates

Carbonate is present at venting sites in the study area as large slabs, thin pavements, and disseminated within the host sediment. There are numerous zones of high reflectivity due to the presence of carbonate. (1) Cucumber Ridge in the north is part of a long accretionary ridge system with a prolonged history of fluid venting. (2) Ridge Crest Crater is the other accretionary feature in the area with large accumulations of carbonate at its surface. Anticlinal ridges (i.e. Cucumber Ridge and Ridge Crest Crater) create structural traps for lighter fluids and gases, and the summits of these ridges may be perforated with many small faults allowing for large amounts of fluids to escape from these structures during their development.

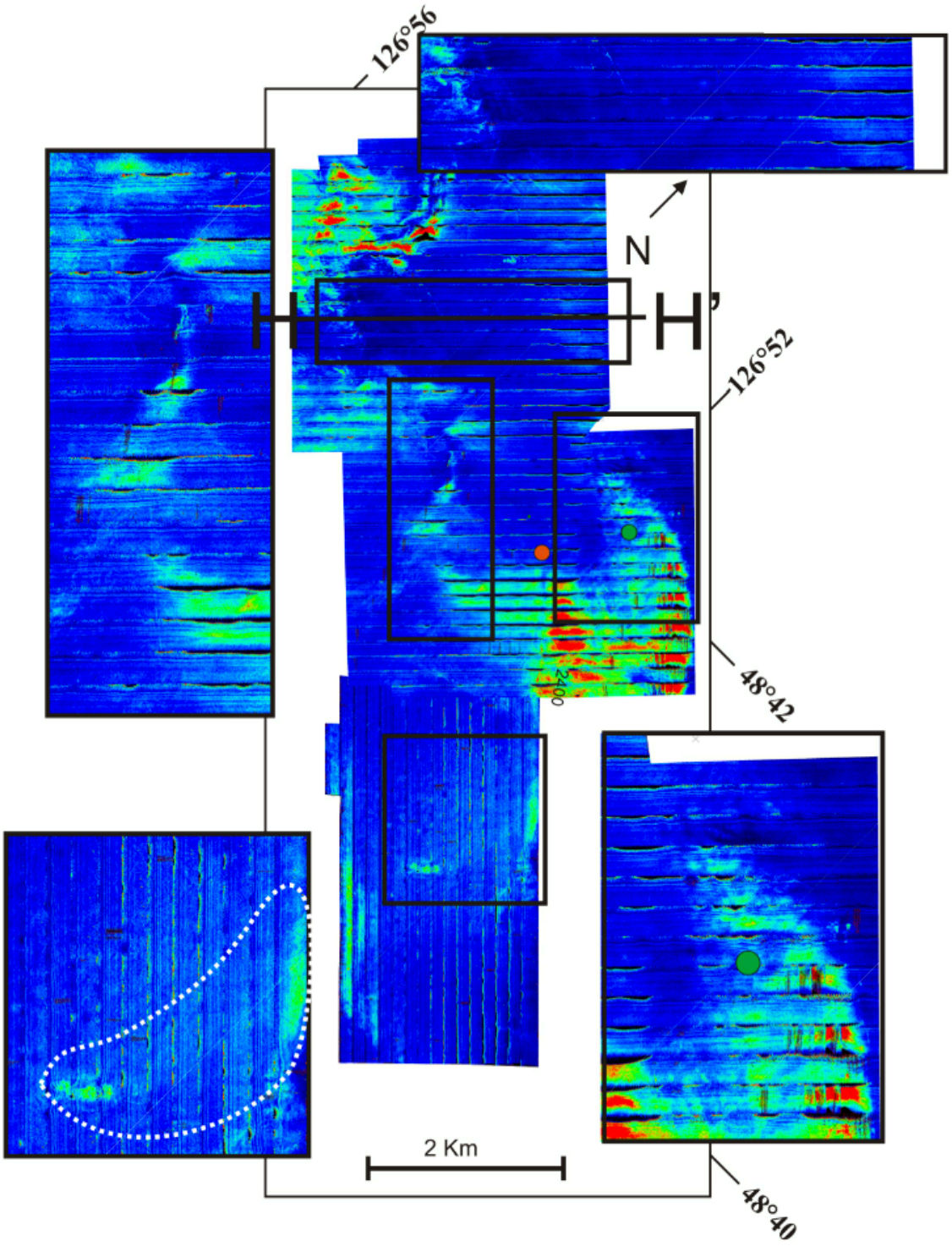

Figure 5.6 AUV backscatter with sites of interest

This figure outlines AUV backscatter sites of interest: (a) Flat surface with changes is backscatter across the basin moving northeast to southwest; (b) Snake Vent backscatter high; (c) Ridge Crest Crater backscatter high; (d) Area northeast of Bullseye Vent backscatter high. A backscatter high

is outlined in the bottom left box by a dashed white line. The green dot shows the location of core R1554.

Bedding planes and fold structures are visible through deeper penetrating seismic data in the area. The rise of the ridges formed the slope basin, and so it is expected that these anticlines would have a longer history of fluid venting that allowed for massive growths of authigenic carbonate compared to the slops basins adjacent. (3) Spinnaker Vent (Figure 4.21 and 4.22) is a much smaller vent feature within slope basin sediments. Authigenic carbonate is present at the surface of the vent as indicated by a reflective high. (4) Bullseye Vent (Figure 4.30, 4.31) has pervasive authigenic carbonate cemented sediments in its base flank. The central zone of the Bullseye Vent depression has low backscatter; here carbonate is not visible at the surface. In the Bullseye Vent depression, coring showed a thick soft sediment cover that was easily penetrated with the vibra-coring system employed by the ROV in 2009 (Paull et al., 2009). (5) Snake Vent (Figure 5.6 b) lies on the hanging wall of the central fault and shows many pockmarks with elevated reflectivity values. Although not investigated by the ROV, these high reflectivity values may also indicate the presence of authigenic carbonate at the surface due to the similarity of the seafloor morphology of other carbonate-rich vent sites.

Intermediate reflectivity values are present to the northeast of Bullseye Vent towards Bubbly Gulch and extend northwards near the base of Ridge Crest Crater shown in Figure 5.6 (d). In the area of these intermediate reflective values, the surface is smooth and unlike the rough topography associated with authigenic carbonate and high reflectivity encountered at other sites. These reflectivity values may be caused by shallow authigenic carbonate produced by diffuse and continuous venting, and simultaneously the

carbonate is covered with a thin layer of hemipelagic sediment. Under these conditions, carbonate deposition would be at a rate less than hemipelagic sedimentation. Alternatively fluid flux may be elevated yet episodic and consequently have the same result. Shallow 50 cm push cores obtained from ROV dives (August 2011) in the area northeast of Bullseye Vent showed small amounts of disseminated authigenic carbonate in the top 30-40 cm. Sediments were examined for dissolved gas content, and so they were not available for a sediment composition analysis.

5.3.2 Chemosynthetic Biological Communities (CBC)

The presence of CBCs through the study is confirmed through visual observations during ROV expeditions. Previous cold vent studies (Orange et al., 2002; Naudts et al., 2008) link the presence of CBCs of tubeworms and bivalves to regions of higher impedance than the surrounding soft seafloor. Spinnaker Vent hosts tubeworms and clams within and surrounding precipitations of authigenic carbonate on the seafloor. Figure 4.22 shows relative reflectivity values at Spinnaker Vent.

In the area northeast of Bullseye Vent (Figure 5.6d), there are laterally variable venting patterns. ROV observations show bacterial mats and clams are common in this area. The presence of abundant chemosynthetic communities is an explanation for the intermediate reflection values encountered through this region. This region of the seafloor is unique because it has not had a rich venting history to build significant depositions of authigenic carbonate. In this region of venting it can be assumed that the reflection values that are higher than the surrounding seafloor are mainly due to the presence of CBCs.

5.4 Pull-up structures and associated gas hydrate at discrete (vertical) vent sites

As previously mentioned, site U1328 (Bullseye Vent) revealed a gas hydrate cap that extended from the surface to ~40 mbsf (Riedel et al., 2010). Controlled-source electromagnetic data also show a large resistivity anomaly at Bullseye Vent and vents linked to Trends 2 - 4 discussed previously (Schwalenberg et al., 2005).

Discrete hydrate accumulations are identified in sub-bottom profiler data by both velocity pull-up structures, and a brightening of reflectors (see Section 2.3.5) above mapped gas chimney occurrences. These areas are expected to host concentrations of hydrate significantly above the average for the region. Localized cold vent sites drilled during IODP Expedition 311 can have concentrations upwards of 80% of pore space (Riedel et al., 2010). Regional concentrations of hydrate are not expected to exceed a 26% (Dash and Spence, 2011).

Blanking trends 2, 3, and 4 show discrete vent structure with vent widths ranging from 50 m to 250 m. Vent chimneys display the bowing of sediment horizons and increases in sediment horizon reflectivity. Both Line 20090725_0042 (Figure 5.7) and Line 20090723_0035 (Figure 5.8) show high impedance reflectors and the bowing of reflectors above localized gas chimneys. The locations of these lines are shown in Figure 4.17. These features are inferred to be caused by the presence of shallow gas hydrate in the sediment column, not unlike that encountered at site U1328 (Bullseye Vent).

Figure 5.7 (page 143): AUV line 20090725_0042 with examples of shallow vent chimneys imaged by the sub bottom profiler. Line locations can be seen in Figure 5.1. At site (A), venting trend 2, sediment horizons bow upwards there is an increase in reflectivity. At site (B), venting trend 3, a vent Chimney connects with the surface and a seafloor cold vent in formed. Hard near surface reflectors are interpreted to be the result of hydrate and the bowing of reflectors to be the result of increases in velocity associated with the infilling of pore space with gas hydrate.

Figure 5.8 (page 144): AUV line 20090723_0035 with more examples of shallow vent chimneys imaged by the sub bottom profiler. Line location can be seen in Figure 5.1. At site (A), venting trend 3, a vent chimney reaches the surface to make a cold vent. At site (B), venting trend 2, there is an increase in reflectivity, and bowing of sediments above a blank zone. Site (C), venting trend 1, is a tight vertical chimney with bowing of sediment and an increase in reflectivity. Site (D), venting trend 1, is a wide blank zone on along the same strike as BEV. Hard near surface reflectors are interpreted to be the result of hydrate and the bowing of reflectors to be the result of increases in velocity associated with the infilling of pore space with gas hydrate.

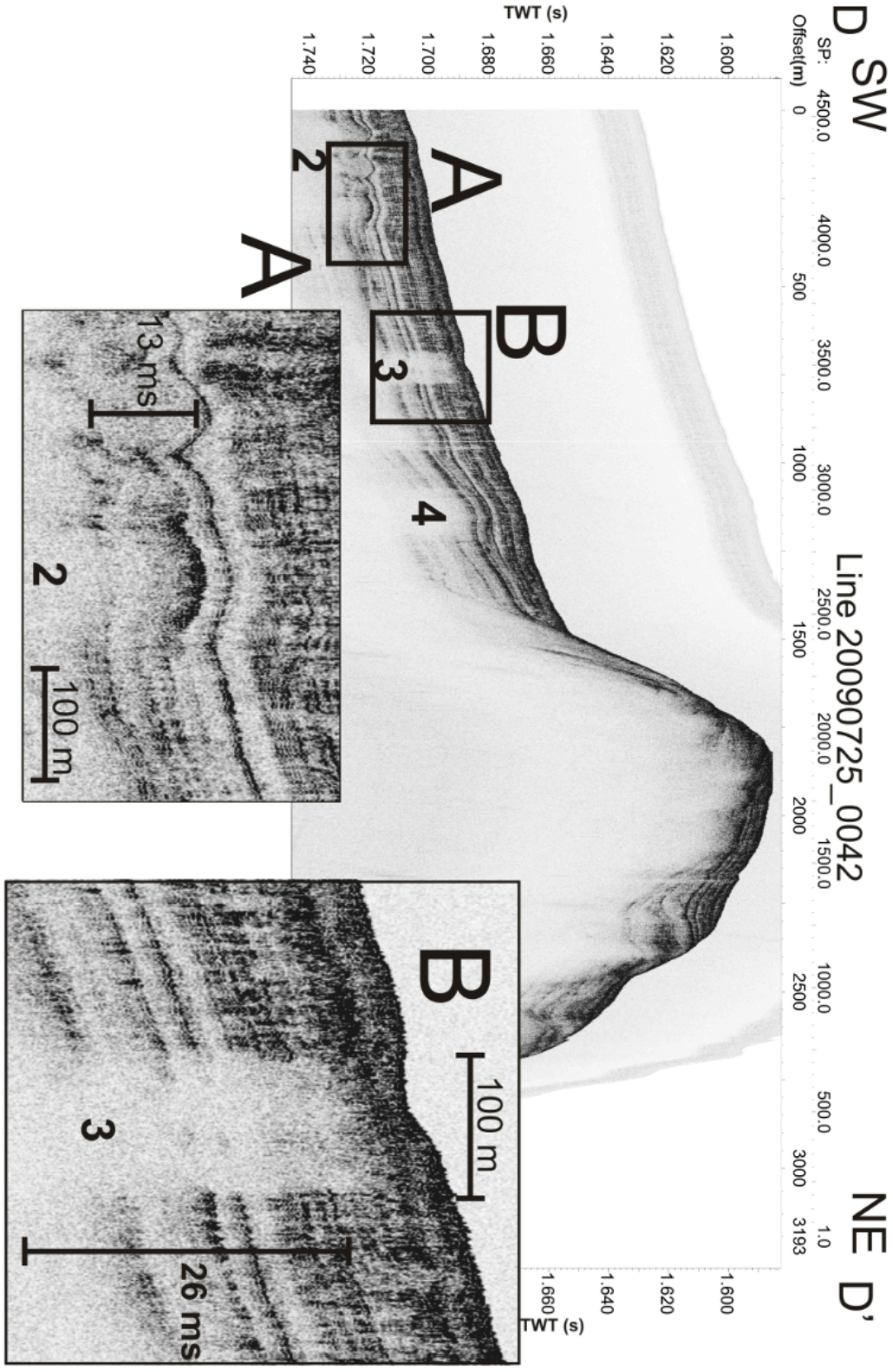

Figure 5.7 AUV Line 20090625_0042, shallow vent chimneys

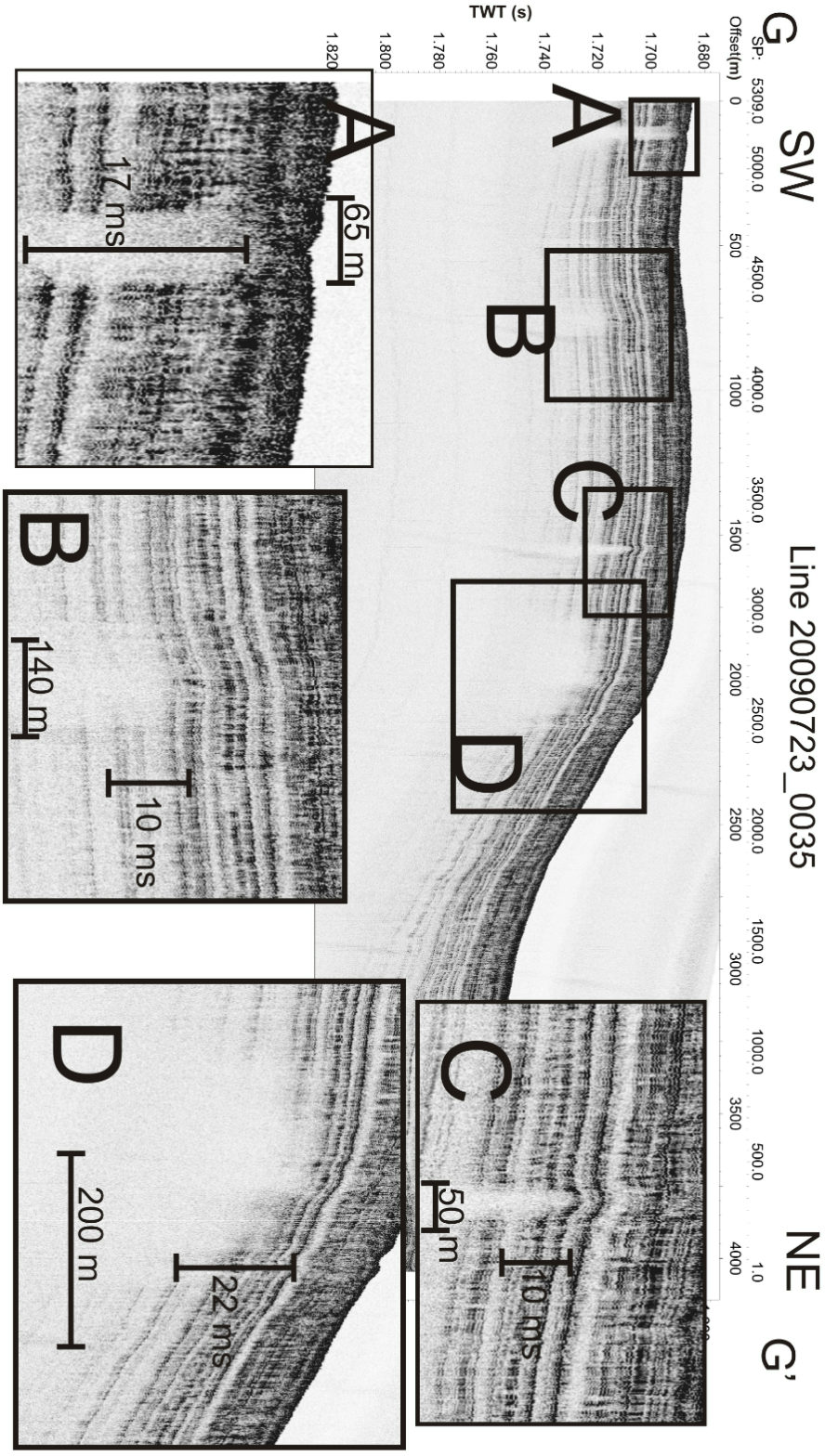

Figure 5.8 AUV Line 20090623_0035, shallow vent chimneys

5.5 Evidence for evolutionary history of venting and related surface and sub-surface geophysical expressions

Localized sites of blanking imaged through the AUV sub bottom profiler exhibit variations in their depth extent. Vent chimneys extend from depth to near the seafloor, and in some circumstances intersect the seafloor. This section will discriminate between the different occurrences of localized blanking encountered in sub-bottom profiler recordings. When chimneys intersect the seafloor to expel their contents into the ocean they are considered cold vents. Vent chimneys that do not reach the surface can be considered as either (1) proto cold vents or (2) extinct vent chimneys. There may be various stages of evolution in between these two end-member scenarios.

Cold vents are identified in sub-bottom profiler recordings by a vent chimney of reduced acoustic reflectivity (blanking) that extends to the seafloor. Venting Trends 2, 3 and 4 also have vent chimneys that breach the surface and create cold vents. These venting sites have a smaller geographic footprint (10-20 meters in diameter) and pockmark relief (0.5-1.0 meter) than larger vents in the study area such as Bullseye Vent or Spinnaker Vent. Line 20090725_0042 in Figure 5.7 shows a vent chimney breaching the seafloor at shot point 3550 (associated with vent 3).

(1) A proto cold vent is a vent chimney that has migrated towards the surface but has not breached the seafloor. This vent may breach the surface in the future if it maintains the necessary gas and fluid pressure. Between shot points 2500-3000 on Line 20090723_0035 (Figure 5.8 D), localized blanking indicates a proto cold vent. (2) An extinct vent chimney is a chimney that is no longer migrating towards the surface. The

proto-vent may have lost its fluid and gas content and now lacks enough pressure to ascend further. As the sub-bottom profiler shows a snapshot in time, it is unclear whether or not these venting features are active or extinct. One possible method of distinction could be through the presence of a high impedance layer at a vent's apex, which may indicate the presence of hydrate within the sediment. Similarly the presence of carbonate would have the same effect, however because these structures are below the depth of the SMTZ it is assumed that these structures are caused from the presence of hydrate. Line 20090723_0035 (Figure 5.8 B and C) and possibly Line 20090725_0042 (Figure 5.7 A) show the presence of a high impendence reflective layer above the vent chimney. As mentioned above in Section 5.4 and Section 2.3.4, the accumulation of gas hydrate within sediment can occur when there is a cap to flow, and the fluid pressure dissipates (i.e. the tap is switched off) causing methane to bubble out of pore fluids. Therefore the presence of hydrate accumulations could be one available distinction to classify extinct gas chimneys from those that may still migrate up further in the future.

One venting type hypothesized in this study area is an episodic vent. This type of vent would have breached the surface in the past and has since lost its fluid and gas support to maintain venting. An episodic vent would be characterized by cold vent evidence at the surface (pockmarks, carbonates, etc.) with a gas hydrate cap and a vent chimney (acoustically blank) below in the subsurface, yet no indication of sustained degassing (bubble-plumes) and/or active chemosynthetic communities. Bullseye Vent is such a type of occurrence of vent.

The end-member of venting history (paleo-vent) are extinct vents where venting activity can be no longer identified. Ridge Crest Crater is an example of a site showing

evidence of paleo-venting; however it lacks any evidence supporting the potential for future venting. At such sites exposed massive carbonate platforms carry the signature of former substantial (and prolonged) methane venting. However, no active chemosynthetic communities are sustained, indicating no methane for the bacterial consortium and symbiosis (that involves H_2S). Coincidentally, these massive carbonate platforms are covered with deep-water corals (Figure 4.7), especially at Ridge Crest Crater and Cucumber Ridge. Corals are known to be sedentary and therefore require nutrient-rich water currents. In areas of abundant deep-water corals growing on massive carbonate platforms, no evidence for typical chemosynthetic communities were found, i.e. no tubeworms and clam-colonies (Calyptogena or Acharax, also known as leather clam) that are indicative of a sulfide-rich environment from the chemical reaction of methane with sulfate. It can therefore be speculated that zones of abundant coral-growth are barren of methane and thus represent extinct cold vents.

As AUV sub bottom profiler data only penetrate the top 40 meters of the sediment column. Figure 5.9 combines SCS line 27 (Figure 5.5) with two AUV lines roughly parallel running northwest to southeast through the basin. Profile I-I´ shows the migration of fluids from BSR depths towards the surface where they are eventually terminate, or reach the surface to form cold vents.

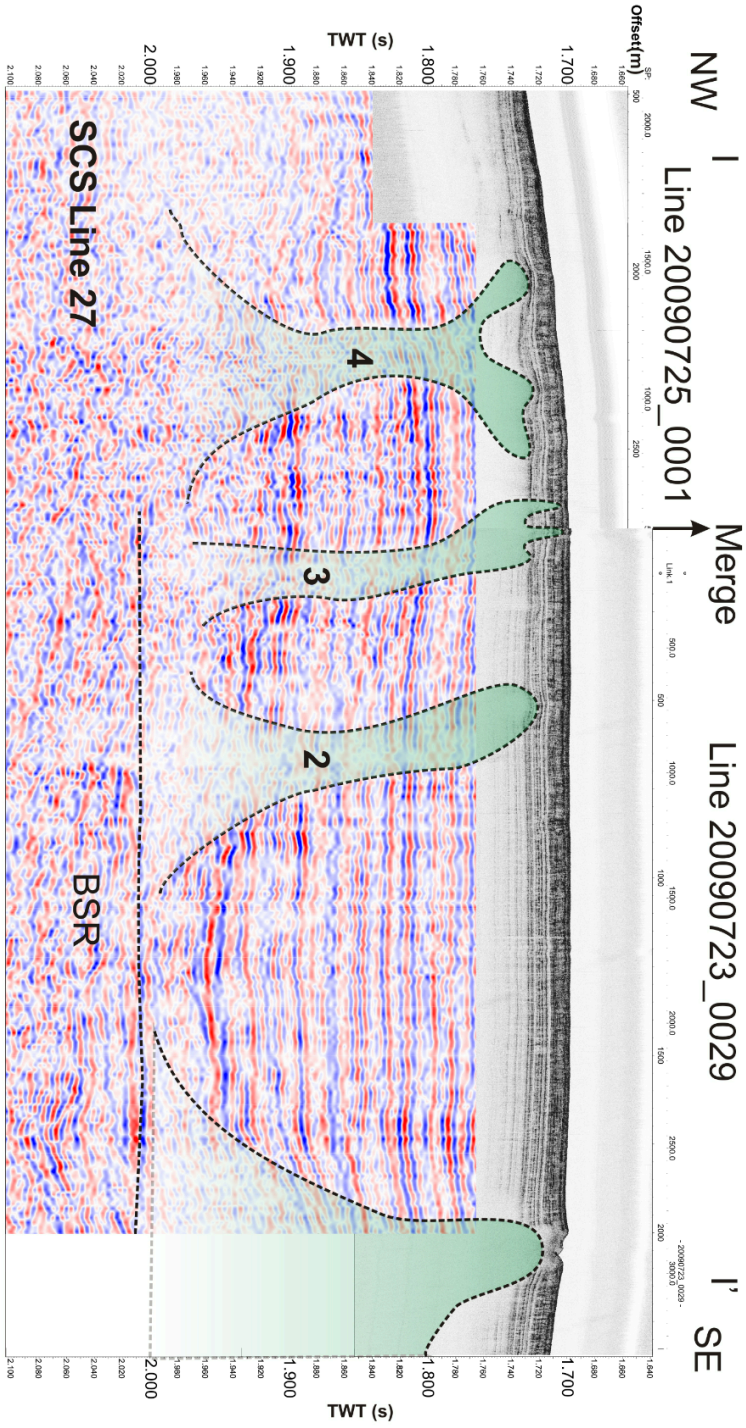

Figure 5.9 AUV with SCS Line 27

AUV line 20090725_0001 and 20090723_0029 combined with line 27 SCS I-I′. Venting trend 1 is the furthest SE at the Bullseye Vent location. Venting trend 4 is the furthest northwest. Venting trends 2 and 3 are in between.

5.6 Evolution of Venting

The expulsion of pore fluids from the accretionary wedge is coincident with dehydration and compaction of the sediment column. Fluid venting across the margin does not exist as a static unvarying process; over-pressures and incipient fluid advection from sediment occur as a response to the changes in accretionary prism environment (i.e. the evolution of the wedge). Temporal changes in prism environment lead to differing stages of fluid venting as discussed in Chapter 2 and summarized by Riedel et al. (2010).

This study provides evidence that discrete sections of the wedge may undergo numerous periods of fluid venting, thus establishing its own venting history. This section will summarize the evolution of fluid venting through the study area by partitioning individual vent sites into one of three stages along the venting lifespan. The stages of fluid venting are classified through the concentration and/or absence of recognized venting related features (e.g. authigenic carbonate, methane degassing, CBCs, seabed morphology). The stages of venting begin with the earliest signs of vent formation and are called “juvenile”. Larger and more established sites are called “intermediate”. Finally, sites of paleo-venting are named “mature”. Table 5.2 lists the different stages in venting evolution and the characteristics absent or present at each venting sites used in their classification.

Table 5.2

Venting Evolution Characteristics

	Juvenile	**Intermediate**	**Mature**
Methane	Active CH4 release	Little or absent CH4 release	No CH4 release
Carbonate	Disseminated CaCO3 through sediments	Laterally extensive CaCO3 pavements	CaCO3 slabs 1-5 meters high in reference to seafloor
Hydrate	Potentially present below the surface	Often present and interbeded within carbonate layers	Not present at the surface, potentially present beneath the surface
CBCs	Extensive bacterial mats and clams	Clams and tube worms attached to carbonate	Coral
Morphology	Blisters, Pockmarks often <1-2m	Pockmarks 1-5 meters	Large carbonate slabs, sometimes > 5m
Backscatter	Mild backscatter response	Medium to high backscatter response	Largest backscatter response

5.6.1 Juvenile

The onset of fluid venting is recognized at the seafloor through methane bubble plumes exiting the seafloor sediment to rise and expand within the water column. These sites are easily recognized in ROV sonar recordings, and long recognized through ship sonar recordings. Bubbly Gulch is the foremost example of juvenile venting through this study area. ROV dives through the region northeast of Bullseye Vent observe the flat seafloor with ample CBCs. The seafloor is covered in white and yellow bacterial mats with intermittent clams scouring the seafloor. These mats expand over 1 km^2 of the study area as inferred from backscatter responses (Figure 5.6 D and Figure 4.35) and seafloor observations. Figure 5.10 is an illustration showing juvenile venting and the associated subsurface features (i.e. vent chimneys and potentially subsurface hydrate). The key characteristic defining these vents as "juvenile" is their lack of accumulation of authigenic carbonate, a common development at other venting sites. ROV push cores collected in the area show small amounts of disseminated authigenic carbonate in the shallow sediment. It is possible that these juvenile venting sites will never see the development of sizeable deposits of carbonate that are present at "intermediate" and "mature" sites. The lack of carbonate may be due to a higher sedimentation rate than carbonate development at the seafloor. This is unlikely however as sub-bottom profiler penetration is high in this region and no anomalously high amplitude reflectors are visible in the subsurface. More likely, the lack of carbonate is due to the intermittent methane supply as seen in sub-bottom profiler data as discussed in Section 5.4 and 5.5.

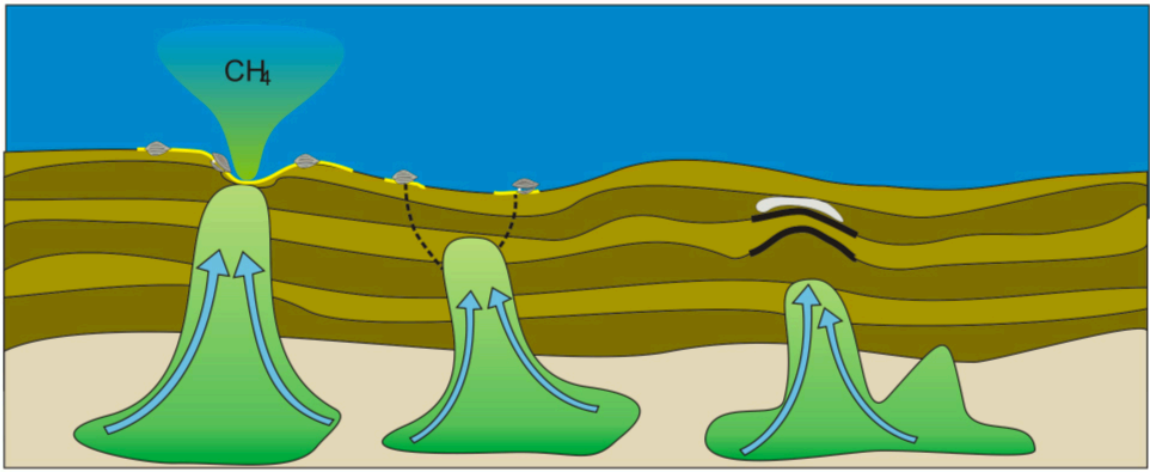

Figure 5.10 Illustration of Juvenile Venting

This illustration was created to represent many of the Juvenile venting features associated with venting trends 2, 3, and 4. Proto cold vents (middle), dead cold vents (right), and active cold vents are depicted (left). Bacterial mats and clams are present at the surface.

5.6.2 Intermediate

Intermediate venting sites are distinguished by the presence of seafloor authigenic carbonate, visible accumulations of gas hydrate at or near the surface, CBCs, pock marks, and often methane venting. Bullseye Vent (Figures 4.31-4.33), Spinnaker Vent (Figures 4.21-4.23) and potentially Snake Vent (Figures 4.25-4.27) are examples of intermediate venting sites. Unlike juvenile vents, intermediate vents have experienced a richer history of venting. This history allowed for large deposits of authigenic carbonates in the form of pavements to develop. This spatial extent of authigenic carbonate pavements is best viewed at Bullseye Vent. Figure 5.11 shows an illustration for intermediate fluid venting depicting large pockmarks and a variety of CBC life and hydrate formation. For accumulations of authigenic carbonate to develop, fluid advection rates must have persisted over time. Structure-related migration pathways allowing for the development

of these sites were first proposed by Riedel (2001). Bullseye Vent, Spinnaker Vent, and Snake Vent are all interpreted to occur on fault-related structures as discussed in Section 5.2.2. Due to accumulations of authigenic carbonate, intermediate venting locations are most easily detected through their topographic signature and acoustic backscatter. A key defining feature of intermediate venting is the lack of sub bottom profiler seismic penetration. As discussed in Section 5.1 and 5.2, the reason for this loss of acoustic signal is unclear but may be due to an increase in heterogeneity, free gas, gas hydrate, or authigenic carbonate. It is worth mentioning that seismic penetration varies quite significantly between Bullseye Vent, Spinnaker Vent, and Snake Vent. Snake Vent has the deepest penetration recorded at any of the intermediate venting sites, but lacks the surface expressions of equal scale as Spinnaker Vent or Bullseye Vent. It is most likely that the loss of seismic penetration is caused by sediment heterogeneity due to a history of venting and irregular sedimentation.

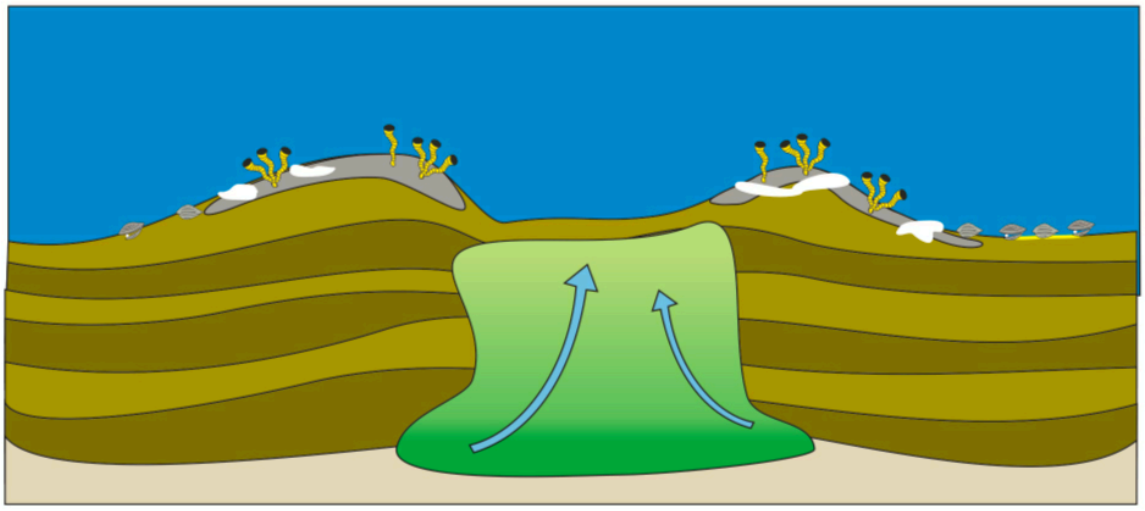

Figure 5.11 Illustration of Intermediate Venting

Figure 5.11 (previous page) Illustration of Intermediate Venting: Illustration of the intermediate stage of venting showing tubeworms, authigenic carbonate (grey), clams, hydrate mixed with carbonate, and a distinctive blank zone. This illustration was created to represent Bullseye Vent. The green blank zone illustrates the possible vertical migration of fluids and gas to the surface.

5.6.3 Mature

Lastly, a mature venting site is denoted by the large accumulations of authigenic carbonate and an absence of any other venting characteristics. Ridge Crest Crater (Figures 4.27-4.29) and Cucumber Ridge (Figure 4.18-4.20) are both examples of mature venting sites, or paleo-venting sites. Both these sites host the largest accumulations of authigenic carbonate seen in the study area, and as such have the highest backscatter responses. Cucumber Ridge and Ridge Crest Crater are the accretionary ridges that rose to create the conditions necessary to form the slope basin of this study area. As the sites are quite old, it is only logical that they would have experienced a much greater history of fluid venting than either Bullseye Vent or Spinnaker Vent. An interesting feature of these paleo sites of venting is the presence of corals which sometimes grow on top of authigenic carbonate. These corals have been determined to live only in quiescent environments and thus further support the perception that these sites of paleo-venting have long been inactive. Figure 5.12 shows an illustration of a mature venting site with large deposits of authigenic carbonate topped by coral. As these ridges initially form from anticlines it is possible that they were in part stratigraphically fed. However, defining these structures as anticlines currently may not be appropriate due to their lack of internal structure. As the ridges ascended much of their internal structure was lost due to vertical

stretching and they are more internally homogeneous than their onlapping slope basin sediments. This homogeneity may have allowed for increases in pervasive fluid advection during formation and allowed for the massive carbonate deposits to form. Finally, due to the convex shape of the ridges they are also naturally more susceptible to increases in fluid advection (He 2007).

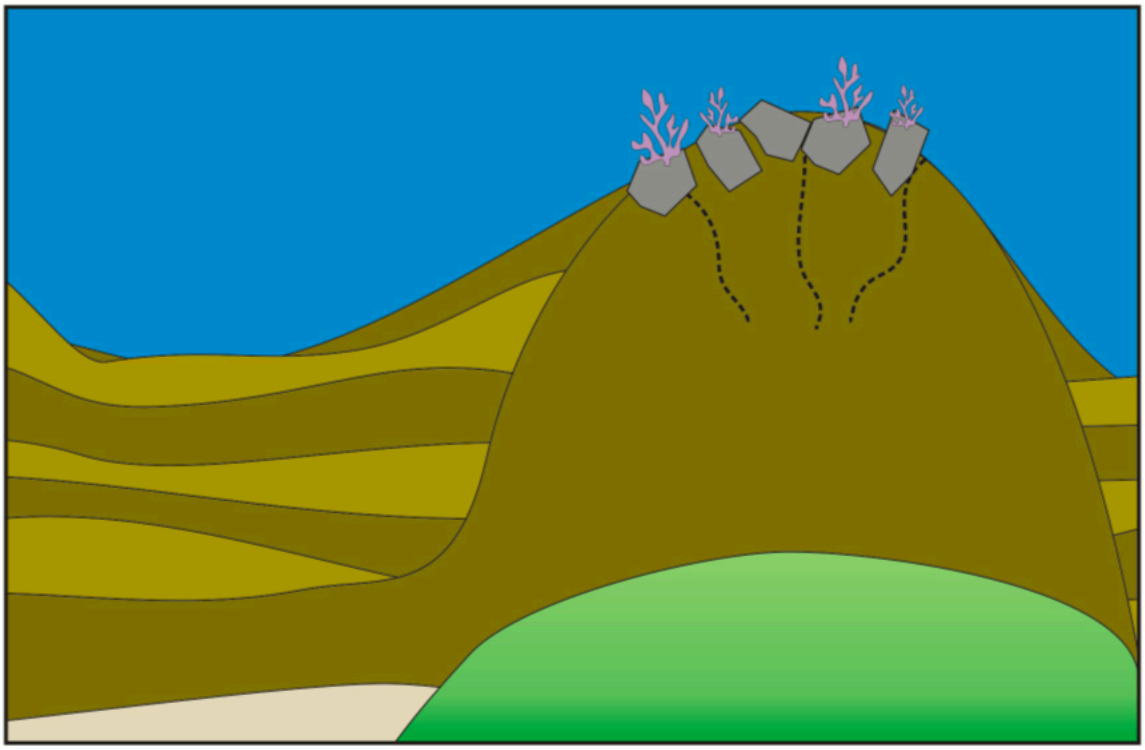

Figure 5.12 Illustration of Mature Cold Vent Site

This cold vent site is modeled after Cucumber Ridge and Ridge Crest Crater. Large slabs of authigenic carbonate (grey) are present at the surface, without any indicator of recent venting. The green zone marks the vertical migration of gas and fluid.

5.7 Can Ocean-Bottom Currents cause anomalous seafloor backscatter highs? A proposed new mechanism

The lowest backscatter values in this area exist just south of Cucumber Ridge. The regional backscatter map (Figure 5.6) shows a gradual decrease in reflectivity from

east to west across the slope basin. Figure 5.6 (a) shows the location of the lowest relative backscatter in the area. AUV line 20090724_0023, profile H-H (Figure 5.13) shows the area of low backscatter for shot points <3000. The low backscatter in this area is most likely caused a large amount of acoustically transparent hemipalegic muds collecting on just one side of the basin. These muds are acoustically transparent in the sub-bottom profiler data. One explanation for the cause of the lateral change in reflectivity moving east to west across the slope basin is the presence of ocean bottom currents. Sedimentary debris removed from the northeast side could migrate over the topographic high of the slope basin. Moving sediments over this structural high may cause heavier sediments (sands) to be left behind and lighter muddy sediments to collect on the opposite side of the basin. The result is a gradual thickening of the mud packet as you move east to west across the slope basin. Figure 6.4 shows an illustration of gradual change in acoustic backscatter. This anomalous zone of sedimentation is most likely the cause of the regional blanking and transmission losses previously discussed.

Figure 5.13(following page) Bottom current affects on backscatter intensity

Line 20090724_0023 geographic location is shown in Figure 5.6 (a). Bottom currents in the region are differentially transporting sediments. Muds are removed from the northeast (shot points > 3000) leaving sands with higher reflectivity. Progressing southwest across the line (shot points < 3000), a thin veneer of mud gradually thickens towards Cucumber Ridge.

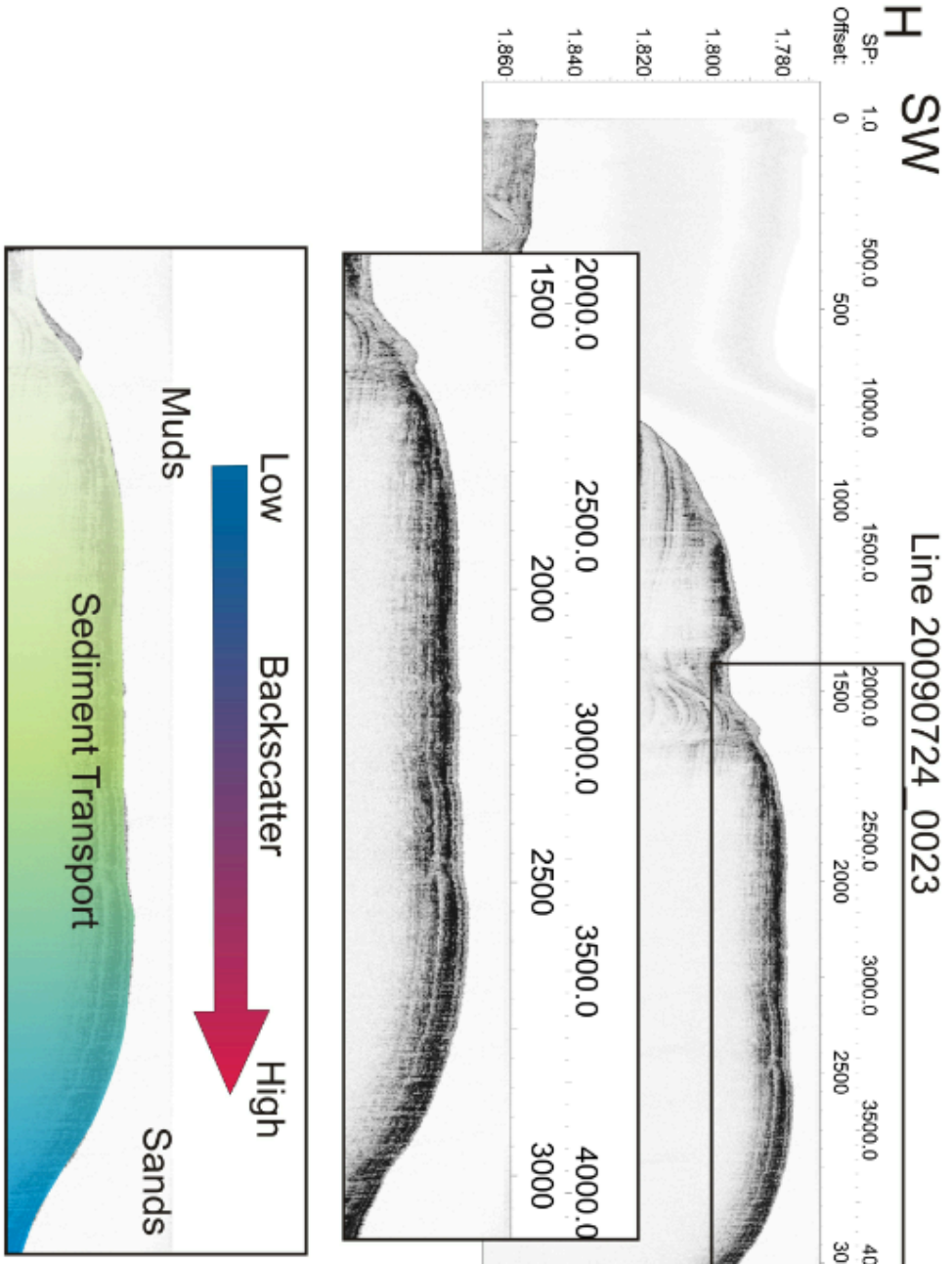

Figure 5.13 Bottom current affects on backscatter intensity

6 Summary and Conclusions

The visual absence of cold-vent-related characteristics (i.e. authigenic carbonate, chemosynthetic biological communities, deep sea corals, gas hydrate) and their morphological and geophysical signatures (i.e. bathymetry and acoustic backscatter) allow for the classification of cold vent communities. The classification scheme places seafloor cold vent occurrences into three separate stages along a path of evolutionary venting. These stages begin with vent inception and high amounts of methane degassing (juvenile), and progress to an intermediate stage, and finally end at a mature stage where these sites lack any evidence of recent fluid advection. This classification scheme could be applied at sea using amplitudes of ship-mounted sonars identify the expected nature of vent sites.

The data presented in this thesis further confirm the utility of the AUV to map the seafloor accurately, and to resolve the geology of near-surface sediments to depths of ~40 m. Shallow faults, with relief of less than a meter, can be resolved in soft sediment at the surface. While bathymetry data may show excellent resolution, backscatter data continue to provide invaluable information about seafloor hardness. The AUV sub bottom profiler echo-sounder penetration depth was not uniform through the study area. It is inferred that due to the high frequency of the AUV signal the unit is especially susceptible to attenuation effects and transmission losses. This conclusion was reached through evidence of near-surface transmission losses in a portion of the survey area that was confirmed to have near-surface stacked turbidite packages with highly reflective sands due to their anomalously high velocity. This evidence was extrapolated to a large region

just east of Cucumber Ridge that experiences a disproportionately low depth of seismic penetration compared to the surrounding area and the majority of the surveyed area. This area is expected to contain larger accumulations of closely stacked turbidite layers with a near surface highly reflective sand package. The conclusion that this near surface higher reflectivity layer is sand is in contrast to previous geophysical work done in the region that has inferred seafloor authigenic carbonate as the source of high reflectivity. The past studies did not have ROPOS coring tools, or high-resolution sonar to distinguish low reflectivity sands or muds.

Methane emission from continental margins occurs mainly as a steady diffuse flow or seepage where most of the leaking methane is not released into the water column but consumed by sulphate reducing bacteria. However at cold vent sites methane release is magnitudes higher (Etiope and Klusman, 2002; Riedel et al, 2010). The AUV data interpreted in this thesis serve as an important database to address the evolution of venting on the northern Cascadia accretionary prism.

Bibliography

Archer, D. E., & Buffett, B. A. (2012). A two-dimensional model of the methane cycle in a sedimentary accretionary wedge. *Biogeosciences*, *9*(8), 3323–3336.

Adams, J., Klaeschen, D., Kukowski, N., & Flueh, E. (2004). Upward delamination of Cascadia Basin sediment infill with landward frontal accretion thrusting caused by rapid glacial age material flux. *Tectonics*, *23*(3), 1-21.

Atwater, T. (1970). Implications of plate tectonics for the Cenozoic tectonic evolution of western North America. *Geological Society of America Bullletin*, 81: 3513-3536.

Alegret, L., & Ortiz, S. (2007). Global extinction event in benthic foraminifera across the Paleocene/Eocene boundary at the Dababiya Stratotype section. *Micropaleontology*, *52*(5), 433–447.

Boles, J., Clark, J., Leifer, I., & Washburn, L. (2001). Temporal variation in natural methane seep rate due to tides, Coal Oil Point area, California. *Journal of Geophysical Research*, *106*(Cll), 27,077–27,086.

Bondevik, S., Mangerud, J., Dawson, S., Dawson, A., & Lohne, Ø. (2005). Evidence for three North Sea tsunamis at the Shetland Islands between 8000 and 1500 years ago. *Quaternary Science Reviews*, *24*(14-15), 1757–1775.

Bryn, P., Berg, K., Forsberg, C. F., Solheim, A., & Kvalstad, T. J. (2005). Explaining the Storegga Slide. *Marine and Petroleum Geology*, *22*(1-2), 11–19.

Buffett, B., & Archer, D. (2004). Global inventory of methane clathrate: sensitivity to changes in the deep ocean. *Earth and Planetary Science Letters*, *227*(3-4), 185–199.

Carson, B., Holmes, M., Umstattd, K., Strasser, J. C., & Johnson, H. P. (1991). Fluid expulsion from the Cascadia accretionary prism: evidence from porosity distribution, direct measurements, and GLORIA imagery. *The Behavior and Influence of Fluids in Subduction Zones* (Vol. 335, pp. 105–114). The Royal Society, London.

Chapman N.R., Gettrust J., Walia R., Hannay D., Spence G.D., Wood W., & Hyndman, R.D. (2002). High resolution deep-towed multichannel seismic survey of deep sea gas hydrates off western Canada. *Geophysics*, 67, 1038-1047.

Claypool, G., & Kvenvolden, K. (1983). Methane and other Hydrocarbon Gases in Marine Sediment. *Annual Review of Earth and Planetary Science*, 299–327.

Collett, T., Johnson, A., Knapp, C., & Boswell, R. (2009). Natural gas hydrates: a review. *Natural gas hydrates—Energy resource potential and associated geologic hazards* (pp. 146–219).

Dallimore, S. R., Wright, J. F., Yamamoto, K., & Bellefleur, G. (2012). Proof of concept for gas hydrate production using the depressurization technique, as established by the JOGMEC / NRCan / Aurora Mallik 2007 – 2008 Gas Hydrate Production Research Well Program. *Geological Survey of Canada*, Bulletin 601, 1–15.

Dash, R., & Spence, G. (2011). P-wave and S-wave velocity structure of northern Cascadia margin gas hydrates. *Geophysical Journal International*, *187*(3), 1363–1377.

Davis, D., Suppe, J., Dahlen, F.A. (1983). Mechanics of fold-and-trust belts and accretionary wedges. *Journal of Geophysical Research*. 88, 1153-1172.

Davis, E., & Hyndman, R. (1989). Accretion and recent deformation of sediments along the northern Cascadia subduction zone. *Geological Society of America Bulletin*, *101*, 1465–1480.

Davis, E.E., and Karsten, J.L. (1986). On the asymmetric distribution of seamounts about the Juan de Fuca ridge: ridgecrest migration over a heterogeneous asthenosphere. *Earth and Planettary Science Letters,* 79, 385-396.

De Beukelaer, S. M., MacDonald, I. R., Guinnasso, N. L., & Murray, J. a. (2003). Distinct side-scan sonar, RADARSAT SAR, and acoustic profiler signatures of gas and oil seeps on the Gulf of Mexico slope. *Geo-Marine Letters*, *23*(3-4), 177–186.

Engebretson, D.C., A. Cox, and G.A. Thompson. (1985). Relative motions between oceanic and continental plates in the Pacific Basin, Speculation Paper. *Geological Society of America*, 196, 59.

Etiope, G., & Klusman, R. W. (2002). Geologic emissions of methane to the atmosphere. *Chemosphere*, *49*(8), 777–89.

Etiope, G., Milkov, A, & Derbyshire, E. (2008). Did geologic emissions of methane play any role in Quaternary climate change? *Global and Planetary Change*, *61*(1-2), 79–88.

Ganguly, N., Spence, G. D., Chapman, N. R., & Hyndman, R. D. (2000). Heat flow variations from bottom simulating reflectors on the Cascadia margin. *Marine Geology*, *164*(1-2), 53–68.

He, T. (2007). *Mound and vent structures associated with gas hydrates offshore Vancouver Island: analysis of single-channel and deep-towed multichannel seismic data*. Retrieved from http://dspace.library.uvic.ca:8080/handle/1828/201

He, T., Spence, G. D., Wood, W. T., Riedel, M., & Hyndman, R. D. (2009). Imaging a hydrate-related cold vent offshore Vancouver Island from deep-towed multichannel seismic data. *Geophysics*, *74*(2), B23–B26.

Haflidason, H., Lien, R., Sejrup, H. P., Forsberg, C. F., & Bryn, P. (2005). The dating and morphometry of the Storegga Slide. *Marine and Petroleum Geology*, *22*(1-2), 123–136.

Hobro, J., Minshull, T., Singh, S., & Chand, S. (2005). A three-dimensional seismic tomographic study of the gas hydrate stability zone, offshore Vancouver Island. *Journal of geophysical Research*, *110*, 1–14.

Hovland, M., Talbot M., Qvale H., Olaussen S., Aasberg L. (1987). Methane-related carbonate cements in pockmarks of the North Sea. *Journal of Sediment Petrology*, 57, 881-892.

Humphreys, E. D., & Coblentz, D. D. (2007). North American dynamics and western US tectonics. *Reviews of Geophysics*, *45*(RG3001), 1–30.

Hyndman, R.D. (1995). The Lithoprobe corridor across the Vancouver Island continental margin: the structural and tectonic consequences of subduction. *Canadian Journal of Earth Sciences*, *32*, 1777–1802.

Hyndman, R. D. (2010). The consequences of Canadian Cordillera thermal regime in recent tectonics and elevation: a review. *Canadian Journal of Earth Sciences*, *47*(5), 621–632.

Hyndman, R.D., Spence G.D., Chapman, R., Riedel, M., & Edwards, R.N. (2001), Geophysical studies of marine gas hydrate in Northern Cascadia. Natural Gas Hydrates: Occurrence Distribution and Detection, Geophysics Monograph Series, vol 124, edited by Paull, C.K. and Dillion, W.P., 273-295, *American Geophysical Union*, Washington D.C.

Hyndman, R.D. & Spence, G.D. (1992). A seismic study of methane hydrate marine bottom simulating reflectors, J.geophys. Res., 97(B5), 6683-6698.

Hyndman, R. D., & Wang, K. (1993). Tectonic sediment thickening, fluid expulsion and thermal regime of subduction zone accretionary prisms: the Cascadia margin off Vancouver Island. *Journal of Geophysical Research*, *98*, 21, 864-876.

Hyndman, R. D., & Wang, K. (1995). The rupture zone of Cascadia great earthquakes from the current deformation and the thermal regime. *Journal of Geophysical Research*, *100*(B11), 22,133–22,154.

Lelieveld, J., Crutzen, P.J., Dentener, F.J. (1998) Changing concentration, lifetime and climate change forcing of atmospheric methane. *Tellus,* 50B 128-150.

Kastner, M., Kvenvolden, K.A., Whiticar, M.J., Camerlenghi, A., & Lorenson, T.d. (1995). Relation between pore fluid chemistry and gas hydrate associated with bottom-simulating reflectors at the Cascadia Margin, edited by B.Carson, G.K. Westbrook, R.J. Musgrave, and E. Suess, *213*, 146, 175-187.

Kennett, J.P, Cannariato, K.G., Hendy, I.L., Behl, R.J. (2003). Methane hydrates in Quaternary climate change. The Clathrate Gun Hypothesis. *American Geophysical Union*, Washington, DC, P.216.

Kennett, J.P, & Scott, L.D. (1991). Abrupt deep-sea warming, palaeoceanographic changes and benthic extinctions at the end of the Palaeocene. *Nature*, 353: 255-229.

Kim, G. Y., Bahk, J. J., Yoo, D. G., & Ryu, B. J. (2012). Physical Property Interpretation Using Log Data from the Ulleung Basin Sediments, East Sea of Korea. *Marine Georesources & Geotechnology*, *30*(3), 195–209.

King, L., & MacLean, B. (1970). Pockmarks on the Scotian shelf. *Geological Society of America Bulletin*, *81*(10), 3141–3148.

Klauda, J. B., & Sandler, S. I. (2005). Global Distribution of Methane Hydrate in Ocean Sediment. *Energy & Fuels*, *19*(2), 459–470.

Krastel, S., Spiess, V., Ivanov, M., Weinrebe, W., Bohrmann, G., Shashkin, P., Heidersdorf, F. (2003). Acoustic investigations of mud volcanoes in the Sorokin Trough, Black Sea. *Geo-Marine Letters*, V23, 230-238.

Kulm, L., Suess, E., Moore, J., & Carson, B. (1986). Oregon Subduction Zone: Venting, Fauna, and Carbonates. *Science*, *231*(4738), 561–566.

Lewis, B., & Cochrane, G. (1990). Relationship Between the Location of Chemosynthetic Benthic Communities and Geologic on the Cascadia Subduction Zone. *Journal of Geophysical Research*, *95*(B6), 8783–8793.

Lopez, C. (2008). *Seismic velocity structure associated with gas hydrate at the frontal ridge of northern Cascadia margin*. Retrieved from http://dspace.library.uvic.ca:8080/handle/1828/2859

Lu, H., Seo, Y., Lee, J., Moudrakovski, I., Ripmeester, J. A., Chapman, N. R., Coffin, R. B., et al. (2007). Complex gas hydrate from the Cascadia margin. *Nature*, *445*(7125), 303–306.

Luff, R., & Wallmann, K. (2003). Fluid flow, methane fluxes, carbonate precipitation and biogeochemical turnover in gas hydrate-bearing sediments at Hydrate Ridge, Cascadia Margin: numerical modeling and mass balances. *Geochimica et Cosmochimica Acta*, *67*(18), 3403–3421.

Luff, R., Wallmann, K., & Aloisi, G. (2004). Numerical modeling of carbonate crust formation at cold vent sites: significance for fluid and methane budgets and chemosynthetic biological communities. *Earth and Planetary Science Letters*, *221*(1-4), 337–353.

Malinverno, a., Kastner, M., Torres, M. E., & Wortmann, U. G. (2008). Gas hydrate occurrence from pore water chlorinity and downhole logs in a transect across the northern Cascadia margin (Integrated Ocean Drilling Program Expedition 311). *Journal of Geophysical Research*, *113*(B8), B08103.

Malinverno, a., & Pohlman, J. W. (2011). Modeling sulfate reduction in methane hydrate-bearing continental margin sediments: Does a sulfate-methane transition require anaerobic oxidation of methane? *Geochemistry, Geophysics, Geosystems*, *12*(7), 1–18.

Martin, J. B., Orange, D. L., Lorenson, T. D., & Kvenvolden, K. a. (1997). Chemical and isotopic evidence of gas-influenced flow at a transform plate boundary: Monterey Bay, California. *Journal of Geophysical Research*, *102*(B11), 903–924.

Mazzotti, S. (2003). Current tectonics of northern Cascadia from a decade of GPS measurements. *Journal of Geophysical Research*, *108*(B12).

Milkov, A. V, & Sassen, R. (2002). Economic geology of offshore gas hydrate accumulations and provinces. *Marine and Petroleum Geology*, *19*(1), 1–11.

Milkov, A. V. (2004). Global estimates of hydrate-bound gas in marine sediments: how much is really out there? *Earth-Science Reviews*, *66*(3-4), 183–197

Naudts, L., Greinert, J., Artemov, Y., Beaubien, S. E., Borowski, C., & Batist, M. De. (2008). Anomalous sea-floor backscatter patterns in methane venting areas, Dnepr paleo-delta, NW Black Sea. *Marine Geology*, *251*(3-4), 253–267.

Novosel, I., Spence, G., & Hyndman, R. (2005). Reduced magnetization produced by increased methane flux at a gas hydrate vent. *Marine Geology*, *216*, 265–274.

O'Hara, K. D. (2008). A model for late Quaternary methane ice core signals: Wetlands versus a shallow marine source. *Geophysical Research Letters*, *35*(2), L02712.

Paull, C. K., Chanton, J. P., Neumann, A. C., Coston, J. A., Martens, C. S., & Showers, W. (1992). Indicators of Carbonates Carbon from and Chemosynthetic Organic Examples the Florida Deposits : Escarpment. *Society for Sedimentary Geology*, *7*, 361–375.

Paull, C. K., Ussler, W., Caress, W. D., Thomas, H., Lundsten, E., Riedel, M., Lapham, L. (2009), Seafloor Manifestations of Gas Venting and Near Seafloor Gas Hydrate Occurrences, *EOS Trans*. American Geophysical Union, 90(52), Fall Meet. Suppl.

Pohlman, J. W., Canuel, E. a., Chapman, N. R., Spence, G. D., Whiticar, M. J., & Coffin, R. B. (2005). The origin of thermogenic gas hydrates on the northern Cascadia Margin as inferred from isotopic (13C/12C and D/H) and molecular composition of hydrate and vent gas. *Organic Geochemistry*, *36*(5), 703–716.

Pohlman, J. W., Kaneko, M., Heuer, V. B., Coffin, R. B., & Whiticar, M. (2009). Methane sources and production in the northern Cascadia margin gas hydrate system. *Earth and Planetary Science Letters*, *287*, 504–512.

Pohlman J., Spence, G.D., Chapman, N.R., Hyndman, R.D., Grabowski, K.S., & Coffin, R.B. (2003). Evidence for anaerobic methane oxidation in gas hydrate rich sediments on the northern Cascadia Margin offshore Vancouver Island. *France, EGS-AGU-EUG joint assembly*, April 6-11.

Orange, D. L., Yun, J., Maher, N., Barry, J., & Greene, G. (2002). Tracking California seafloor seeps with bathymetry, backscatter and ROVs. *Continental Shelf Research*, *22*(16), 2273–2290.

Riddihough, R.P. (1982). Contemporary movements and tectonics on Canada's west coast: A discussion, *Tectonophysics*, 86, 319-341.

Riddihough, R.P. (1984). Recent movements of the Juan de Fuca plate system. *Journal of Geophysical Research* 89, 6980-6994.

Riddihough, R.P., & R.D. Hyndman (1991). Modern plate tectonic regime of the contintal margin of Western Canada. Geology of the Cordilleran Orogen in Canada, H, Gabrielse and C.J. Yoraths (eds.), Geological Survey of Canada, Geology of Canada, No. 4, (also Geological Society of America, The geology of North America, V. G2).

Riedel, M. (2001). *3-D Seismic Investigations of Northern Cascadia Marine Gas Hydrates*. Retrieved from http://voyager.library.uvic.ca/vwebv/holdingsInfo?bibld=1179457

Riedel, M., Collett, T. S., & Malone, M. (2010). Expedition 311 synthesis : scientific findings. *Proceedings of the Integrated Ocean Drilling Program* (Vol. 311).

Riedel, M. (2002). Seismic investigations of a vent field associated with gas hydrates, offshore Vancouver Island. *Journal of Geophysical Research*, *107*(B9), 1–16.

Riedel, M., Novosel, I., Spence, G. D., Hyndman, R. D., Chapman, R. N., Solem, R. C., & Lewis, T. (2006). Geophysical and geochemical signatures associated with gas hydrate-related venting in the northern Cascadia margin. *Geological Society of America Bulletin*, *118*(1-2), 23–38.

Riedel, M., Tréhu A. M., Spence G. D. (2010). Characterizing the thermal regime of cold vents at the northern Cascadia margin from bottom-simulating reflector distributions, heat-probe measurements and borehole temperature data. *Marine Geophysical Research* 31, 1–16.

Sahling, H., Rickert, D., Lee, R., Linke, P., & Suess, E. (2002). Macrofaunal community structure and sulfide flux at gas hydrate deposits from the Cascadia convergent margin, NE Pacific. *Marine Ecology Progress Series*, *231*, 121–138.

Schwalenberg, K., Willoughby, E., Mir, R., & Edwards, R.N. (2005). Marine gas hydrate electromagnetic signatures in the Cascadia and their correlation with seismic blank zones. *First Break*, 23, 57-63

Shipley, T.H. Houston, M.H., Buffler, T.T., Shaub, F.J., McMillen, K.J., Ladd, J.W., and Worzel, J.L. (1979). Seismic evidence for widespread possible gas hydrate horizons on continental slopes and rises. *American Association of Petroleum Geologists Bulletin*, 63: 2204-2213.

Solem, R.D., Spence, G.D., Vukajlovich, D., Hyndman, R.D., Riedel, M., Novosel, I., and Kastner, M. (2002). Methane advection and gas hydrate formation within an active vent field offshore Vancouver Island. *Proceedings of the Fourth International Conference on Gas Hydrates*, Yokohama, Japan, May 19-23, 84-89.

Spence, G.D., Haacke, R.R., and Hyndman, R.D. (2010). Seismic indicators of natural gas hydrate and underlying free gas. *Geophysical Characterization of Gas Hydrates, SEG Geophysical Development Series,* (14), 39-71

Stoian, I., Park, K., Yoo, D., & Haacke, R. (2008). Seismic Reflection Blank Zones In The Ulleung Basin, Offshore Korean, Associated with High Concentrations of Gas Hydrate. *Proceedings of the 6th International Conference of Gas Hydrates*. Vancouver, British Columbia, July 6-10.

Suess, E., Torres, M. E., Bohrmann, G., Collier, R. W., Greinert, J., Linke, P., Rehder, G., et al. (1999). Gas hydrate destabilization: enhanced dewatering, benthic material turnover and large methane plumes at the Cascadia convergent margin. *Earth and Planetary Science Letters*, *170*(1-2), 1–15.

Torres, M. E., Embley, R. W., Merle, S. G., Tréhu, A. M., Collier, R. W., Suess, E., & Heeschen, K. U. (2009). Methane sources feeding cold seeps on the shelf and upper continental slope off central Oregon, USA. *Geochemistry, Geophysics, Geosystems*, *10*(11), 1–21.

Torres, M. E., McManus, J., Hammond, D. E., Angelis, M. A. De, Heeschen, K. U., Colbert, S. L., Tryon, M. D., et al. (2002). Fluid and chemical fluxes in and out of sediments hosting methane hydrate deposits on Hydrate Ridge , OR , I : Hydrological provinces. *Earth and Planetary Science Letters*, *201*, 525–540.

Tsunogai, U., Maegawa, K., Sato, S., Komatsu, D. D., Nakagawa, F., Toki, T., & Ashi, J. (2012). Coseimic massive methane release from a submarine mud volcano. *Earth and Planetary Science Letters*, *341-344*(5), 79–85.

Ussler, W., & Paull, C. K. (2008). Rates of anaerobic oxidation of methane and authigenic carbonate mineralization in methane-rich deep-sea sediments inferred from models and geochemical profiles. *Earth and Planetary Science Letters*, *266*(3-4), 271–287.

Westbrook, C.K., Carson, B., Musgrave, R.J., et al. (1994). *Proceedings of the ocean drilling program, initial report*, vol 146 (part 1). Ocean Drilling Program, College Station, Texas.

Whiticar, M. J. (1999). Carbon and hydrogen isotope systematics of bacterial formation and oxidation of methane. *Chemical Geology*, *161*(1-3), 291–314.

Wilson, D.S. (1988). Tectonic history of the Juan de Fuca Ridge over the last 40 millions years. *Journal of Geophysical Research,* 94: 3065-3075.

Wood, W., Gettrust, J., & Chapman, N. (2002). Decreased stability of methane hydrates in marine sediments owing to phase-boundary roughness. *Nature*, *420* (December), 656–660.

Xu, W., & Ruppel, C. (1999). Predicting the occurrence, distribution, and evolution of methane gas hydrate in porous marine sediments. *Journal of Geophysical Research*, *104*, 5081–5095.

Yuan, J., & Edwards, R. N. (2000). The assessment of marine gas hydrate through electrical remote sounding: Hydrate without BSR? *Geophysical Research Letters*, *27*(16), 2397–2400.

Yuan, T., Hyndman, R. D., Spence, G. D., & Desmons, B. (1996). Seismic velocity increase and deep-sea gas hydrate concentration above a bottom-simulating reflector on the northern Cascadia continental slope. *Journal of Geophysical Research*, *101*(B6), 13655.

Yuan, T., Spence, G. D., & Hyndman, R. D. (1994). Seismic velocities and inferred porosities in the accretionary wedge sediments at the Cascadia margin. *Journal of Geophysical Research*, *99*(B3), 4413–4427.

Yuan, T., Spence, G. D., and Hyndman, R.D. (1999). Seismic velocity studies of a gas hydrate bottom-simulating reflector on the northern Cascadia margin: amplitude modeling and full waveform inversion. *Journal of Geophysical Research*, 104, 1179-1191.

Zühlsdorff, L., & Spieß, V. (2004). Three-dimensional seismic characterization of a venting site reveals compelling indications of natural hydraulic fracturing. *Geology*, *32*(2), 101.

Zykov, M. M., and Chapman, N.R. (2004) 3-D velocity model of hydrocarbon vent site in Cascadia region offshore Vancouver Island. AAPG Hedberg Research Conference: Gas Hydrates: Energy Resource Potential and Associated Geologic Hazards, Vancouver, 12-16 September, 2005.

Zykov, M. M. (2006). *3-D travel time tomography of the gas hydrate area offshore Vancouver Island based on OBS data*. Retrieved from https://dspace.library.uvic.ca:8443//handle/1828/1892